N 70 42829
CR 113905

THE PENNSYLVANIA STATE UNIVERSITY

# IONOSPHERIC RESEARCH

Scientific Report No. 357

## A COMPARISON OF SIMULTANEOUS PHASE AND AMPLITUDE FLUCTUATIONS IMPOSED ON SATELLITE SIGNALS BY F-REGION ANOMALIES

by
J. W. Porter

June 15, 1970

IONOSPHERE RESEARCH LABORATORY

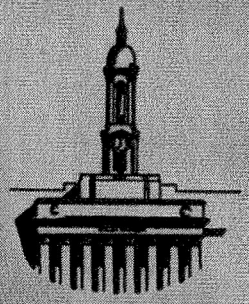

University Park, Pennsylvania NASA Grant NGR-39-009-002

Ionospheric Research

NASA Grant NGR-39-009-002

Scientific Report

on

# "A Comparison of Simultaneous Phase and Amplitude Fluctuations Imposed on Satellite Signals by F-Region Anomalies"

by

J. W. Porter

June 15, 1970

Scientific Report No. 357

Ionosphere Research Laboratory

Submitted by: W. J. Ross (aw)

William J. Ross, Professor of Electrical Engineering
Project Supervisor

Approved by: C. H. Waynick

A. H. Waynick, Director
Ionosphere Research Laboratory

The Pennsylvania State University

Department of Electrical Engineering

University Park, Pennsylvania 16802

TABLE OF CONTENTS

## ABSTRACT

The amplitude and phase variations of high frequency signals transmitted through the ionosphere from Earth Satellite S-66 were recorded and processed to allow intercomparison of seven different diffraction patterns obtained from one satellite pass. The amplitude patterns are on two harmonically related frequencies, 20 and 40 MHz, which are measured at each of two locations separated by one kilometer. The phase patterns are phase difference patterns between the two frequencies as measured at one location or between ends of the base-line using the same frequency.

To develop theoretical phase-modulating screen models and obtain relationships between the patterns as they propagated behind the screen, the diffraction theory was used. The weak, one-dimensional, phase-modulating screen was extended in complexity to include two-dimensional, non-weak, thick, and discrete blob screens. The screens were assumed repetitive in structure; that is, their phase modulations could be represented by a finite number of Fourier terms which were functions of distance along the screen measured in two orthogonal directions. The common limiting assumptions of gaussian spatial distributions and the observer being either in the far field or the first Fresnel zone were not used. Patterns which developed behind each screen model were determined as functions of modulation intensity, scale size, distance to satellite and screen, and zenith angle.

The measured diffraction patterns were projected for comparison and sampled. Their autocorrelation functions and Fourier spectra were calculated using two harmonic analysis programs written for this investigation. Distribution of these spectra for the various patterns was

explained in terms of theoretical screen characteristics and geometrical considerations of the satellites, screen, and receiver. Data analysis procedures included transferring the various measured patterns back to the height of the screen by use of appropriate propagation factors. The height was incremented such as to minimize differences between transferred patterns in a least squares sense.

It was concluded that the total peak phase modulation is usually more than one radian; this large value is justified by showing that thick two-dimensional phase-modulating screens are not as effective in producing large scintillation indexes are a.c. to d.c. ratios. Also, the larger scale sizes containing most of the phase variation do not develop in the amplitude patterns. It is shown by theoretical analysis and measured data that scale size variation deduced from measurement of diffraction patterns depends on both the radiating source and the particular pattern measured. Radio stars and high satellites tend to give larger scale sizes than do satellites close to the diffraction screen. Also, phase difference patterns between harmonically related frequencies tend to give larger scale sizes than do the amplitude patterns for the same satellite. Phase interferometer patterns are shown to be very sensitive to baseline lengths. The mean scale size obtained for the amplitude patterns was $L_F$ = 2.16 km, equivalent to a correlation length, $L_C$, of 0.34 km. Phase difference patterns between harmonically related frequencies yielded a scale size, $L_F$ = 7.0 km, equivalent to a correlation length of 1.1 km.

In comparing results with those of other investigations, explanations are given for several observed phenomena. These phenomena include the difference in pattern correlation functions when

measurements are made on radiation at two or more frequencies, the lack of expected dependence of scintillation index on wavelength, and the existence of either, but not both, phase or amplitude diffraction patterns during a track.

# CHAPTER 1 INTRODUCTION

## 1.1 General Review

Scintillations in the amplitude and phase of the signals from radio stars and Earth satellites have been observed for a number of years at points scattered throughout the world. These fluctuations are imposed on the radio waves as they pass through the irregular structure of the ionosphere. Because of the relative ease with which they are measured, most of the extensive literature relating to the radio star and satellite scintillations has dealt only with the amplitude fluctuations. The generally accepted model for producing the scintillation phenomenon is a diffracting layer of irregular electron concentration located in the ionosphere. The irregularity in the refractive index of this layer acts as a thin lens for focusing and defocusing the emerging wave so as to produce an irregular pattern as observed by a receiver some distance below the screen. To relate these fluctuations which are measured on the ground to the medium where they are produced, it is necessary to determine how the signal varies as it propagates from the region of the screen where the wave is modulated.

Increasing interest in the effect of these ionospheric variations on electromagnetic wave propagation and diffraction or scattering has induced considerable work in recent years. Three different theoretical approaches have been used for handling the problem. A number of investigators have treated the problem such that the wave at the receiving antenna is regarded as the sum of the original wave and a number of components that have been scattered from each volume of the irregular

ionosphere. This method is direct but is difficult to apply when scattering is not weak or for an arbitrary distribution of scatterers. In attempting to overcome the latter deficiency, the properties of the irregular medium are usually described statistically in terms of some assumed form of correlation function. Also, most of this work has been a blend of statistical approximations using the electromagnetic wave theory, since an exact analytical solution of the general propagation and scattering problems is not feasible, even if the physical behavior of the regions along the ray path is well-defined. For this reason, stress has been on the statistics, and physics enters only for considerations of the nature of the turbulence and for application of Maxwell's equations. Unfortunately, once a statistical model amenable to the necessary operations has been selected to describe the medium at the screen, the possibility of a more general solution has been removed.

A second method used for handling the scintillation problem is ray optics. This method is not very rigorous since ray optics only apply when the size of the anomalies is much larger than a wavelength and thus very large compared to the first Fresnel zone measured at the point of pattern observation. This method has been used when strong scattering exists or a single large anomaly is being considered. It does not work well when the modulating region contains a number of scale sizes, some of which are only an order of magnitude larger than the wavelength.

The third approach to the solution of the scintillation problem is the diffraction theory. The properties of the wave front on emerging from the region of the anomalies are related to the properties of those

anomalies. The propagation through the space beyond the region of the anomalies is treated as a diffraction problem. To model the changes given the wavefront as it passes through the region of the anomalies, the concept of an equivalent thin screen is used. The screen is assumed to be very thin in the direction of propagation and to modulate the wave incident upon it by an amount which is a function of position across the screen.

Booker and Clemmow (1950)[1] first showed the relationships existing between an electric field and an angular spectrum of plane waves; this was followed by an application of the principle to ionospheric diffraction problems by Booker, Ratcliffe, and Shinn (1950)[2]. It was then shown by Hewish (1951, 1952)[3],[4] how the field produced by an individual Fourier component vaired with distance beyond the screen. This work was followed by that of Bowhill (1960, 1961)[5],[6], DeBarber and Ross (1963)[7], Yeh and Swenson (1964)[8], and many others. Unfortunately, in formulating a model for the spatial distributions, most investigators assume that the correlation function of the dielectric constant or of the electron density is gaussian with an elliptical symmetry[4],[10]. The assumption of gaussian shape is used for convenience and has no physical basis[8]; however, it does influence the solution of the problem. The ergodic assumptions often made are of doubtful validity unless the amount of data available is extensive. This results because the properties of the measured patterns change with position of the radiating source and time of the observation. The averaging effects of the models containing the ergodic assumptions obscure the individual character of the patterns.

In most previous investigations, the intensity of the phase modulation, $\phi_0$ , and the correlation distance, $r_0$ , are the two independent parameters specified for the single gaussian function used to describe the phase-modulating screen. It is asserted that when $\phi_0$ is less than one radian, the scale sizes of the diffraction patterns in the radiation at wavelength, $\lambda$ , are equal to those of the screen at those distances, $Z$ , where $\lambda Z/r_0^2 >> 1$. However, when $\phi_0$ is larger than one radian, the scale sizes of the patterns measured at large distances from the screen should be smaller than those at the screen.

The approach taken by these past investigations has resulted in the conclusions that: (1) the amount of modulation and scintillation is proportional to wavelength; (2) the phase pattern has the same correlation as the screen; (3) the amplitude pattern develops with a linear dependence on the distance from the screen until it reaches a maximum beyond which it remains constant; and (4) the scale size in the amplitude pattern depends on the amount of modulation.

The experimental results of these prior investigations indicate that the ionospheric irregularities which produce the observed diffraction patterns may occur at heights of from 250 km to 600 km, although the thickness of the region containing the irregularities is sometimes less than 50 km. The scale size of the anomalies which were defined by the correlation distance for the gaussian function, $r_0$ , or the separation of successive maxima or minima, $L$ , were found to vary from 2 km to 10 km. These anomalies were said to be elongated by a ratio of 5 to 1, or greater, with the larger axis along the line of the magnetic field.

For those experiments where the records of the diffraction patterns were analyzed to determine their harmonic content, long samples were taken together, and autocorrelation functions and their cosine transforms were used to obtain the power spectral densities. This method is one best applied to random processes; because of its smoothing characteristic, it tends to fill in for those harmonics possessing little energy. Nevertheless, the spectra obtained were somewhat discrete and not continuous as would be required by the theory using the assumed distributions. Examples of other observed phenomena unexplained by the theory of the earlier experiments are: the absence of either the phase or amplitude pattern when the other was present, as observed by DeBarber (1962)[15], and the inversion effect, where the longer wavelength transmissions contained less scintillations, as observed by Briggs (1966)[11].

There are reasons why a description of the irregular ionosphere has not been obtained by use of a more direct approach. To obtain a unique set of ionospheric characteristics from the interpretation of the diffraction patterns measured on the ground is most difficult. One approach would be to extrapolate backwards a complete surface map of the measured patterns to yield a corresponding map at the diffracting region. This is prevented by the practical limitations on the amount of data which can be gathered on the ground. Some form of modeling is thus employed to produce patterns similar to those which are measured. Among the most frequently used models is that of the thin modulating screen. The wave emerging below the screen has a complex field pattern which may show variations in both its amplitude and phase.

Another approach would be to synthesize, in depth, the medium which would convert the known spherical wavefront into the observed field pattern. This is a most difficult problem which may not have a unique solution. However, the physics of the ionosphere in the altitude range where the effects are incurred, does provide some insight as to the screen model to use. The causative process is refractive rather than absorptive; the changes in the emerging wavefront are then in phase rather than in amplitude, and a phase-modulating screen is generally employed for modeling.

## 1.2 Statement of the Problem

The previous section discussed the complexity and difficulty of obtaining a rigorous solution for the nature, position, and extent of the ionospheric region responsible for the fluctuations imposed on radiation from radio stars and Earth Satellites. To circumvent these difficulties, modeling was used to represent the significant characteristics of the phase-modulating regions. The ergodic assumptions which have been made for the majority of the studies of F region irregularities were made principally for mathematical convenience. Their use has resulted in unexplained behavior when comparisons are made between the diffraction patterns which develop behind the theoretical screens and the real patterns measured at the ground.

A new approach, to obtain better models for representing the region of the ionosphere which produces the scintillation on the radio signals passing through it, is dictated by the limitations of the existing techniques. This new approach should be flexible enough to

synthesize variable models that will correspond with the measurements made on real-phase and amplitude diffraction patterns. One way to achieve more flexibility in the models is to assemble them from a sum of weakly modulating, two-dimensional, spatial Fourier series terms.

## 1.3 Specific Statement of Problem

It is the objective of this investigation to relate the properties of the diffraction patterns measured on the ground to a realistic model of the irregular ionosphere. To accomplish this, scintillation measurements will be made at spaced receiver locations at two satellite frequencies simultaneously. To obtain the phase and amplitude diffraction patterns, a receiving system will be designed and will record the data required for analysis. Where possible, the methods used for data analysis will avoid making any unnecessary assumptions. A series of theoretical ionospheric model studies will be made to determine relationships between the irregularities and the diffraction patterns they produce. The experimental results will be compared with the theoretical models to make better estimates for the irregular ionosphere.

## CHAPTER 2 PHASE AND AMPLITUDE PATTERNS PRODUCED BY PHASE-MODULATING SCREENS

This section develops expressions to represent the phase and amplitude scintillation patterns which develop behind a phase-modulating screen on which H.F. radiation is incident. For this investigation, the radiation emanates from an artificial Earth satellite located a finite distance, $Z'$ , above the region of the ionosphere where the phase-modulating anomalies are situated. The receiver at the Earth's surface, which measures the pattern is located a distance, $Z$ , from the same screen of phase-modulating anomalies.

The first screen examined is the weka, single-frequency, one-dimensionsla, continuous screen. This has been investigated previously[3],[4]; however, the known results are presented here for completeness and for revealing certain characteristics essential for developing the later models. The way in which these patterns propagate behind the screen is shown to be a function of the scale size of the screen and the distance of the source from the screen. The complexity of this simple screen is increased as the screen is made non-weak, two-dimensional, thick, and finally to consist of an array of discrete blobs.

For each screen model, the appropriate phase and amplitude patterns which develop behind the screen are obtained. The discrete blob screen, which reduces to a two-dimensional, cosinusoidal screen for a special case, is shown to have a realizable correlation function. In all cases investigated, it is shown that the resulting diffraction patterns may be represented by a small number of significant Fourier components. The effects of the satellite-screen geometry, on the particular patterns

measured as part of the experiment, are discussed. The amount of electron density variation required to produce various levels of phase modulation is also determined.

## 2.1 The Weak One-Dimensional Screen Containing a Single Spatial Frequency

The first screen investigated is infinitely thin in the plane $Z = 0$ and has a weak phase variation in one direction, $X_0$ , the phase modulation function being a cosinusoidal function of $X_0$ . The geometry for the satellite, screen, and receiver is shown in Figure 1. To obtain the patterns, the spatial Fourier transform is used, first to find the angular spectrum of plane waves that represents the electric field as it emerges from the bottom of the phase-modulating screen. A second transform is then acquired of the angular spectrum to find the complex field beyond the screen as a function of the cartesian coordinates-- $X$ , $Z$ . The angular spectrums are given in terms of $S$ where $S$ is the sine of the angle $\Theta$ , the angle between the incident radiation at the screen and a diffracted component.

In this analysis, normal incidence has been used because the small change in weighted distance to the observer, which results when the screen is tilted, has little effect on the coefficients for pattern propagation. The spatial Fourier transforms relating the angular spectrums of plane waves and the one-dimensional variation in the complex electric field, $E$ , are then:

$$P(S) = \int_{-\infty}^{\infty} E(X_0, 0)\, e^{\frac{-j2\pi S X_0}{\lambda}}\, dX_0 \qquad (2\text{-}1)$$

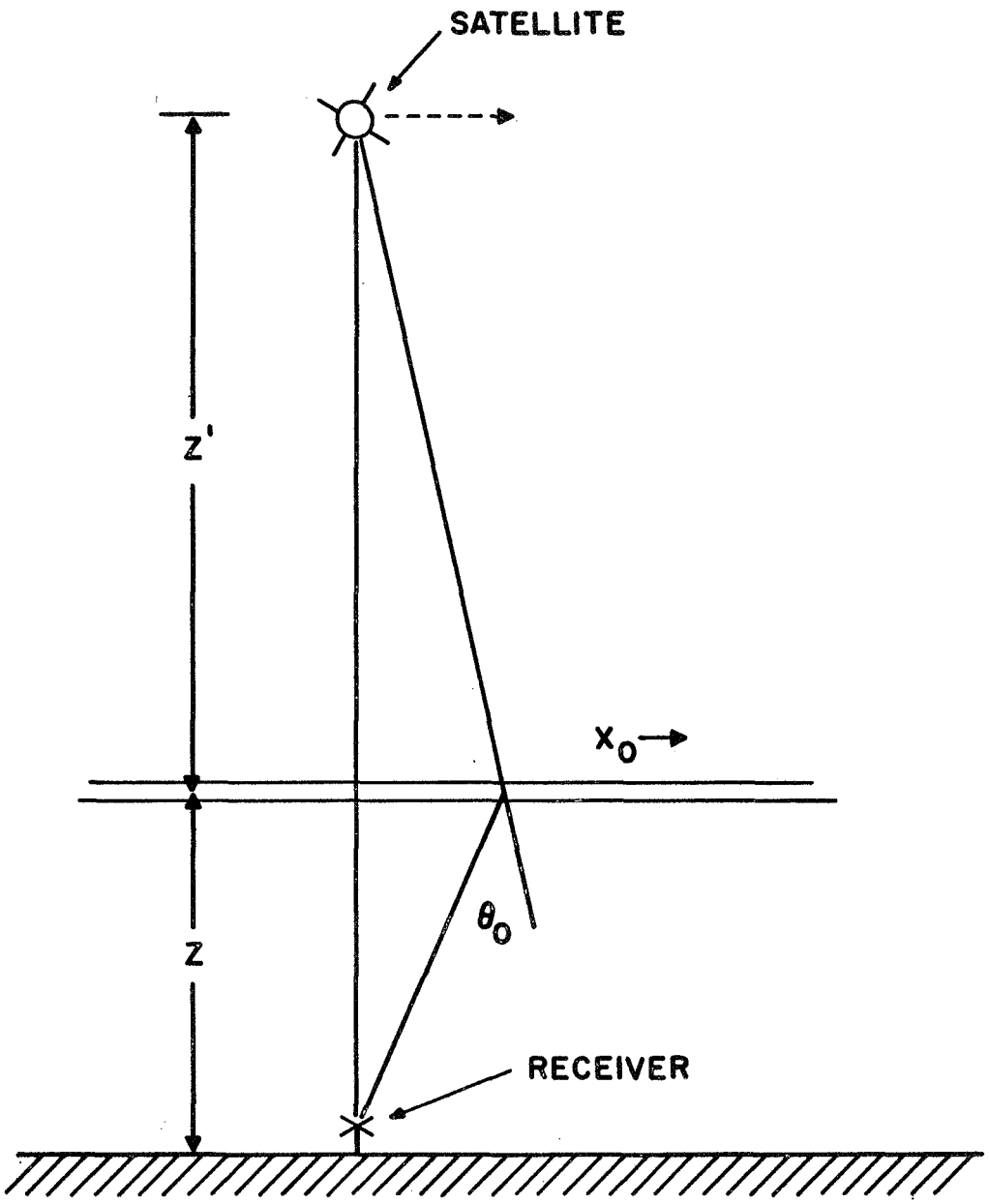


Figure 1. Satellite-Receiver Geometry

$$E(X_0, 0) = \frac{1}{\lambda} \int_{-\infty}^{\infty} P(S)\, e^{\frac{j2\pi S X_0}{\lambda}}\, dS \qquad (2\text{-}2)$$

The limits for the Fourier transform here are $\pm \infty$ for the variable $S$. It follows that, when $|S| > 1$, $\cos \theta = (1 - S^2)^{1/2}$ will be imaginary. The significance of this behavior is evident when the expression for finding the complex field, a distance, $X$, $Z$, is examined.

$$E(X, Z) = \frac{1}{\lambda} \int_{-\infty}^{\infty} P(S)\, e^{\frac{j2\pi S X}{\lambda}}\, e^{\frac{j2\pi C Z}{\lambda}}\, dS \qquad (2\text{-}3)$$

When $S$ is larger than one, the angular spectrum component has a spatial period less than $\lambda$ in the $X$ direction, but it is attenuated in the $Z$ direction. A series of these components will comprise what is known as an evanescent wave; these waves are rapidly attenuated as they leave the screen so as not to contribute to a pattern some distance behind the screen.

For the weak scattering considered here, only the first two terms in the binomial expansion for $C$ are used; that is:

$$C \approx 1 - \frac{1}{2} S^2 \qquad (2\text{-}4)$$

This is equivalent to a Fresnel region representation of the field when weak scattering exists. As will be shown, when the satellite is at a finite distance (1,000 km), only small anomalies place the receiver in the far field.

It then follows that:

$$E(X, Z) = \frac{1}{\lambda} e^{\frac{j2\pi Z}{\lambda}} \int_{-\infty}^{\infty} P(S)\, e^{\frac{j2\pi XS}{\lambda}}\, e^{\frac{-j\pi ZS^2}{\lambda}}\, dS \qquad (2\text{-}5)$$

where the phase shift is made positive with increasing $Z$. Because the satellite producing the radiation is a finite distance from the screen, the wavefront incident on the screen is spherical and has a phase dependent on the displacement from origin, $X_0$. If the phase-modulating screen has a modulation function, $\phi(X_0)$, the angular spectrum at the screen becomes:

$$P(S) \approx e^{\frac{j2\pi Z'}{\lambda}} \int_{-\infty}^{\infty} e^{j\phi_0(X_0)}\, e^{\frac{j\pi X_0^2}{\lambda Z'}}\, e^{\frac{-j2\pi SX_0}{\lambda}}\, dX_0 \qquad (2\text{-}6)$$

For the weak cosinusoidal screen:

$$e^{j\phi_0(X_0)} \approx 1 + j\phi_0 \cos\frac{2\pi X_0}{L} \qquad (2\text{-}7)$$

where $L$ is the scale size of the screen.

When the cosine function is replaced by its exponential form,

$$P(S) = e^{\frac{j2\pi Z'}{\lambda}} \int_{-\infty}^{\infty} \left[1 + \frac{j\phi_0}{2}\left(e^{\frac{j2\pi X_0}{L}} + e^{-\frac{j2\pi X_0}{L}}\right)\right] e^{j\left(\frac{\pi X_0^2}{\lambda Z'} - \frac{2\pi S X_0}{\lambda}\right)} dX_0 \tag{2-8}$$

Sneddon (1951)[12] gives the solution for complex integrals of this form. Upon completing the integration of 2-8,

$$P(S) = e^{\frac{j2\pi Z'}{\lambda}} \sqrt{j\lambda Z'} \left\{ e^{-\frac{j\pi Z' S^2}{\lambda}} + \frac{j\phi_0}{2}\left[e^{-j\pi\lambda Z'\left(\frac{S}{\lambda} - \frac{1}{L}\right)^2} + e^{-j\pi\lambda Z'\left(\frac{S}{\lambda} + \frac{1}{L}\right)^2}\right]\right\} \tag{2-9}$$

In later developments, additional terms of the form $\cos \frac{2n\pi X_0}{L}$ will be used to represent the screen. The $1/L$ terms in 2-9 then become $n/L$ .

To obtain the complex field at $X$ , $Z$ , the $P(S)$ of 2-9 is substituted into 2-5 and the integration is performed. After collecting terms, the result may be written as:

$$E(X, Z) = \sqrt{\bar{F}}\left[1 + \phi_0 \sin\frac{\pi\lambda\bar{F}Z}{L^2}\cos\frac{2\pi\bar{F}X}{L} + j\phi_0 \cos\frac{\pi\lambda\bar{F}Z}{L^2}\cos\frac{2\pi\bar{F}X}{L}\right] e^{\frac{j2\pi(Z+Z')}{\lambda}} e^{\frac{j\pi X^2}{\lambda(Z+Z')}} \tag{2-10}$$

where $\overline{F} = \frac{Z'}{Z + Z'}$

The two exponentials represent the phase of the undiffracted wave at point $X$, relative to which the diffracted wave field can be normalized.

It is noted that the one-dimensional, weak phase, modulating screen produces a diffraction pattern beyond the screen which has both an in-phase and quadrature component relative to the undiffracted wave. The in-phase component has an amplitude which varies as a sine function of the distance from the screen, $Z$, while the quadrature component varies as a cosine function of the same distance. This means that the amplitude pattern does not fully develop until some distance beyond the screen. Also, if the screen is very thin, there are values of $Z$ for which the phase pattern vanishes.

That the source is at a finite distance, $Z'$, from the screen changes the pattern of a one-dimensional screen in three fashions. First, the size of the pattern has been enlarged by a factor, $(Z + Z')/Z'$, which is the factor of ray optical projection methods. Second, the distance to the development of the in-phase pattern has been increased by the same expansion factor, $(Z + Z')/Z'$. Last, the amplitude of all terms has been decreased by this expansion factor to the minus one-half power as compared to the case where the source is at $\infty$ and normalization is to the same incident power flux upon the screen. The non-parallel rays, which are scattered and then combine to produce the pattern, continue to diverge, reducing the magnitude of the pattern at a point beyond

the screen. When the satellite approaches close to the screen, the in-phase pattern does not develop and the scale size of the quadrature pattern is much enlarged.

The phase, $\psi$, and amplitude, A, of the diffraction pattern can be expressed as functions of the in-phase and quadrature components:

$$\text{Tan } \psi = \left( \frac{\phi_0 \cos \frac{\pi\lambda\bar{F}Z}{L^2} \cos \frac{2\pi\bar{F}X}{L}}{1. + \phi_0 \sin \frac{\pi\lambda\bar{F}Z}{L^2} \cos \frac{2\pi\bar{F}X}{L}} \right) \tag{2-11}$$

$$A = \sqrt{\bar{F}} \left(1. + 2\phi_0 \sin \frac{\pi\lambda\bar{F}Z}{L^2} \cos \frac{2\pi\bar{F}X}{L}\right)^{1/2} \tag{2-12}$$

Since $\phi_0$ is assumed small, $\psi$ is also small; then $\text{Tan } \psi \approx \psi$ :

$$\psi \approx \phi_0 \cos \frac{\pi\lambda\bar{F}Z}{L^2} \cos \frac{2\pi\bar{F}X}{L} \tag{2-13}$$

If only the first two terms of the binomial expansion of 2-12 are retained, the function for the amplitude pattern becomes:

$$A = \sqrt{\bar{F}} \left(1. + \phi_0 \sin \frac{\pi\lambda\bar{F}Z}{L^2} \cos \frac{2\pi\bar{F}X}{L}\right) \tag{2-14}$$

When $\phi_0$ is small and the patterns contain only one spatial frequency, the amplitude pattern will have its first maximum for $Z = L^2/2\lambda\bar{F}$ . For a particular scale size, L, the distance at which the amplitude pattern develops decreases as the wavelength of the incident radiation, $\lambda$, is increased. Conversely, if only one frequency

is being transmitted ($\lambda$, a constant), then the distance required for the amplitude pattern development decreased with the scale size, $L$. At distances, $Z$, less than half the value for the maximum pattern to occur, $Z_m$, the magnitude of the amplitude pattern may be approximated by a linear expression:

$$A \approx \sqrt{F}\left(1 + \phi_0 \frac{\pi}{2}\frac{Z}{Z_m}\right) \tag{2-15}$$

This section has shown how the phase and amplitude patterns evolve behind weak phase-modulating screens that are represented by a single spatial frequency. In the general case, where the patterns consist of a finite number of these frequencies, the more complex patterns are obtained on applying the principle of superposition.

## 2.2 The One-Dimensional Screen When Modulation is Not Weak

When the cosinusoidal screen is used and $\phi_0$ is not much less than unity, Bessel function expansions must be used. The phase-modulating term of 2-6 is written as:

$$e^{j\phi_0 \operatorname{Cos} \frac{2\pi X_0}{L}} = \cos\left(\phi_0 \cos\frac{2\pi X_0}{L}\right) + j \sin\left(\phi_0 \cos\frac{2\pi X_0}{L}\right) \tag{2-16}$$

where

$$\cos\left(\phi_0 \cos\frac{2\pi X_0}{L}\right) = J_0(\phi_0) - 2J_2(\phi_0)\cos\frac{4\pi X_0}{L} + 2J_4(\phi_0)\cos\frac{8\pi X_0}{L} - \ldots. \tag{2-17}$$

$$\text{and} \quad j \sin\left(\phi_0 \cos\frac{2\pi X_0}{L}\right) = j\left(2J_1(\phi_0)\cos\frac{2\pi X_0}{L} - 2J_3(\phi_0)\cos\frac{6\pi X_0}{L} + 2J_5(\phi_0)\cos\frac{10\pi X_0}{L} - \ldots .\right) \tag{2-18}$$

Here $J_n(\phi_0)$ is the Bessel function of the first kind and nth order.

If 2-17 and 2-18 are substituted into 2-8 in lieu of 2-7 and the integrations are performed with respect to $X_0$ and then $S$, the result for $E(x,z)$ is a series of terms of the form:

$$\sqrt{F}\ (j)^n\ 2J_n(\phi_0)\left(\cos\frac{\pi n^2\lambda\bar{F}Z}{L^2} - j\sin\frac{\pi n^2\lambda\bar{F}Z}{L^2}\right)\cos\frac{2\pi n\bar{F}X}{L} \tag{2-19}$$

On collecting terms and making the substitutions-- $T = \frac{2\pi\bar{F}X}{L}$, $R = \frac{\pi\lambda\bar{F}Z}{L^2}$, the in-phase and quadrature components become:

In-Phase

$$\sqrt{F}\left(J_0(\phi_0) + 2J_1(\phi_0)\cos T \sin R - 2J_2(\phi_0)\cos 2T\cos 4R - 2J_3(\phi_0)\cos 3T\sin 9R + 2J_4(\phi_0)\cos 4T\cos 16R + 2J_5(\phi_0)\cos 5T\sin 25R - \ldots .\right) \tag{2-20}$$

Quadrature

$$\sqrt{\overline{F}}\Big(2J_1(\phi_0)\cos T\cos R + 2J_2(\phi_0)\cos 2T\sin 4R - 2J_3(\phi_0)\cos 3T\cos 9R - 2J_4(\phi_0)\cos 4T\sin 16R + 2J_5(\phi_0)\cos 5T\cos 25R + \ldots\Big) \quad (2\text{-}21)$$

Calculations were made, using a simulation program, to obtain the patterns that develop behind a sinusoidal phase-modulating screen which is not weak. The phase pattern is taken to be relative to the specular component of the angular spectrum, which becomes small with increasing $\phi_0$ . For all values of $\phi_0$ , this phase pattern will have a zero mean over the spatial period at the point where it is measured. The amplitude pattern is taken to be the amplitude fluctuation about the mean amplitude over the same period.

The first calculations were made for a relatively weak modulation, $\phi_0 < 0.5$ radian; these were followed where $\phi_0$ was increased in steps until it reached four radians. Figures 2 through 5 show the phase and amplitude patterns which result for $\phi_0$ having the values 0.25, 0.5, and 0.8 radians for different values of $\Theta$ ; $\Theta = \pi\lambda\overline{F}Z/L^2$ . The amplitude patterns were normalized to show variation about unity, while the scale of the phase patterns is given in radians. It is observed that for these values of $\phi_0$ there are distances represented by $\Theta$ which yield patterns no longer cosinusoidal in appearance.

When a thin screen has a scale size, $L$ , for every $\lambda$ , there is a value of $\overline{F}Z$ that reduces either the phase or amplitude pattern.

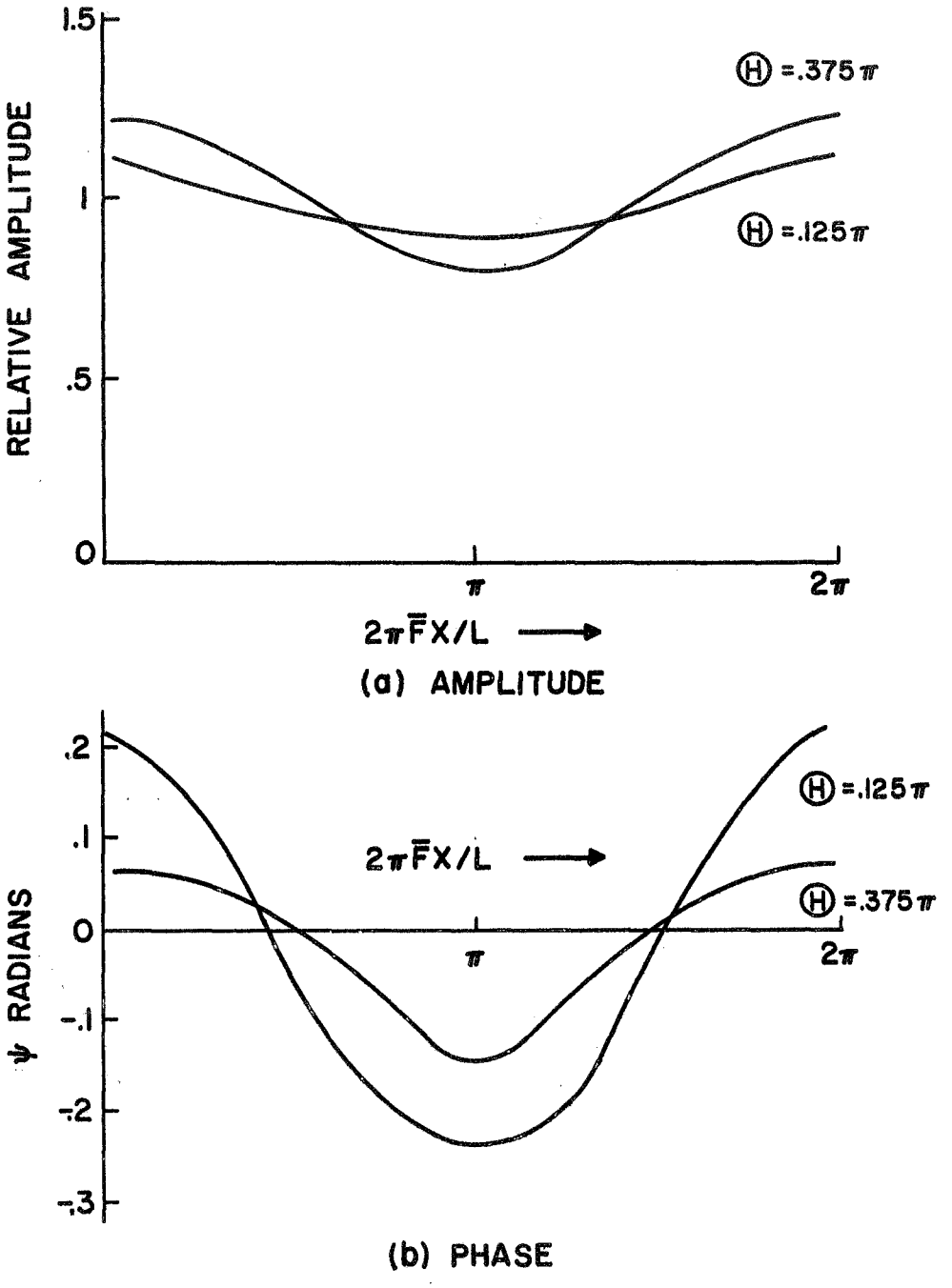


Figure 2. Diffraction Patterns Produced by a Weak One-Dimensional Screen with $\phi_0$ of 0.25 Radians

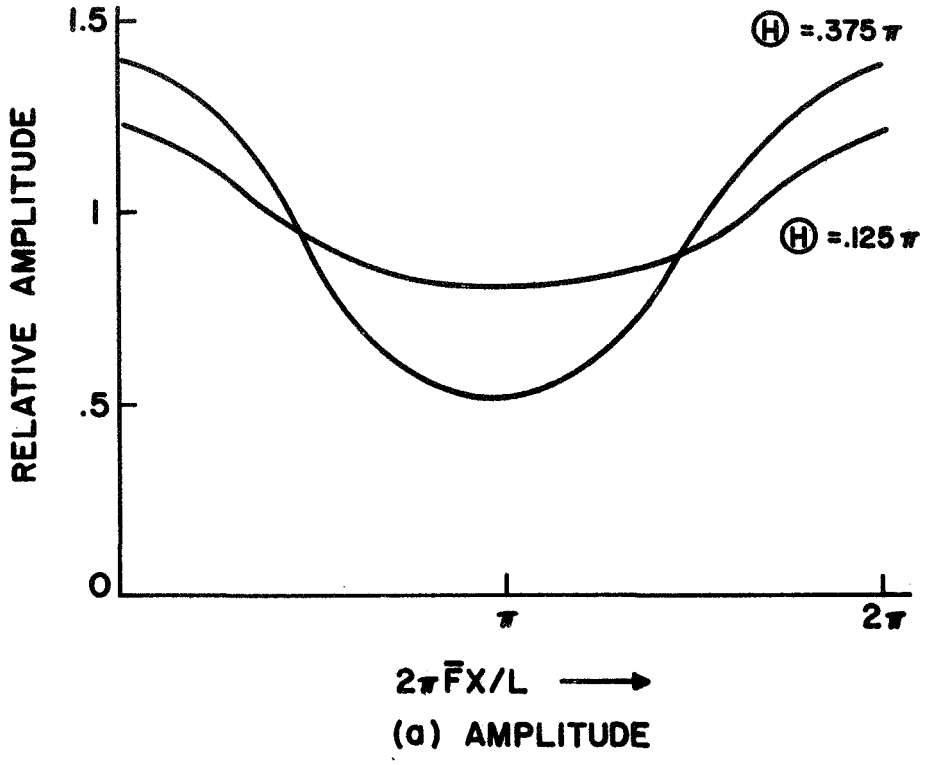


(a) AMPLITUDE

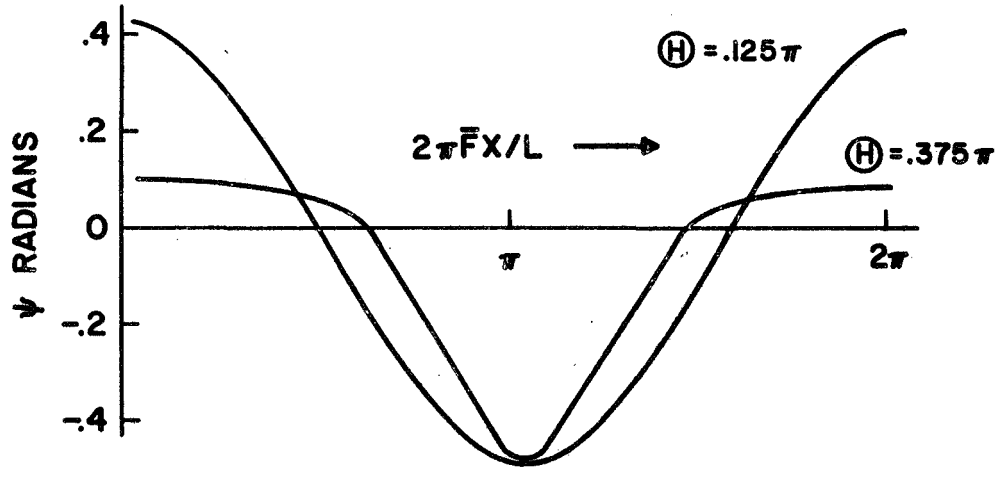


(b) PHASE

Figure 3. Diffraction Patterns Produced by a One-Dimensional Screen with $\phi_0$ of 0.5 Radians

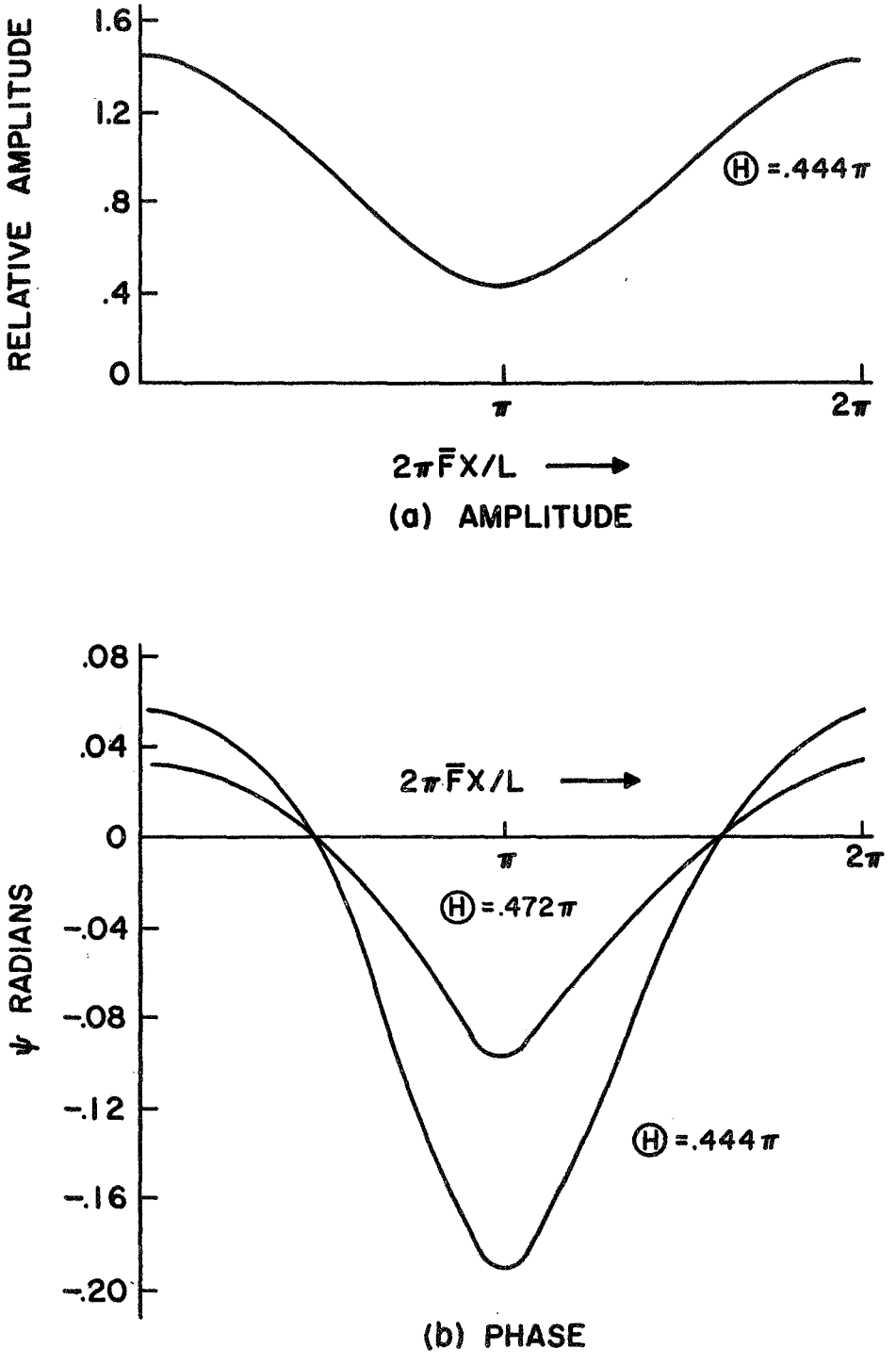


Figure 4. Diffraction Patterns Produced by a Screen with $\phi_0$ of 0.5 Radians

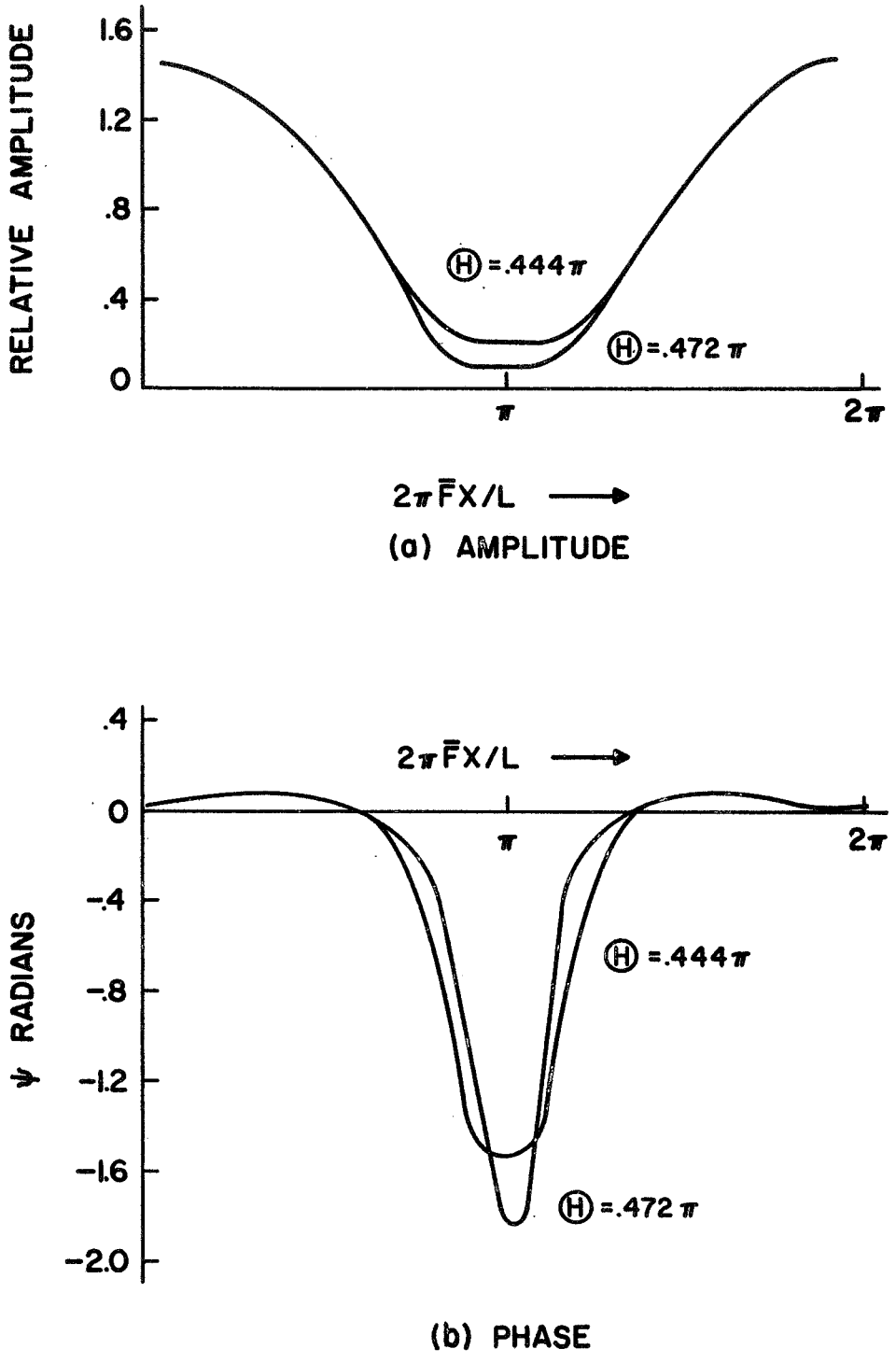


Figure 5. Diffraction Patterns Produced by a One-Dimensional Screen with $\phi_0$ of 0.8 Radians

However, they do not vanish together. This extinction phenomena is able to produce, at times, stronger amplitude patterns on 40 MHz than on 20 MHz radiation, even though $\phi_0$ is proportional to $\lambda$ in the ionospheric phase-modulating screens; values of $\Theta$ between $0.84\pi$ and $1.16\pi$ for the 20 MHz radiation produce this result. When the diffracting screens are sufficiently thin and the source of radiation moves in a few seconds across the region of the screen to be sampled, then the observed patterns become functions of time which depend primarily on the motion of the source. For this investigation, where the satellite source is moving at a velocity of greater than 7 km/sec., the assumption is made that the pattern is preserved over the sampling period. Using this assumption, other behavior of the amplitude patterns with the distance, $\Theta$ , can also be used to provide insight into the quadrant in which this quantity lies. When $\Theta$ lies between 0 and $\pi$ for the pattern on the 20 MHz signal, the 20 MHz and 40 MHz patterns would have peaks and nulls which occur close together with respect to time. When $\Theta$ lies in the range of $\pi$ to $2\pi$ for the amplitude pattern on the 20 MHz radiation, the nulls and peaks on the 40 MHz radiation are shifted along the time scale such as to not be coincident with those of the 20 MHz patterns.

For phase patterns when $\Theta$ is between $\pi/2$ and $\pi$ for the 20 MHz radiation, this pattern is inverted with respect to the phase pattern on the 40 MHz radiation. This increases the values obtained when phase difference measurements are made between the two frequencies. When $\phi_0 > 1$ , more terms are required by the Bessel function expansion to represent the in-phase and quadrature components. Also, both the phase and amplitude

patterns have finer structures and the in-phase pattern develops closer to the screen. To be realistic in the simulations for calculating the phase and amplitude patterns, appropriate values had to be selected for the independent parameters. These were:

$\lambda$ = wavelength, 0.015 and 0.0075 km
L = scale size, 1 to 10 km
$Z'$ = distance from screen to satellite, 750 to 600 km
Z = distance from receiver to screen, 250 to 400 km

A number of combinations of these parameters were selected for the computations that gave the following quantities as a function of position in a direction parallel to the scale size.

- The in-phase terms using significant terms of 2-20.
- The quadrature terms using significant terms of 2-21.
- The phase pattern using 2-11 with all significant terms.
- The amplitude pattern using 2-12 with all significant terms.

Although smaller scale sizes are observed in the phase and amplitude patterns as the higher order terms become more significant with the increase in $\phi_0$, the spatial period does not change; it is still $L/\overline{F}$. The phase pattern retains its sinusoidal shape for some values of $\Theta$ but in general is distorted as shown by Figures 6 through 8. When these patterns are sampled and their Fourier spectrums are developed, they will show these variations as higher spatial frequencies. As the intensity of the modulation represented by a single spatial frequency is increased, for the thin screen the extinction phenomena and pattern inversion still hold and occur at the same values of $\Theta$ which applied to the weaker screen.

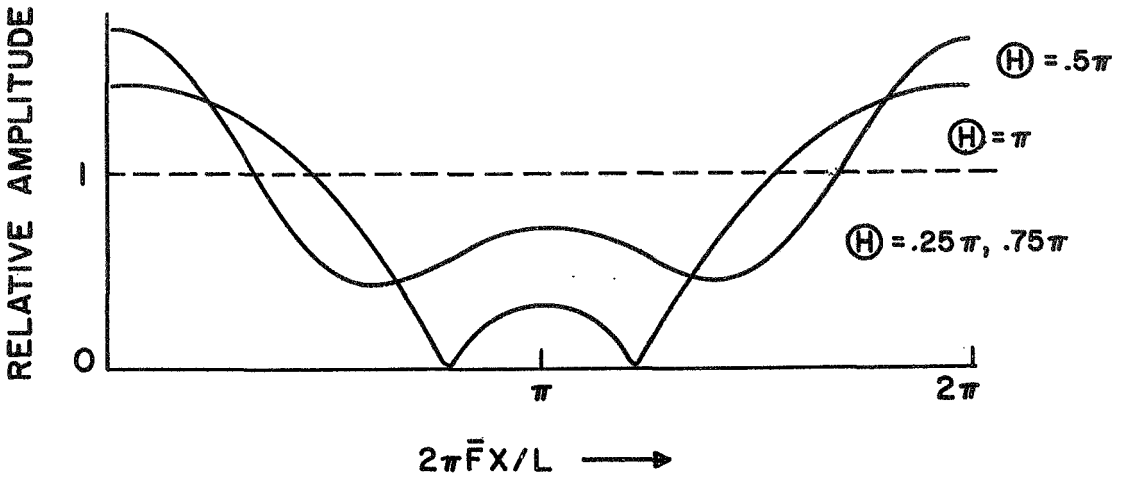


(a) AMPLITUDE

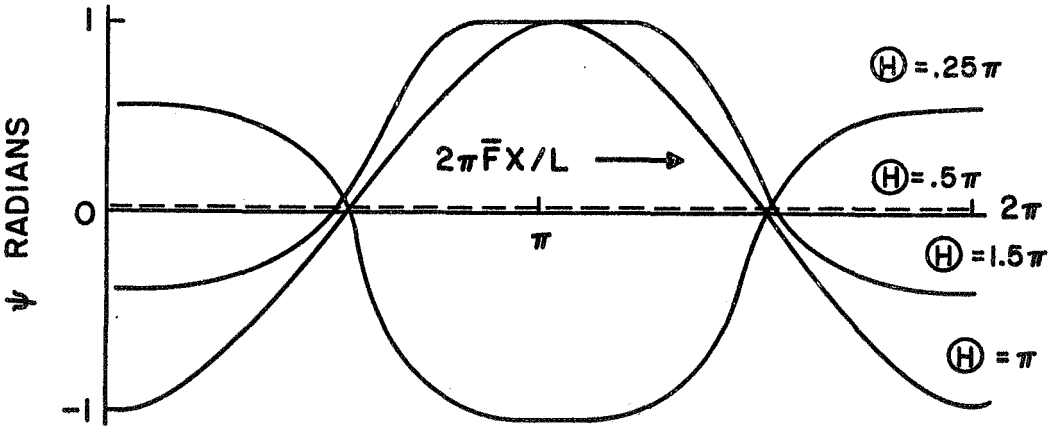


(b) PHASE

Figure 6. Diffraction Patterns Produced by a Screen with $\phi_0$ of 1. Radian

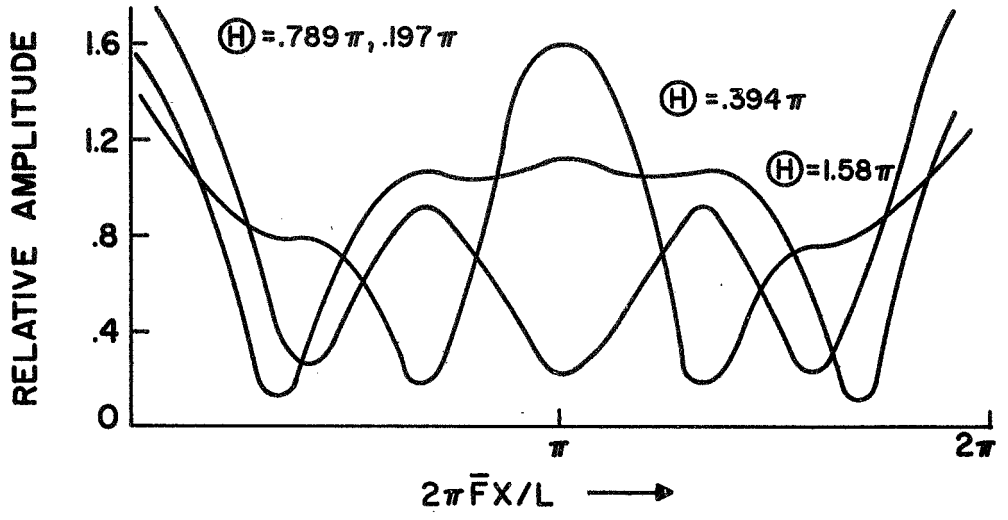


(a) AMPLITUDE

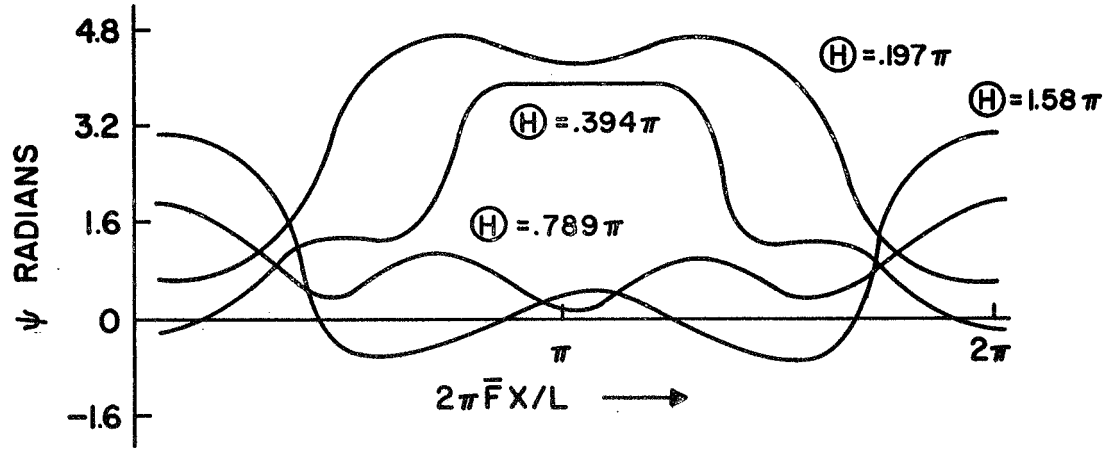


(b) PHASE

Figure 7. Diffraction Patterns Produced by a One-Dimensional Screen with $\phi_0$ of 2. Radians

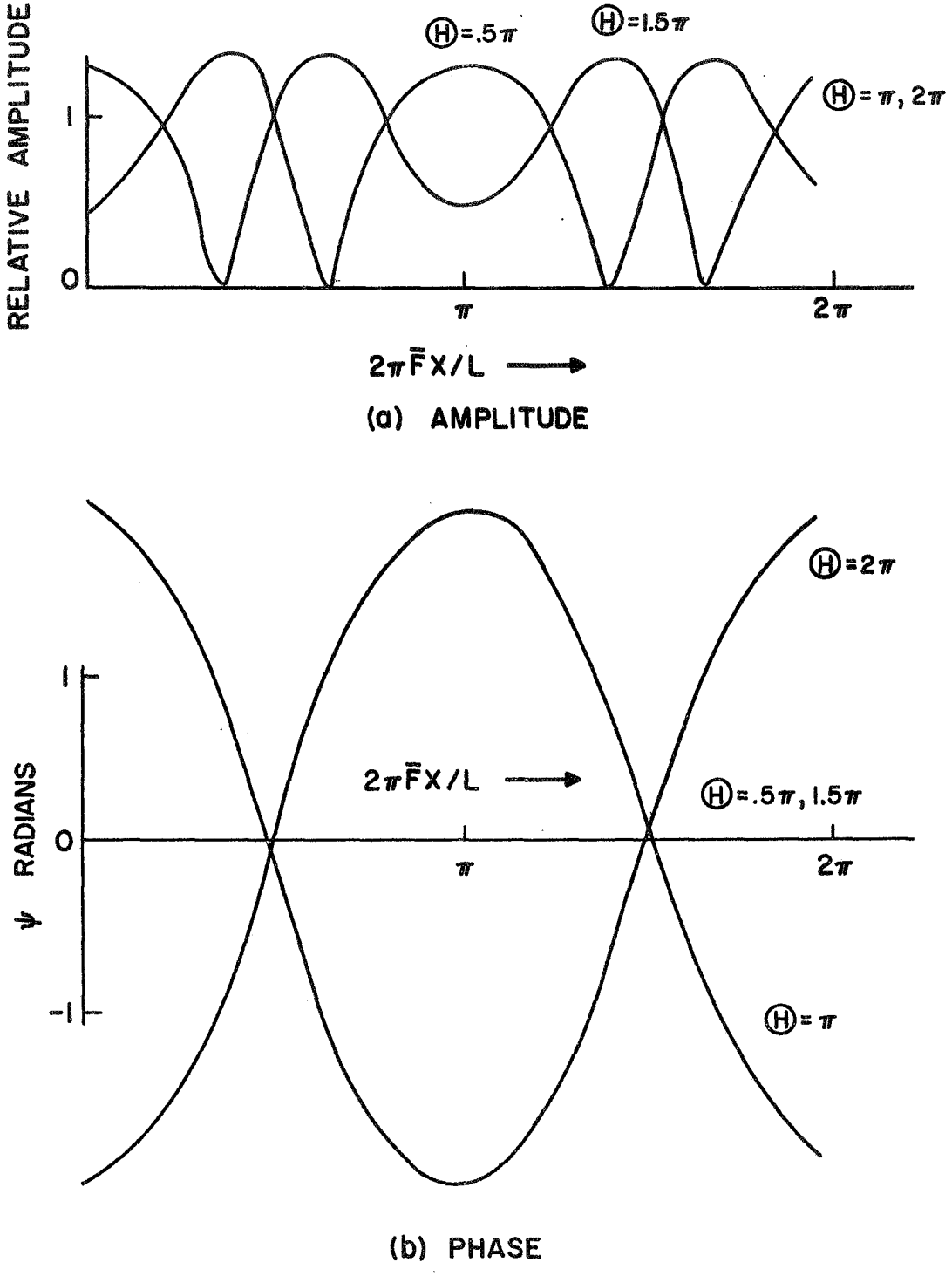


Figure 8. Diffraction Patterns Produced by a Screen with $\phi_0$ of 2. Radians for Particular Values of $\Theta$

It was of interest to determine the smallest values of $\phi_0$ which will produce deep nulls in the amplitude pattern in the appropriate distance range of $\Theta$. It was determined that, when $\phi_0$ was greater than 0.8 radians, notches to zero could be produced in amplitude although the depth and position of these notches are strong function of $\Theta$. As notches in the amplitude pattern generally occur when the in-phase and quadrature terms change sign together, a rapid variation in the phase pattern usually occurs in conjunction with a notch in the amplitude pattern. As $\phi_0$ becomes larger, amplitude nulls become more frequent and the region of $\Theta$, where the phase patterns appear sinusoidal, becomes smaller. Some examples of phase and amplitude patterns where $\phi_0$ has become increasingly larger are shown in Figures 6 through 10.

In conclusion, it is noted that as $\phi_0$ is increased from 0.5 radians to 4.0 radians, significant changes occur in both the phase and amplitude patterns. The higher order terms become increasingly significant and the amplitude pattern for these terms develops closer to the screen. The interval, measured with respect to $\Theta$ over which the phase pattern appears sinusoidal, is reduced as $\phi_0$ is increased while it expands around the points $N\pi/2$, N odd, until it only exists in narrow bands around $\Theta = N\pi$. The notches which develop in the amplitude patterns are strongly dependent on both $\phi_0$ and $\Theta$. Though the patterns may have most of their energy at the higher frequencies, the spatial period does not change with increasing $\phi_0$. If correlation functions are obtained for the phase and amplitude patterns that develop behind these non-weak screen, these correlation functions will differ for every value of $\Theta$.

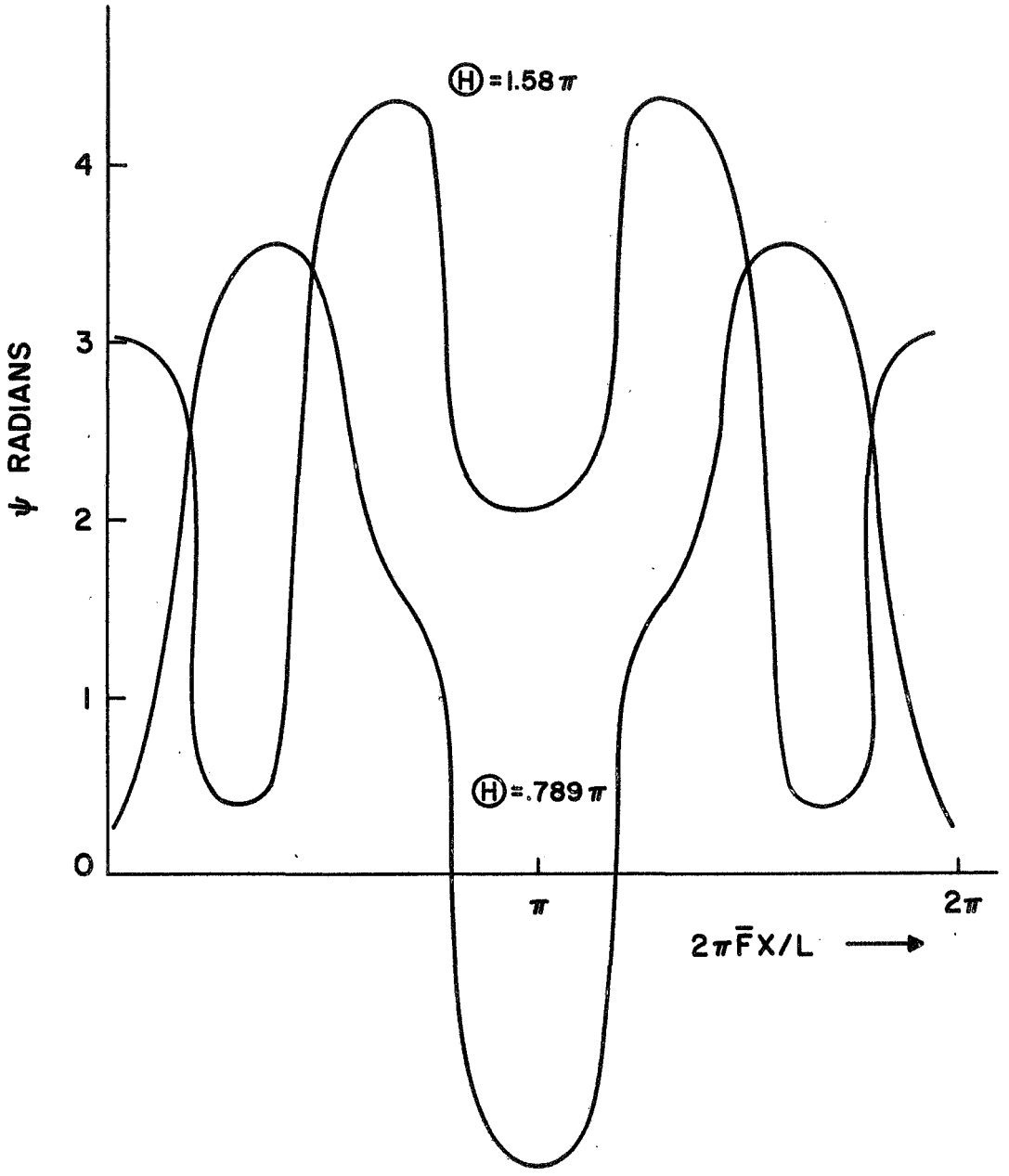


Figure 9. Phase Diffraction Patterns Produced by a Screen with $\phi_0$ of 4. Radians

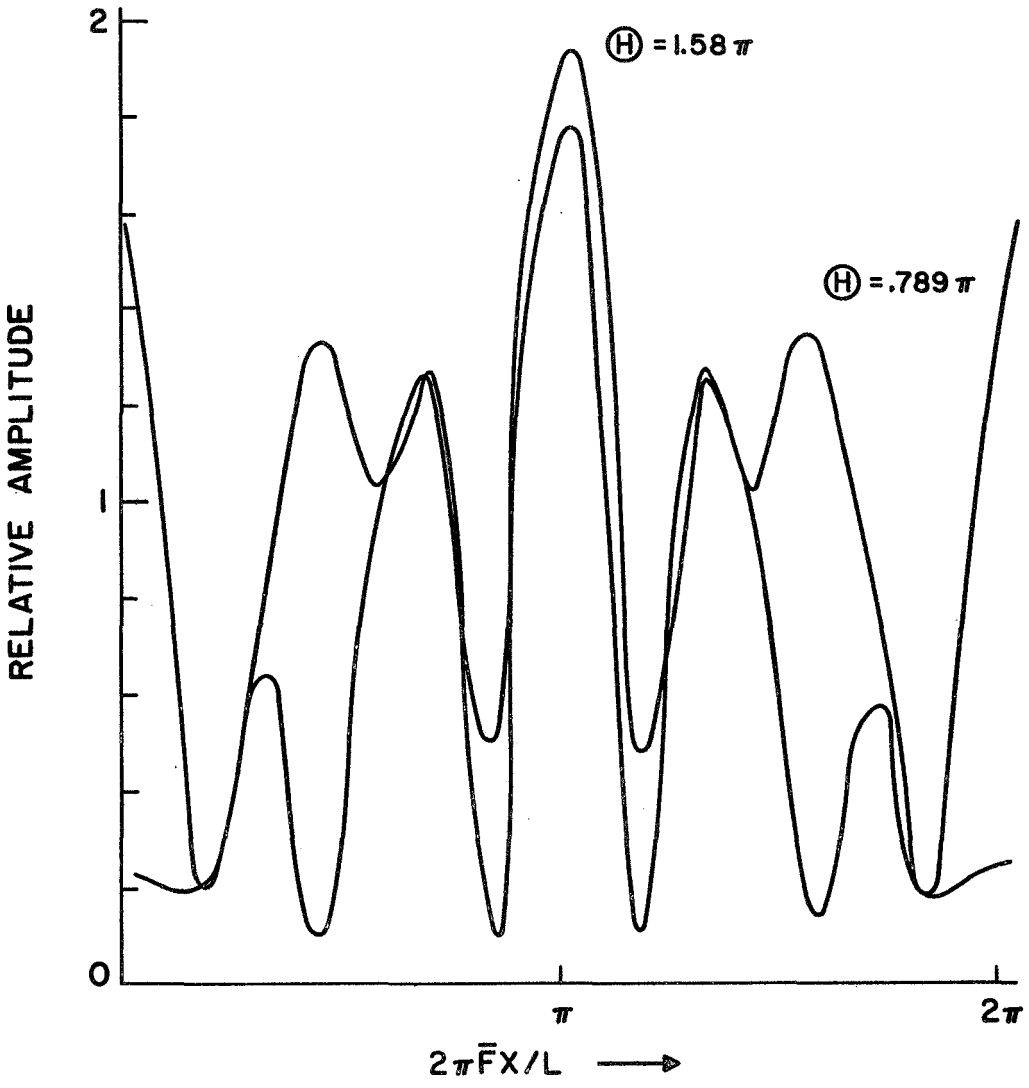


Figure 10. Amplitude Diffraction Patterns Produced by a Screen with $\phi_0$ of 4. Radians

## 2.3 The Weak Two-Dimensional Screen

When the phase modulation along the screen is a function of two orthogonal directions, $X_0$ , $Y_0$ , that are normal to $Z$ , then instead of 2-1, for the angular spectrum:

$$P(S_1, S_2) = \int_{-\infty}^{\infty}\int_{-\infty}^{\infty} E(X_0, Y_0)\, e^{-j2\pi\,(S_1X_0 + S_2Y_0)}\, dX_0 dY_0 \qquad (2\text{-}22)$$

Here $S_1$ and $S_2$ are the direction cosines of the scattered wave normal in the $X_0$ and $Y_0$ directions respectively. If the modulation is weak,

$$E(X_0, Y_0) = e^{j\phi_0(X_0, Y_0)} \approx 1 + j\phi_0 \cos\frac{2\pi X_0}{L_1} \cos\frac{2\pi Y_0}{L_2} \qquad (2\text{-}23)$$

or

$$E(X_0, Y_0) = 1 + \frac{j\phi_0}{4}\left[e^{j2\pi\left(\frac{X_0}{L_1} + \frac{Y_0}{L_2}\right)} + e^{-j2\pi\left(\frac{X_0}{L_1} + \frac{Y_0}{L_2}\right)} + e^{j2\pi\left(\frac{X_0}{L_1} - \frac{Y_0}{L_2}\right)} + e^{-j2\pi\left(\frac{X_0}{L_1} - \frac{Y_0}{L_2}\right)}\right] \qquad (2\text{-}24)$$

Immediately above the screen at $X_0, Y_0$ , the phase of the incident wave is:

$$e^{\frac{j2\pi Z_0}{\lambda}}\; e^{\frac{j\pi X_0^2}{\lambda Z_0}}\; e^{\frac{j\pi Y_0^2}{\lambda Z_0}}$$

The integral 2-22 including the phase terms for a finite $Z_0$ then becomes:

$$P(S_1, S_2) = e^{\frac{j2\pi Z_0}{\lambda}} \int_{-\infty}^{\infty}\int_{-\infty}^{\infty} \left\{ 1. + \frac{j\phi_0}{4} \left[ e^{j2\pi\left(\frac{X_0}{L_1} + \frac{Y_0}{L_2}\right)} + e^{-j2\pi\left(\frac{X_0}{L_1} + \frac{Y_0}{L_2}\right)} + e^{j2\pi\left(\frac{X_0}{L_1} - \frac{Y_0}{L_2}\right)} + e^{-j2\pi\left(\frac{X_0}{L_1} - \frac{Y_0}{L_2}\right)} \right] \right\} e^{\frac{j\pi X_0^2}{\lambda Z_0}} e^{\frac{j\pi Y_0^2}{\lambda Z_0}} e^{-\frac{j2\pi}{\lambda}(S_1X_0 + S_2Y_0)} dX_0 dY_0 \qquad (2\text{-}25)$$

On integrating with respect to $X_0$ and $Y_0$, the angular spectrum at the screen is obtained:

$$P(S_1, S_2) = e^{\frac{j2\pi Z_0}{\lambda}} (j\lambda Z_0) \left\{ e^{\frac{-j\pi Z_0}{\lambda}\left(S_1^2 + S_2^2\right)} \left[ 1 + e^{j\pi\lambda Z_0\left(\frac{1}{L_1^2} + \frac{1}{L_2^2}\right)} \left( e^{j2\pi Z_0\left(\frac{S_1}{L_1} + \frac{S_2}{L_2}\right)} + e^{-j2\pi Z_0\left(\frac{S_1}{L_1} + \frac{S_2}{L_2}\right)} + e^{j2\pi Z_0\left(\frac{S_1}{L_1} - \frac{S_2}{L_2}\right)} + e^{-j2\pi Z_0\left(\frac{S_1}{L_1} - \frac{S_2}{L_2}\right)} \right) \right] \right\} \qquad (2\text{-}26)$$

The expression for the field at X , Y , Z is then expressed as:

$$E(X, Y, Z) = \frac{e^{\frac{j2\pi Z}{\lambda}}}{\lambda^2} \int_{-\infty}^{\infty}\int_{-\infty}^{\infty} P(S_1, S_2)\, e^{\frac{j2\pi S_1 X}{\lambda}}\, e^{-\frac{j\pi Z S_1^2}{\lambda}} \tag{2-27}$$

$$e^{\frac{j2\pi S_2 Y}{\lambda}}\, e^{-\frac{J\pi S_2^2}{\lambda}}\, dS_1 dS_2$$

Upon integrating and collecting terms, the expression for E(X, Y, Z) is found to be:

$$E(X, Y, Z) = e^{\frac{j2\pi}{\lambda}(Z + Z_0)}\, e^{\frac{j2\pi(X^2 + Y^2)}{\lambda (Z + Z_0)}} \left\{\bar{F}\right\} \left\{1. + \frac{j\phi_0}{2}\right.$$

$$e^{-j\pi\lambda\bar{F}Z\left(\frac{1}{L_1^2} + \frac{1}{L_2^2}\right)} \left[\cos 2\pi\bar{F}\left(\frac{X}{L_1} + \frac{Y}{L_2}\right)\right. \tag{2-28}$$

$$\left.\left. + \cos 2\pi\bar{F}\left(\frac{X}{L_1} - \frac{Y}{L_2}\right)\right]\right\}$$

The amplitude of all the terms in the pattern has been reduced by $\bar{F}$ , the projection factor of the diverging rays.

When the multipliers outside the brackets of 2-28 which modify all terms are removed, and the position of $L_1$ is changed to simplify comparison with the patterns of a one-dimensional screen, 2-28 results in the following in-phase and quadrature terms.

In-Phase

$$1 + \frac{\phi_0}{2} \sin \frac{\pi\lambda\bar{F}Z}{L_1^2}\left(1. + \frac{L_1^2}{L_2^2}\right)\left[\cos \frac{2\pi\bar{F}}{L_1}\left(X + \frac{L_1 Y}{L_2}\right) + \cos \frac{2\pi\bar{F}}{L_1}\left(X - \frac{L_1}{L_2} Y\right)\right] \tag{2-29}$$

Quadrature

$$\frac{\phi_0}{2} \cos \frac{\pi\lambda\bar{F}Z}{L_1^2}\left(1. + \frac{L_1^2}{L_2^2}\right)\left[\cos \frac{2\pi\bar{F}}{L_1}\left(X + \frac{L_1}{L_2} Y\right) + \cos \frac{2\pi\bar{F}}{L_1}\left(X - \frac{L_1}{L_2} Y\right)\right] \tag{2-30}$$

Using the same approximations for the weak screen used for 2-13 and 2-14 results in the following phase and amplitude patterns behind the two-dimensional screen:

$$\psi \approx \frac{\phi_0}{2} \cos \frac{\pi\lambda\bar{F}Z}{L_1^2}\left(1 + \frac{L_1^2}{L_2^2}\right)\left[\cos \frac{2\pi\bar{F}}{L_1}\left(X + \frac{L_1}{L_2} Y\right) + \cos \frac{2\pi\bar{F}}{L_1}\left(X - \frac{L_1}{L_2} Y\right)\right] \tag{2-31}$$

$$A = 1. + \frac{\phi_0}{2} \sin \frac{\pi\lambda\bar{F}Z}{L_1^2} \left(1 + \frac{L_1^2}{L_2^2}\right) \left[\cos \frac{2\pi\bar{F}}{L_1} \left(X + \frac{L_1}{L_2} Y\right) + \cos \frac{2\pi\bar{F}}{L_1} \left(X - \frac{L_1}{L_2} Y\right)\right] \tag{2-32}$$

Comparison of 2-31 and 2-32 with 2-13 and 2-14 reveals that if $L_1 = L_2$ the amplitude pattern will develop in one-half the distance required by the one-dimensional pattern. However, when $L_2 = 5L_1$, the two-dimensional pattern does not develop until $\bar{F}Z$ attains 0.95 of the value required by the one-dimensional amplitude pattern for similar development. Thus, when the scale size in one direction is increase, the two-dimensional pattern will develop no closer to the screen than does the one-dimensional pattern. Also, if the particular cases where $X = \pm Y$ are neglected, motion along the pattern reveals two spatial frequencies. These frequencies may vary from near zero to twice the frequency of a one-dimensional screen as different combinations of $L_1$, $L_2$, X, and Y are investigated. When the patterns are sampled primarily along the direction of the larger scale size, the spatial frequencies are lower.

Thus it is observed that when a one-dimensional, weak, cosinusoidal, phase-modulating screen is extended to the two-dimensional case, there are significant differences in the spatial properties of the pattern E ( X , Y , Z ). Also, the distance at which amplitude patterns develop may be reduced by one-half.

However, the differences observed in the temporal properties of the pattern $E(X, Y, Z, t)$, at a fixed receiving point as a radiating satellite passes above the screen, may be minor. These properties depend on how the screen is crossed. The observed spatial frequencies may be low, high, or single depending on the satellite path. Similarly, a small-scale, one-dimensional screen may produce low spatial frequencies at the observation point if it is crossed in a direction oblique to the scale size. The complete periods of the patterns observed below a regular two-dimensional screen may become considerably longer than those the largest scale size would produce; the path across the screen must return to a similar point in the pattern to complete the period.

## 2.4 The Two-Dimensional Screen When Modulation is Not Weak

In this case, the phase modulation at the screen can be expressed as:

$$e^{j\phi_0 \cos \frac{2\pi X_0}{L_1} \cos \frac{2\pi Y_0}{L_2}} \tag{2-33}$$

Let $A = \frac{2\pi X_0}{L_1}$ and $B = \frac{2\pi Y_0}{L_2}$

Then:

$$e^{j\phi_0 \cos \frac{2\pi X_0}{L_1} \cos \frac{2\pi Y_0}{L_2}} = \cos\left\{\frac{\phi_0}{2}\left[\cos(A+B) + \cos(A-B)\right]\right\}$$

$$+ j \sin\left\{\frac{\phi_0}{2}\left[\cos(A+B) + \cos(A-B)\right]\right\}$$

When the expansions given by 2-17 and 2-18 are used for $\phi_0 \geq 1$ radian , the three significant Bessel functions have the following range of values:

$$1.000 \geq J_0\left(\frac{\phi_0}{2}\right) \geq 0.9385$$

$$0.2423 \geq J_1\left(\frac{\phi_0}{2}\right) \geq 0.0$$

$$0.0306 \geq J_2\left(\frac{\phi_0}{2}\right) \geq 0.0$$

The higher order terms are neglected.

Expression 2-33 may be written as a sum of products:

$$e^{j\phi_0 \cos \frac{2\pi X_0}{L_1} \cos \frac{2\pi Y_0}{L_2}} = \cos\left[\frac{\phi_0}{2}\cos(A+B)\right] \cos\left[\frac{\phi_0}{2}\cos(A-B)\right]$$

$$- \sin\left[\frac{\phi_0}{2}\cos(A+B)\right] \sin\left[\frac{\phi_0}{2}\cos(A-B)\right] \qquad (2\text{-}34)$$

$$+ j \sin\left[\frac{\phi_0}{2}\cos(A+B)\right] \cos\left[\frac{\phi_0}{2}\cos(A-B)\right]$$

$$+ j \cos\left[\frac{\phi_0}{2}\cos(A+B)\right] \sin\left[\frac{\phi_0}{2}\cos(A-B)\right]$$

When a Bessel function expansion is made for each term and the multiplication is completed, if all Bessel function terms up to the second power are retained, the screen pattern becomes:

$$J_0^2\left(\frac{\phi_0}{2}\right) - 2J_0\left(\frac{\phi_0}{2}\right) J_2\left(\frac{\phi_0}{2}\right) [\cos(2A+2B) + \cos(2A-2B)]$$

$$- 2J_1^2\left(\frac{\phi_0}{2}\right) [\cos 2A + \cos 2B] - 2J_2^2\left(\frac{\phi_0}{2}\right) [\cos 4A + \cos 4B]$$

$$+ j\left\{2J_0\left(\frac{\phi_0}{2}\right) J_1\left(\frac{\phi_0}{2}\right) [\cos(A+B) + \cos(A-B)]\right. \qquad (2\text{-}35)$$

$$- 2J_1\left(\frac{\phi_0}{2}\right) J_2\left(\frac{\phi_0}{2}\right) [\cos(3A+B) + \cos(3A-B)]$$

$$+ \cos(A+3B) + \cos(-A+3B)$$

When $\phi_0$ is less than one radian, the $J_2^2\left(\frac{\phi_0}{2}\right)$ and $J_1\left(\frac{\phi_0}{2}\right) J_2\left(\frac{\phi_0}{2}\right)$ terms may be neglected. Then, using the same integration applied to the weak two-dimensional screen, the diffraction pattern $E(X, Y, Z)$ may be obtained. For the in-phase components, it has (see following page):

$$J_0^2\left(\frac{\phi}{2}\right) + 2J_0\left(\frac{\phi}{2}\right) J_1\left(\frac{\phi}{2}\right) \sin \frac{\pi\lambda\bar{F}Z}{L_1^2}\left(1 + \frac{L_1^2}{L_2^2}\right)\left[\cos \frac{2\pi\bar{F}}{L_1}\left(X + \frac{L_1}{L_2}Y\right)\right.$$

$$\left. + \cos \frac{2\pi\bar{F}}{L_1}\left(X - \frac{L_1}{L_2}Y\right)\right] \qquad (2\text{-}36)$$

$$- 2J_1^2\left(\frac{\phi}{2}\right)\left[\cos \frac{4\pi\lambda\bar{F}Z}{L_1^2} \cos \frac{4\pi\bar{F}X}{L_1} + \cos \frac{4\pi\lambda\bar{F}Z}{L_2^2} \cos \frac{4\pi\bar{F}Y}{L_2}\right]$$

$$- 2J_0\left(\frac{\phi}{2}\right) J_2\left(\frac{\phi}{2}\right) \cos \frac{4\pi\lambda\bar{F}Z}{L_1^2}\left(1 + \frac{L_1^2}{L_2^2}\right)\left[\cos \frac{4\pi\bar{F}}{L_1}\left(X + \frac{L_1}{L_2}Y\right)\right.$$

$$\left. + \cos \frac{4\bar{F}\pi}{L_1}\left(X - \frac{L_1}{L_2}Y\right)\right]$$

and for the quadrature term:

$$2J_0\left(\frac{\phi}{2}\right) J_1\left(\frac{\phi}{2}\right) \cos \frac{\pi\lambda\bar{F}Z}{L_1^2}\left(1 + \frac{L_1^2}{L_2^2}\right)\left[\cos \frac{2\pi\bar{F}}{L_1}\left(X + \frac{L_1}{L_2}Y\right) + \cos \frac{2\pi\bar{F}}{L_1}\left(X - \frac{L_1}{L_2}Y\right)\right]$$

$$+ J_1^2\left(\frac{\phi}{2}\right)\left[\sin \frac{4\pi\lambda\bar{F}Z}{L_1^2} \cos \frac{4\pi\bar{F}X}{L_1} + \sin \frac{4\pi\lambda\bar{F}Z}{L_2^2} \cos \frac{4\pi\bar{F}Y}{L_2}\right] \qquad (2\text{-}37)$$

$$+ 2J_0\left(\frac{\phi}{2}\right) J_2\left(\frac{\phi}{2}\right) \sin \frac{4\pi\bar{F}Z}{L_1^2}\left(1 + \frac{L_1^2}{L_2^2}\right)\left[\cos \frac{4\pi\bar{F}}{L_1}\left(X + \frac{L_1}{L_2}Y\right)\right.$$

$$\left. + \cos \frac{4\pi\bar{F}}{L_1}\left(X - \frac{L_1}{L_2}Y\right)\right]$$

As previously, the same frequencies exist in the in-phase and the quadrature terms. The phase of the diffraction pattern at the ground, $\psi$, contains all of these terms.

When the amplitude and phase patterns are calculated using expressions similar to 2-11 and 2-12, but including all of the terms of 2-36 and 2-37, these patterns contain some components that are two or three times the spatial frequency which existed at the screen. Also, there are terms present that depend on X and Y above.

To determine some of the diffraction patterns which could form behind the two-dimensional cosine phase screen, where the modulation is less than one radian, the in-phase and quadrature terms have been calculated using a simulation program. These were then combined to obtain the phase and amplitude patterns.

A number of patterns were obtained for transmitted frequencies of 20 and 40 MHz. Some of these patters are shown in Figures 11 and 12; the patterns are plotted versus $\overline{FX}/L_1$, the component of motion along the small-scale axis. The $\Delta S$ value is the total displacement across the screen.

When these patterns are compared with those which develop behind a one-dimensional screen, it is observed that the multiple frequencies are more in evidence for the two-dimensional screen. Also, because of the oblique paths taken across the regular screen, the spatial period becomes, in general, several times longer than the scale size.

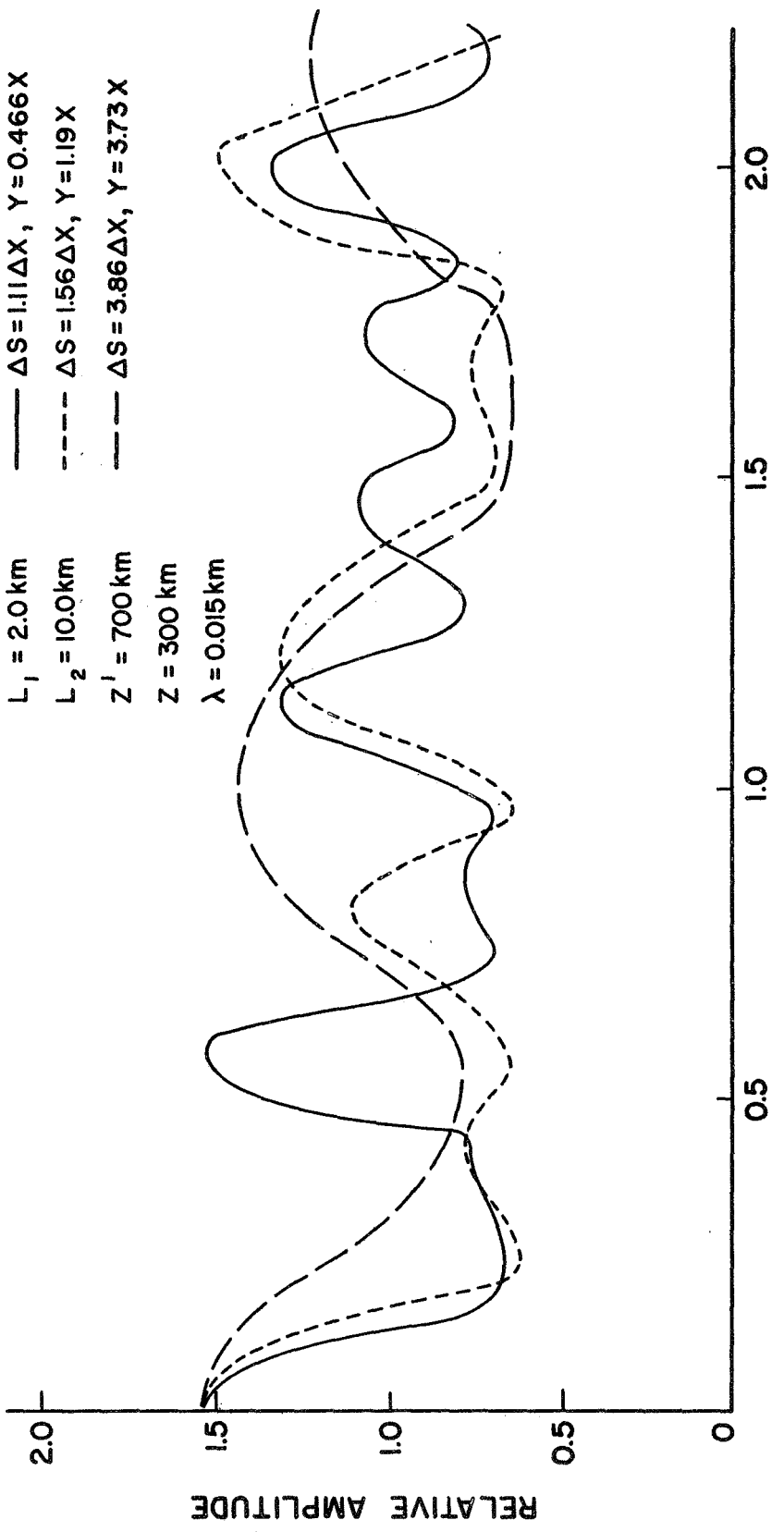


Figure 11. Amplitude Diffraction Patterns Produced by a Two-Dimensional Screen with $\phi_0$ of 1 Radian

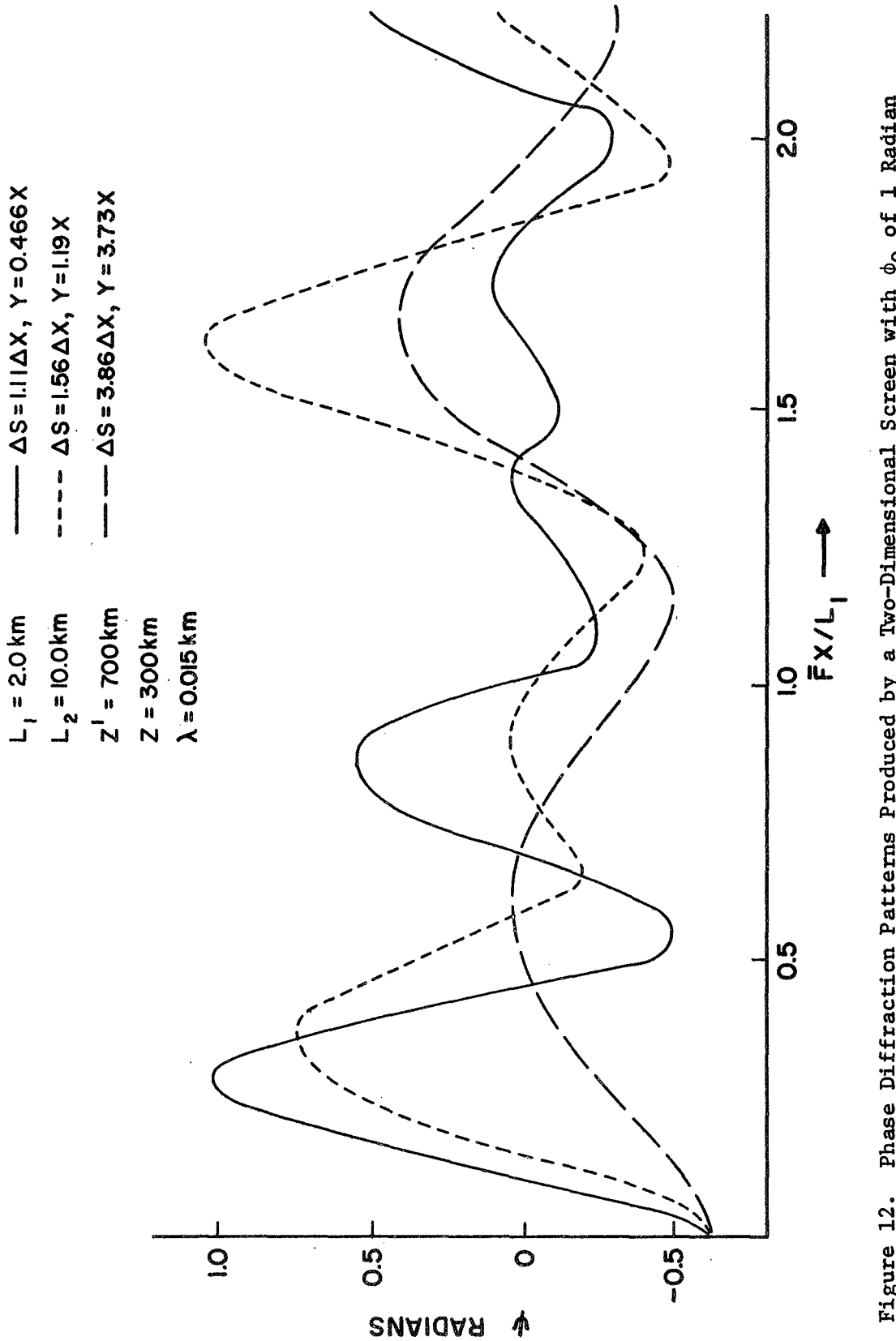


Figure 12. Phase Diffraction Patterns Produced by a Two-Dimensional Screen with $\phi_0$ of 1 Radian

For the same peak screen modulation, $\phi_0$ , the occurrence of deep nulls is less frequent. This is due in part to the average modulating intensity of the two-dimensional screen being reduced by a factor of $2/\pi$ as compared to the one-dimensional screen. Also, there is an increase in the number of spatial frequencies in the screen; the discrete combinations of X , Y , and $\overline{FZ}$ , required to produce deep notches, occur less frequently for arbitrary passes across the two-dimensional screen. Thus, larger values of $\phi_0$ are required to produce equivalent scintillation ratios for the amplitude patterns which develop behind two-dimensional screens. The one-dimensional screen is the most efficient in this respect.

## 2.5 Screen Consisting of An Array of Discrete Blobs

The previous sections have all considered phase-modulating screens where the variation of phase was a continuous function of one or two dimensions along the screen. If the screen is made to consist of a number of blobs, the individual blobs may be separated by regions which have a constant phase modulation. For this configuration, it is desirable to have a modulation function which possesses zero derivatives at the center and at the limits of the blob. A gaussian function does not fulfill these requirements; it has derivatives which are zero at the center of the blob and at an infinite distance from its center. The desired modulation function also should allow for a variable spacing of the blobs in a

two-dimensional screen. Such a function is a series of cosine-squared pulses which are considered first in a one-dimensional screen:

$$\phi(X_0) = \begin{cases} 0, & -\frac{d_1}{2} \le X_0 < -L_1 \\ \phi_0 \cos \frac{2\pi X_0}{2L_1}, & -L_1 \le X_0 < L_1 \\ 0, & L_1 < X_0 \le \frac{d_1}{2} \end{cases} \tag{2-38}$$

The function $\phi(X_0)$ as defined by 2-38 is an even function of period $d_1$ ; thus it can be represented by a Fourier series of the form:

$$\phi(X_0) = a_0 + a_1 \cos \frac{2\pi X_0}{d_1} + a_2 \cos \frac{4\pi X_0}{d_1} + \ldots . \tag{2-39}$$

On solving for the Fourier coefficients, 2-39 is expressed as:

$$\phi(X_0) = \phi_0 \left\{ \frac{L_1}{d_1} + \sum_{n=1}^{\infty} \frac{\sin \frac{2n\pi L_1}{d_1}}{n\pi \left[1 - \left(\frac{2nL_1}{d_1}\right)^2\right]} \cos \frac{2n\pi X_0}{d_1} \right\} \tag{2-40}$$

The coefficients for the harmonic components contain, as a parameter, $\frac{2L_1}{d_1}$ , the ratio of blob diameter to center spacing. The normalized coefficients (the largest value is made equal to 1) are plotted versus $n$ in Figure 13 with the quantity $2L_1/d_1$ a parameter. From four to seven significant terms are required for the series representation; in

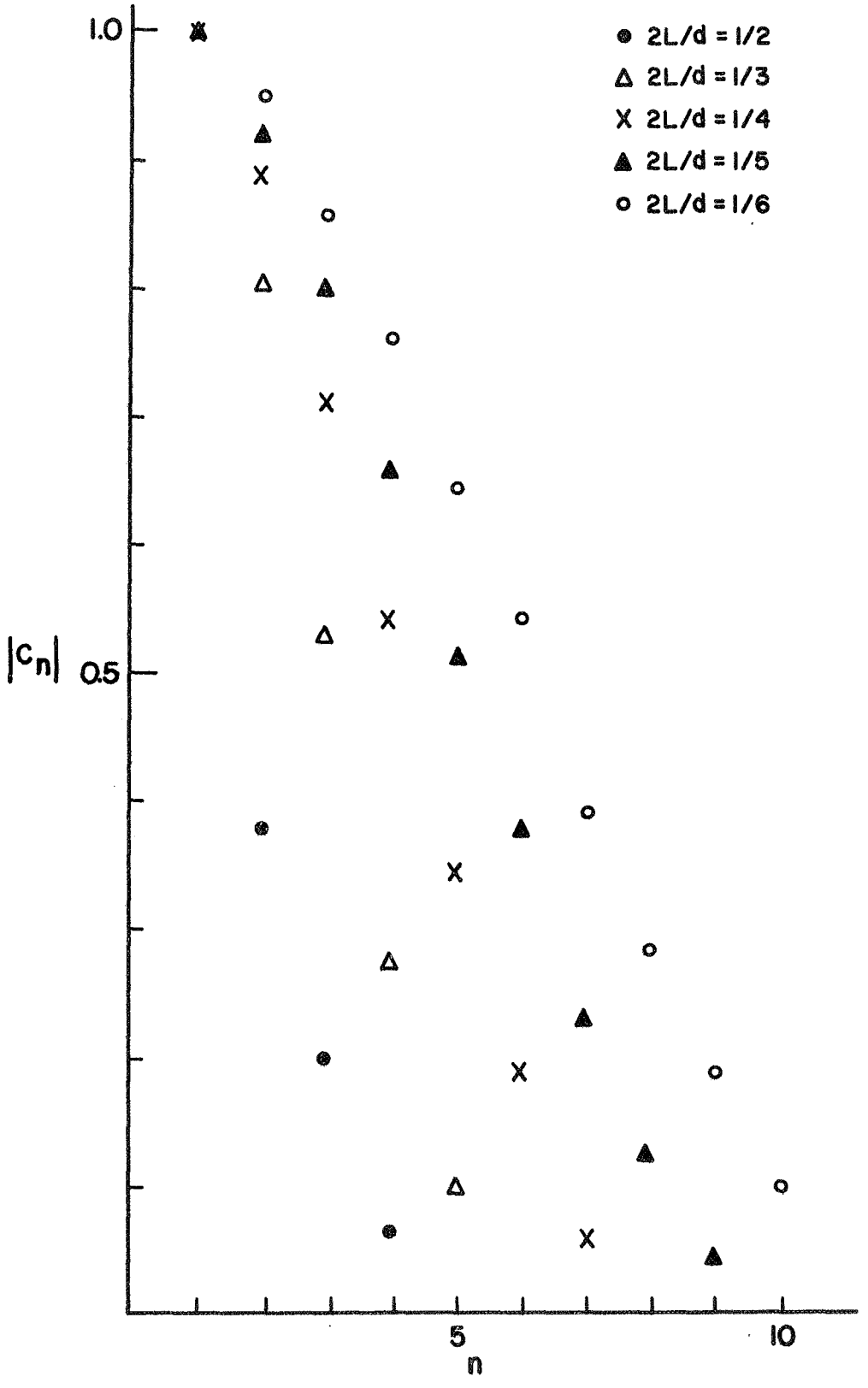


Figure 13. Normalized Coefficients ($C_n$) versus n with 2L/d a Parameter

every case shown, $2L_1/d_1$ from 1/2 to 1/6, the first harmonic has the largest amplitude.

If the phase modulation is assumed weak, the one-dimensional screen modulation function may be expressed as:

$$\phi(X_0) = 1 + j\phi_0 \frac{L_1}{d_1} + j\phi_0 \sum_{n=1}^{N} C_n \cos \frac{2n\pi X_0}{d_1} \tag{2-41}$$

The average component, which is similar to the effects of a uniform slab, produces a mean phase shift for the undiffracted component. If each of the terms are manipulated using the methods of 2.1, the in-phase and quadrature components for the pattern at the ground, when the multiplier, $\overline{F}$ , and the phase of the main component are removed, become:

In-Phase

$$1 + \phi_0 \sum_{n=1}^{N} C_n \sin \frac{n^2 \pi \lambda \overline{F} Z}{d_1^2} \cos \frac{n 2\pi \overline{F} X}{d_1} \tag{2-42}$$

Quadrature

$$\phi_0 \sum_{n=1}^{N} C_n \cos \frac{n^2 \pi \lambda \overline{F} Z}{d_1^2} \cos \frac{n 2\pi F X}{d_1} + \phi_0 \frac{L_1}{d_1}$$

When this model is used for the thin screen, the mean value of the phase shift, which the wave front makes in passing through the screen, is $\phi_0 \frac{L_1}{d_1}$ . Since this constant term does not contribute to the diffraction pattern, it is not included in the expressions for pattern development.

The phase and amplitude patterns which result from 2-42 are:

$$\psi = \phi_0 \sum_{n=1}^{N} C_n \cos \frac{n^2 \pi \lambda \bar{F} Z}{d_1^2} \cos \frac{n 2\pi \bar{F} X}{d_1}$$

$$A = 1 + \phi_0 \sum_{n=1}^{N} C_n \sin \frac{n^2 \pi \lambda \bar{F} Z}{d_1^2} \cos \frac{n 2\pi \bar{F} X}{d_1} \qquad (2\text{-}43)$$

If the value of $\phi_0$ is increased to permit consideration of second order terms,

$$\psi = \phi_0 \sum_{n=1}^{N} C_n \cos \frac{n^2 \pi \lambda \bar{F} Z}{d_1^2} \cos \frac{n 2\pi \bar{F} X}{d}$$

$$- \frac{\phi_0^2}{4} \sum_{n=1}^{N} C_n^2 \sin \frac{n^2 2\pi \lambda \bar{F} Z}{d_1^2} \left(1 + \cos \frac{n 4\pi \bar{F} X}{d}\right)$$

and

$$A = 1 + \phi_0 \sum_{n=1}^{N} C_n \sin \frac{n^2 \pi \lambda \bar{F} Z}{d_1^2} \cos \frac{n 2\pi \bar{F} X}{d}$$

$$+ 1/4 \ \phi_0^2 \sum_{n=1}^{N} C_n^2 \left(1 + \cos \frac{n 4\pi \bar{F} X}{d}\right)$$

$$+ \frac{\phi_0^2}{2} \sum_{n=1}^{N-1} \sum_{m=n+1}^{N} C_n C_m \left(\sin \frac{n^2 \pi \lambda \bar{F} Z}{d_1^2} \sin \frac{m^2 \pi \lambda \bar{F} Z}{d_1^2}\right) \cdot \qquad (2\text{-}44)$$

$$\left[\cos \frac{2\pi \bar{F}}{d} (n + m) X + \cos \frac{2\pi \bar{F}}{d} (n - m) X\right]$$

Expressions 2-44 show that if the screen consisting of spaced anomalies has a value of $\phi_0$ large enough for second order terms to be considered ($0.3 \leq \phi_0 \leq 0.5$), higher frequency components will be observed in the amplitude pattern before they appear in the phase pattern. Because the amplitude is the sum of the two orthogonal components, the squared terms involved contain a number of additions. For example, for $N = 6$, the sixth, seventh, and eighth harmonics each has three contributing terms. Because each of these terms has a coefficient which is a function of $\overline{FZ}$, certain distances from the screen may make them as large as the first harmonic. In particular, small values of $\overline{FZ}$ tend to increase the relative importance of the higher harmonics.

The discrete blobs may have a cosinusoidal shape in the two dimensions, $X_0Y_0$. In this case their Fourier series representation becomes a product function:

$$\text{Let} \quad \phi_0(X_0, Y_0) = e^{j\phi_0} \left[f_1(X_0)\ f_2(Y_0)\right] \tag{2-45}$$

$$\text{where} \quad f_1(X_0) = \frac{L_1}{d_1} + \sum_{n=1}^{N} \frac{\sin \frac{n2\pi L_1}{d_1}}{n\pi\left[1 - \frac{2nL_1}{d_1}^2\right]} \cos \frac{n2\pi X_0}{d_1} \tag{2-46}$$

$$f_1(Y_0) = \frac{L_2}{d_2} + \sum_{m=1}^{M} \frac{\sin \frac{m2\pi L_2}{d_2}}{m\pi\left[1 - \frac{2mL_2}{d_2}^2\right]} \cos \frac{m2\pi Y_0}{d_2}$$

When $C_n$ and $C_m$ are used for the Fourier coefficients, 2-45 becomes for the weak screen:

$$\phi(X_0, Y_0) = 1 + j\phi_0 \left(\frac{L_1}{d_1} + \frac{L_2}{d_2}\right) + j\phi_0 \left[\sum_{n=1}^{N} C_n \cos \frac{n2\pi X_0}{d_1} + \sum_{m=1}^{M} C_m \cos \frac{m2\pi Y_0}{d_2}\right] \tag{2-47}$$

If the methods employed to obtain 2-29 and 2-30 are used for 2-47, the in-phase and quadrature components are found at a distance, $Z$, from the screen:

In-Phase

$$1 + \frac{\phi_0}{2} \sum_{n=1}^{N} \sum_{m=1}^{M} C_n C_m \sin \frac{\pi\lambda F Z}{d_1^2} \left(n^2 + \frac{m^2 d_1^2}{d_2^2}\right) \cdot \left[\cos 2\pi\bar{F} \left(\frac{nX}{d_1} + \frac{mY}{d_2}\right) + \cos 2\pi\bar{F} \left(\frac{nX}{d_1} - \frac{mY}{d_2}\right)\right] \tag{2-48}$$

Quadrature

$$\frac{\phi_0}{2} \sum_{n=1}^{N} \sum_{m=1}^{M} C_n C_m \cos \frac{\pi\lambda\bar{F} Z}{d_1^2} \left(n^2 + \frac{m^2 d_1^2}{d_2^2}\right) \left[\cos 2\pi\bar{F} \left(\frac{nX}{d_1} + \frac{mY}{d_2}\right) + \cos 2\pi\bar{F} \left(\frac{nX}{d_1} - \frac{mY}{d_2}\right)\right] \tag{2-49}$$

In the above expressions, when $L_1 = d_1$ and $L_2 = d_2$, only the $C_n$, $C_m$ for n=1 and m=1 are non-zero and they become identical to 2-29 and 2-30 which represent the continuous screen. If the blobs are moved apart such that two and three values of $C_n$ and $C_m$ are significant, the number of frequencies present in the patterns are increased from 2 to 8 and 18--the number of frequencies being equal to $2N^2$. In this situation the difference frequencies maintain the higher energy level at the low end of the spectrum.

A computer program was used to calculate the in-phase and quadrature terms of the diffraction pattern. These terms were then combined to obtain the amplitude and phase diffraction patterns. Different blob sizes and spacings were employed for the simulations, using transmitted frequencies of 20 and 40 MHz. Some of these patterns are shown in Figures 14 and 15. The independent parameters for the curves are the screen model, the distance to the screen, and the direction of travel across the screen. The directions are taken such that $Y = aX$ where a has values of 0.001, 2.5, 5.0, and 100. The two cases where motion is near parallel to $X_0$ or $Y_0$ show a periodic pattern. The oblique crossings of the screen show pauses between the scintillations which are observed at times in the records of satellite tracks. The phase patterns show proportionally more low frequency components; these components take a longer distance to develop in the amplitude patterns.

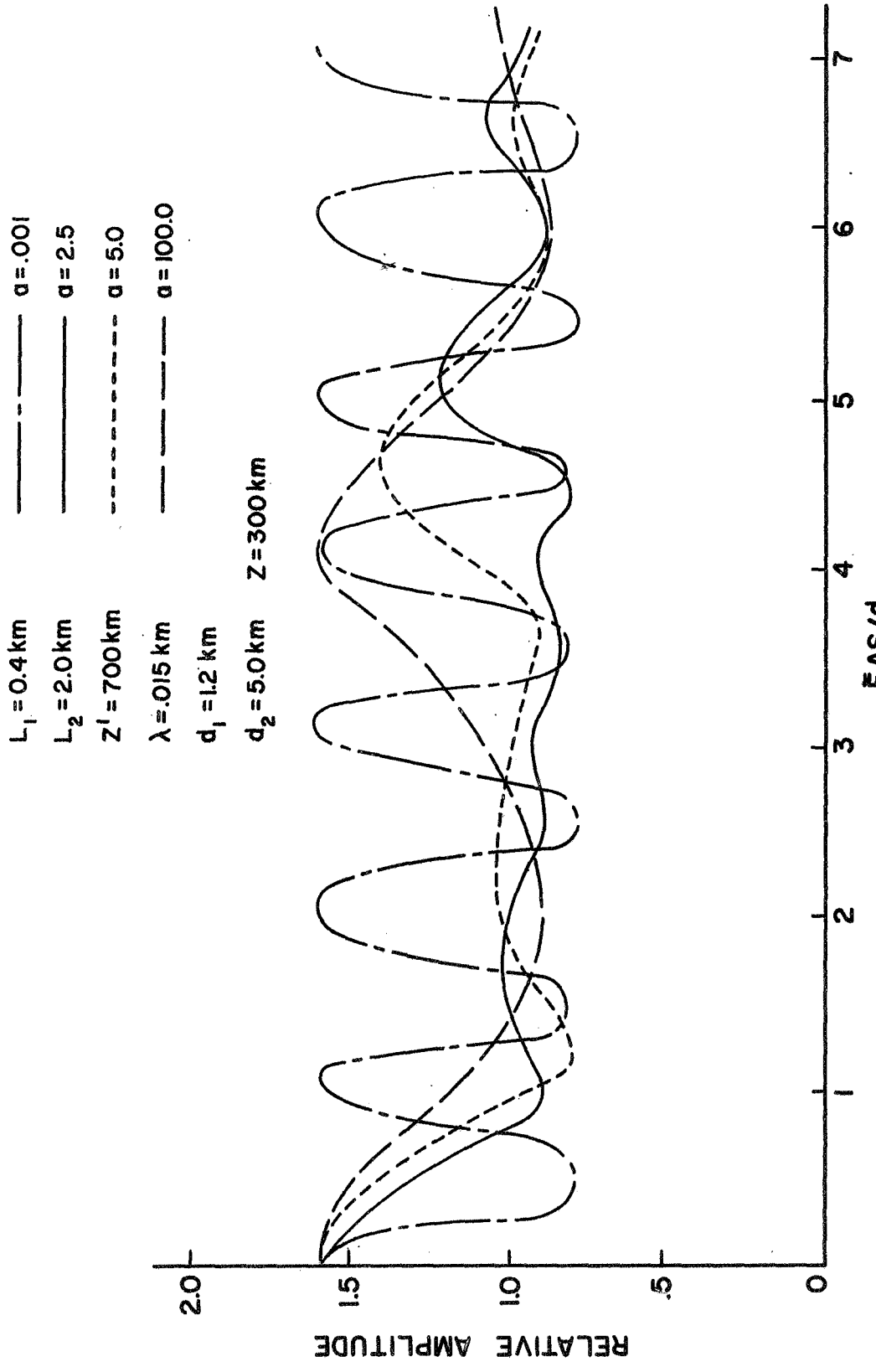


Figure 14. Amplitude Diffraction Patterns Produced by a Two-Dimensional Discrete Blob Screen; Blob Separation 1.2 and 5 km

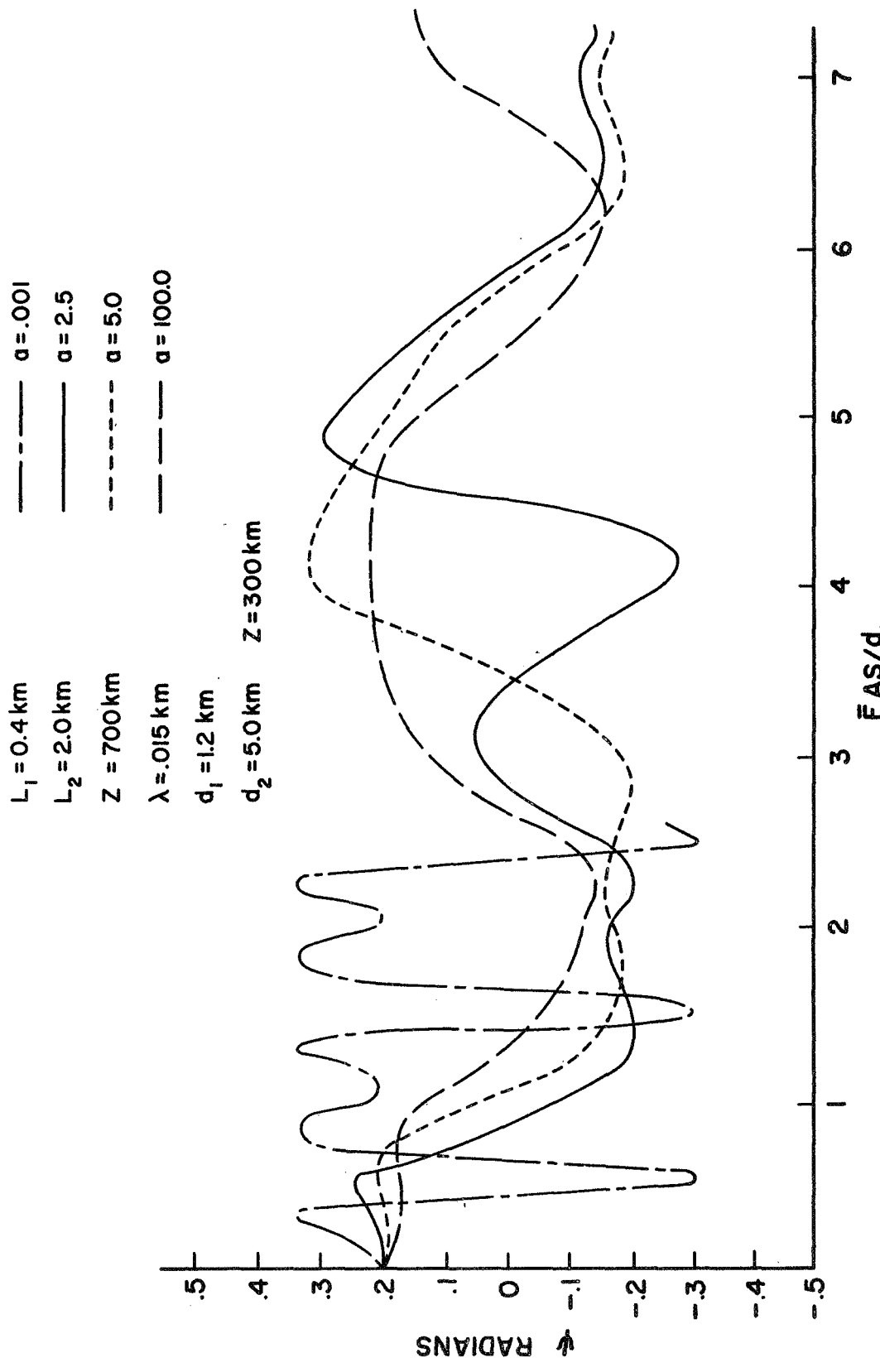


Figure 15. Phase Difference Diffraction Patterns Produced by a Two-Dimensional Discrete Blob Screen; Blob Separation 1.2 and 5. km

## 2.6 A Thick Screen

In the previous models, infinitely thin screens were used. For these screens, though multiple frequencies may be present, no amplitude variations exist when the wave emerges from the bottom. For ionospheric phase modulation, the screens have a finite thickness over which the modulation is imposed. To determine the effect of a screen having thickness, the diffraction patterns produced behind five thin screens which have a variable spacing, $Z_i$ , are investigated. Each layer in the multiple screen has its own scale size, $L_i$ , and modulation intensity, $\phi_i$ . At a distance, $Z_1$ , below the top layer of the complex field is:

$$E_1(X_1, Z_1) = \sqrt{F}\; e^{j2\pi \frac{\left(Z_1 + Z'\right)}{\lambda}}\; e^{\frac{j\pi X_1^2}{\lambda\left(Z_1 + Z'_1\right)}} \left[1. + {}_1 \sin \frac{\pi\lambda\overline{F}_1 Z}{L_1^2} \cos \frac{2\pi\overline{F}_1 X_1}{L_1} + j\phi_1 \cos \frac{\pi\lambda\overline{F}_1 Z_1}{L_1^2} \cos \frac{2\pi\overline{F}_1 X_1}{L_1}\right] \tag{2-50}$$

At distance $Z_1$ , a second screen exists and weakly phase-modulates the incident wave in the form:

$$e^{j\phi_2(X_1)} \approx 1 + j\phi_2 \cos \frac{2\pi X_1}{L_2} \tag{2-51}$$

Then immediately below this infinitely thin screen, the complex field is:

$$E_2(X_1, Z_1) = \sqrt{\overline{F}}\; e^{j2\pi \frac{\left(Z_1 + Z'\right)}{\lambda}}\; e^{\frac{j\pi X_1^2}{\lambda\left(Z_1 + Z^1\right)}}$$

$$\left\{\left[1. + \phi_1 \sin \frac{\pi\lambda\overline{F}_1 Z_1}{L_1^2} \cos \frac{2\pi\overline{F}_1 X_1}{L_1} - \phi_1\phi_2 \cos \frac{\pi\lambda\overline{F}_1 Z_1}{L_1^2}\right.\right.$$

$$\left.\cos \frac{2\pi X_1}{L_2} \cdot \cos \frac{2\pi\overline{F}_1 X_1}{L_1}\right] + j\left[\phi_1 \cos \frac{\pi\lambda\overline{F}_1 Z_1}{L_1^2}\right. \qquad (2\text{-}52)$$

$$\cos \frac{2\pi\overline{F}_1 X_0}{L_1} + \phi_2 \cos \frac{2\pi X_1}{L_2} + \phi_1\phi_2 \sin \frac{\pi\lambda\overline{F}_1 Z_1}{L_1^2}$$

$$\left.\left.\cos \frac{2\pi X_1}{L_2} \cos \frac{2\pi\overline{F}_1 X_1}{L_1}\right]\right\}$$

Each layer is considered weak such that $\phi_i \leq 0.2$ ; the spatial frequencies associated with $\phi_i, \phi_j$ products will then have coefficients less than 0.02 and may be neglected.

The process is continued to include the five cosinusoidal phase-modulating screens; then the complex field at a distance, $Z_5$ , below the last screen contains the single scattering contributions of each of

the screens. The in-phase and quadrature components of the field as functions of $X_5$, $Z_5$ are:

In-Phase

$$1 + \phi_1 \sin \frac{\pi\lambda\bar{F}_1\beta_1}{L_1^2} \cos \frac{2\pi\bar{F}_1\bar{F}_2\bar{F}_3\bar{F}_4\bar{F}_5X_5}{L_1}$$

$$+ \phi_2 \sin \frac{\pi\lambda\bar{F}_2\beta_2}{L_2^2} \cos \frac{2\pi\bar{F}_2\bar{F}_3\bar{F}_4\bar{F}_5X_5}{L_2}$$

$$+ \phi_3 \sin \frac{\pi\lambda\bar{F}_3\beta_3}{L_3^2} \cos \frac{2\pi\bar{F}_3\bar{F}_4\bar{F}_5X_5}{L_3} \qquad (2\text{-}53)$$

$$+ \phi_4 \sin \frac{\pi\lambda\bar{F}_4\beta_4}{L_4^2} \cos \frac{2\pi\bar{F}_4\bar{F}_5X_5}{L_4}$$

$$+ \phi_5 \sin \frac{\pi\lambda\bar{F}_5Z_5}{L_5^2} \cos \frac{2\pi\bar{F}_5X_5}{L_5}$$

Quadrature

$$\phi_1 \cos \frac{\pi\lambda\bar{F}_1\beta_1}{L_1^2} \cos \frac{2\pi\bar{F}_1\bar{F}_2\bar{F}_3\bar{F}_4\bar{F}_5X_5}{L_1}$$

$$+ \phi_2 \cos \frac{\pi\lambda\bar{F}_2\beta_2}{L_2^2} \cos \frac{2\pi\bar{F}_2\bar{F}_3\bar{F}_4\bar{F}_5X_5}{L_2}$$

$$+ \phi_3 \cos \frac{\pi\lambda\bar{F}_3\beta_3}{L_3^2} \cos \frac{2\pi\bar{F}_3\bar{F}_4\bar{F}_5X_5}{L_3} \qquad (2\text{-}54)$$

$$+ \phi_4 \cos \frac{\pi\lambda\bar{F}_4\beta_4}{L_4^2} \cos \frac{2\pi\bar{F}_4\bar{F}_5X_5}{L_4}$$

$$+ \phi_5 \cos \frac{\pi\lambda\bar{F}_5Z_5}{L_5^2} \cos \frac{2\pi\bar{F}_5X_5}{L_5}$$

where $\beta_1 = Z_1 + \bar{F}_1\bar{F}_2Z_2 + \bar{F}_1\bar{F}_2^{\,2}\bar{F}_3Z_3 + \bar{F}_1\bar{F}_2^{\,2}F_3^{\,2}F_4Z_4 + \bar{F}_1\bar{F}_2^{\,2}\bar{F}_3^{\,2}\bar{F}_4^{\,2}\bar{F}_5Z_5$

$$\beta_2 = Z_2 + \bar{F}_2\bar{F}_3Z_3 + \bar{F}_2\bar{F}_3^{\,2}\bar{F}_4Z_4 + \bar{F}_2\bar{F}_3^{\,2}\bar{F}_4^{\,2}\bar{F}_5Z_5$$

$$\beta_3 = Z_3 + \bar{F}_3\bar{F}_4Z_4 + \bar{F}_3\bar{F}_4^{\,2}\bar{F}_5Z_5$$

$$\beta_4 = Z_4 + \bar{F}_4\bar{F}_5Z_5$$

$$\bar{F}_1 = \frac{Z'}{Z' + Z_1}$$

$$\bar{F}_2 = \frac{Z' + Z_1}{Z' + Z_1 + Z_2}$$

$$\bar{F}_3 = \frac{Z' + Z_1 + Z_2}{Z' + Z_1 + Z_2 + Z_3}$$

$$\bar{F}_4 = \frac{Z' + Z_1 + Z_2 + Z_3}{Z' + Z_1 + Z_2 + Z_3 + Z_4}$$

$$\bar{F}_5 = \frac{Z' + Z_1 + Z_2 + Z_3 + Z_4}{Z' + Z_1 + Z_2 + Z_3 + Z_4 + Z_5}$$

A computer program was used to calculate the diffraction patterns which developed behind this five-level screen. Twenty independent parameters were used to define the screen:

$\phi_i$ , $i = 1, \ldots 5.$

$Z_i$ , $i = 1, \ldots 5.$

$L_i$ , $i = 1, \ldots 5.$

$\alpha_i$ , $i = 1, \ldots 5.$

where $\alpha_i$ is the phasing of the cosinusoidal modulation at $X = 0$. The in-phase and quadrature terms were first obtained; there were then used to compute the phase and amplitude patterns. A number of patterns were computed to determine effects of varying independent parameters. Selected results are shown in Figures 16 and 17, where total thicknesses of 10 and 100 km have been used. The patterns of both these screens show effects of the multiple frequencies which are present. The only difference is that the focusing or interference patterns of the thin screens are sharper. A change in screen thickness has little effect on the patterns produced. This is particularly true when the screen is near the midpoint between the radiating source and the receiver where the pattern is observed.

## 2.7 Relationships Between Diffraction Patterns and the Phase-Modulating Screen that Produces Them

As the diffraction patterns measured behind an ionospheric screen vary with the distance from the screen, the situation where a satellite is tracked through an ionosphere of constant height causes the patterns to be a function of zenith angle. This dependence on zenith angle results because the parameter $\overline{FZ}$ is doubled when the zenith angle changes from overhead to 60 degrees. At the screen itself, the variation of phase modulation across the screen requires a corresponding variation in the electron density. The diffraction pattern which the screen produces on the surface of the Earth has scatters which originate from a finite region

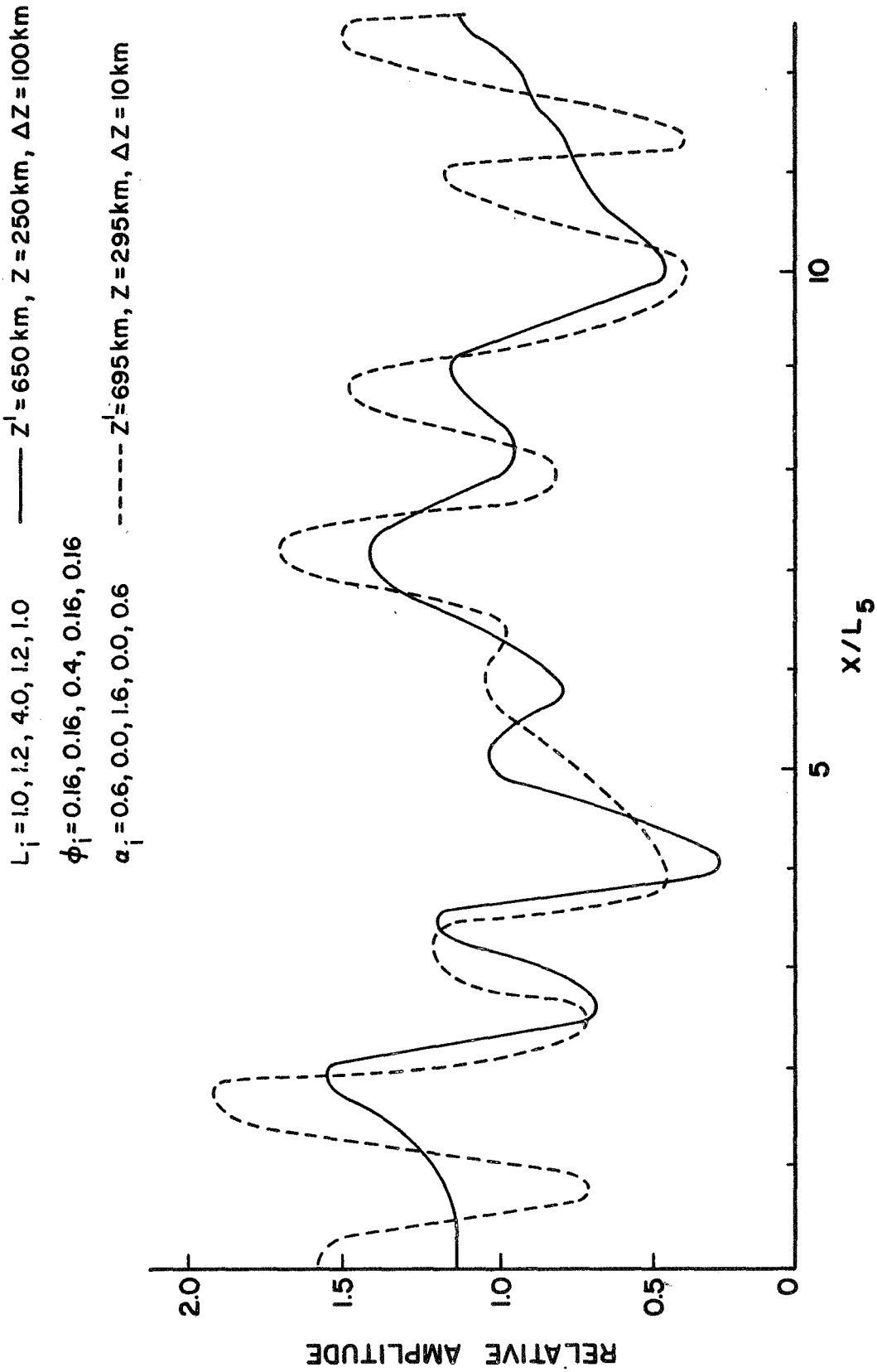


Figure 16. Amplitude Diffraction Patterns Produced by a Thick Screen With Scale Size Tapered from Center

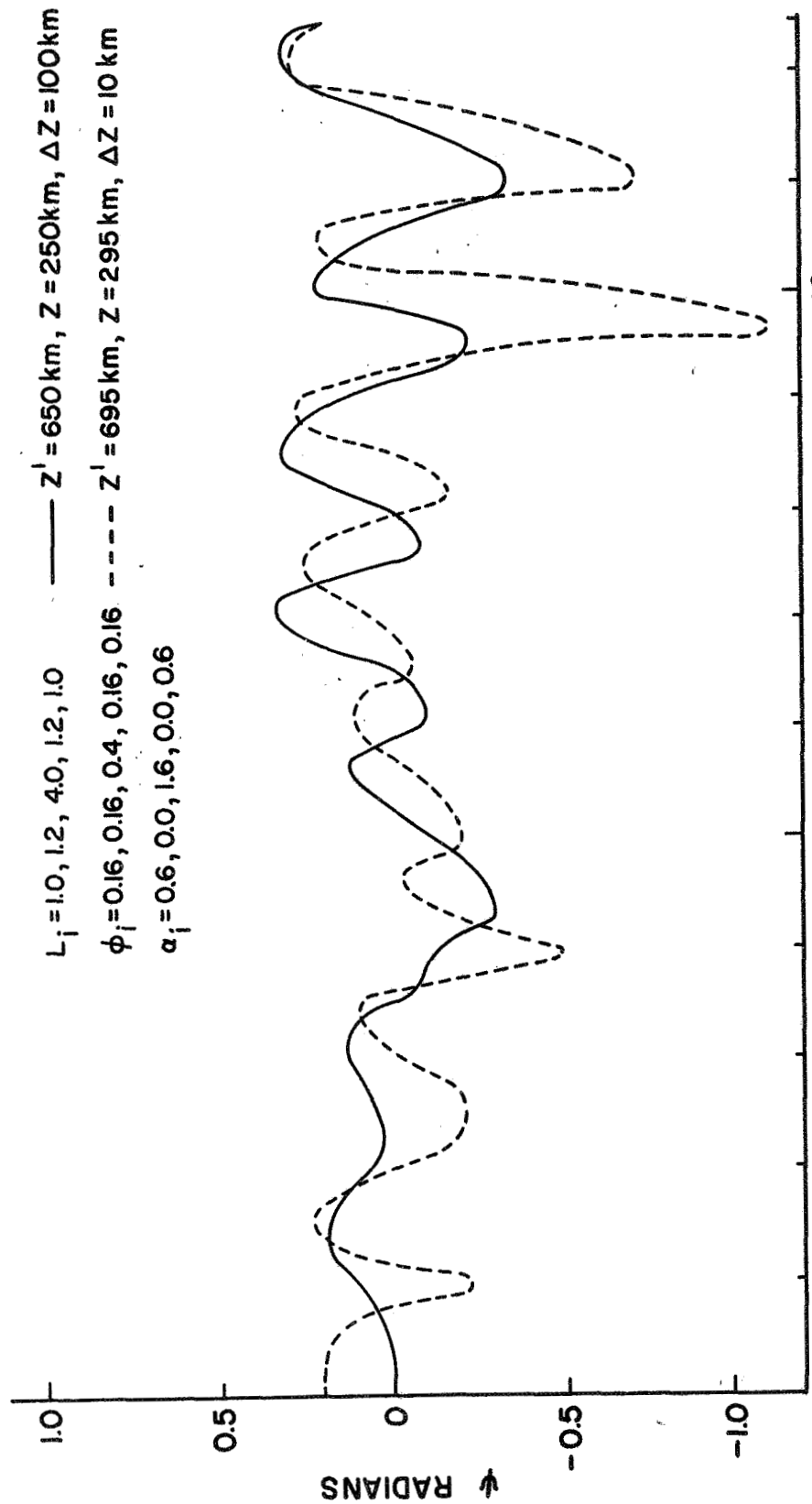


Figure 17. Phase Diffraction Patterns Produced by a Thick Screen with Scale Size Tapered from Center

of the screen when only weak scattering is considered. The two-dimensional screens investiaged in this study have peak modulations of one radian or less. The relationships between the patterns and screen area, distance, and electron content variations are presented in this section.

### 2.7.1 The region of the Screen that can Contribute to the Pattern at One Point on the Earth's Surface

The radiation which is incident on the screen from above has scattered components for the Nth harmonic which makes angles of $n\lambda/L$ with the wave normal[3]. When the satellite source is at a finite distance, $Z'$, above the screen, the scattering angle at the screen is $n\lambda/L$, and the diffraction pattern is measured at a distance, $Z$, behind the screen; then the scattered components arrive at the observation point making an angle, $n\bar{F}\lambda/L$, with normal of the undiffracted component.

Because the scattering angles are small for weak scattering, the distance along the screen measured from the wave normal to the point where the scattered component originates in the screen $\Delta S$, is given by:

$$\Delta S \approx \bar{F}Z\ \lambda/L \qquad (2\text{-}55)$$

For the nominal satellite height of 1000 km and the ionospheric region of interest starting a $Z = 250$ Km , $\overline{FZ}$ varies from 187 km to 250 km when the satellite is overhead. When the zenith angle is increased to 50 degrees, then $\overline{FZ}$ varies from 280 km to 350 km for the same ionospheric heights (Figure 18). Some values of $\Delta S$ have been calculated for the 20 MHz single using $n = 1$ and $\overline{FZ}$ and $L$ as parameters. These are listed in Talbe 1. The linear dependence of these values on $n$ and $\lambda$ makes them larger for $n = 2$ but less for the 40 MHz signal.

It is shown in Section 2.4, for the two-dimensional screens considered in this investigation, that the values of $n$ of 1 and 2 are adequate. For a weak screen, only $n = 1$ is used. It is evident that, when the satellite is overhead, only those screens with scale sizes less than two km will have scatterers originating at points more than a scale size away from the undiffracted component. If the zenith angle is increased to 50 degrees, scale sizes of three km or less will have scattering contributors at more than a scale size away from the undiffracted component. Thus it is seen, for the weak screen, that the region of the screen occupied by a few anomalies contributes to the pattern. The ray optics theory may be applied here to determine the contributing screen area as the scale sizes involved are very large compared with the wavelength.

When modulation of up to one radian is considered, the region of the screen which contributes to the pattern increased four-fold. However, the region contributing to the 40 MHz signal pattern is only one

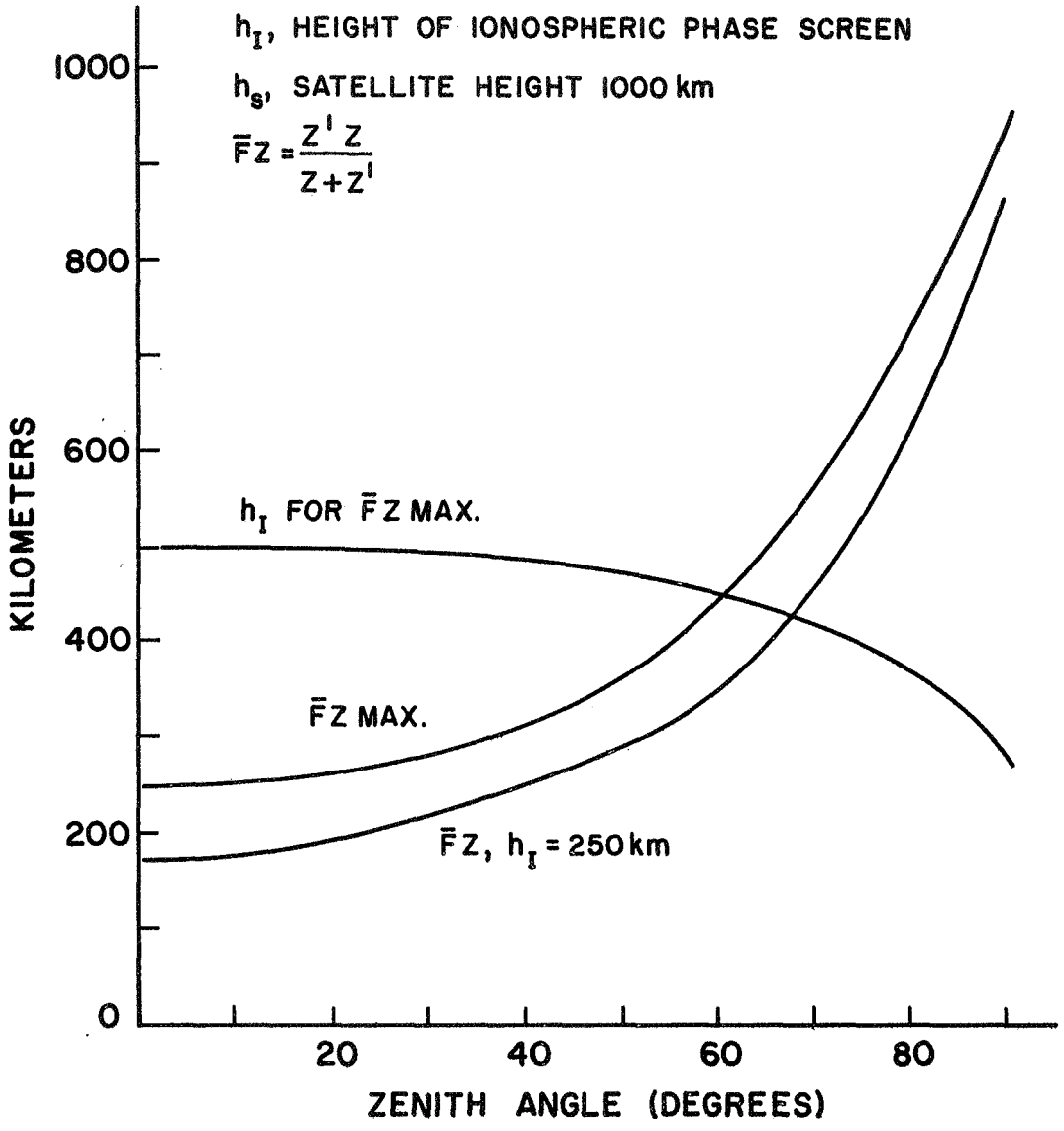


Figure 18. $\bar{F}Z$ and $h_I$ for $\bar{F}Z$ Max Versus Zenith Angle

Table 1 Distance Along The Ionospheric Screen From the Undiffracted Component to the Scattered Component: $\lambda$ = 0.015 km  n = 1

| $\overline{FZ}$ = | 180 km | 250 km | 300 km | 350 km |
|---|---|---|---|---|
| L = 1. km | 2.70 km | 3.75 km | 4.50 km | 5.25 km |
| L = 2. km | 1.35 km | 1.875 km | 2.25 km | 2.63 km |
| L = 3. km | 0.90 km | 1.250 km | 1.50 km | 1.75 km |
| L = 4. km | 0.68 km | 0.938 km | 1.13 km | 1.31 km |
| L = 5. km | 0.54 km | 0.750 km | 0.90 km | 1.05 km |

quarter of the size of the region contributing to the 20 MHz signal pattern. This limited region of the screen, which can contribute to the pattern at a point in terms of the anomaly size, becomes a strip for the length of record sampled. With the short records used for analysis, only a few dominant scale sizes exist. The small number of anomalies which contribute to the pattern over the record length is used for justification of the modeling.

An increase in the zenith angle of the satellite's position not only increases the effective distance, FZ , but also produces a tilt of a spherically stratified screen away from its normal position which it makes with the radiation at overhead. The tilt angle is given as a function of zenith angle, with ionospheric height a parameter in Figure 19. If a zenith angle of 50 degrees is selected, then for $n = 2$ and $L = 1$ (Table 1), the maximum value of $\Delta S$ is 10.5 km. This displacement increases to 15.7 km along the tilted screen and represents a change of $Z$ of 11.6 km. The effect of this change on the argument of the Fourier coefficients; $n^2 \frac{2\pi\lambda\overline{FZ}}{L^2}$ , can be found by using:

$$\overline{FZ} = \frac{(r_s - Z)}{r_s} Z \tag{2-56}$$

then:

$$d\left(n^2 \frac{2\pi\lambda\overline{FZ}}{L^2}\right) = \frac{n^2\, 2\pi\lambda}{L^2} \left(1 - \frac{2Z}{r_s}\right) \tag{2-57}$$

This represents a change of 26.8 degrees in this extreme case, when $\eta = 2$ , $L = 1$ , and zenith angle is 50 degrees. For the weak screen, the change in the function of $Z$ is only one-eighth as large. Thus, for this study the effects of tilts will be considered to be second order. The major effect produced when the screens are tilted is to alter the projection of the anomalies on the plane which is normal to the line of signal propagation. The scale size observed at the antenna is changed when tilting is present.

### 2.7.2 The Effect of Zenith Angle and Distance on Amplitudes of the Various Frequency Components of the Diffraction Patterns

The previous sections demonstrated that for the one-dimensional, weak phase screen each Fourier component in the amplitude pattern is multiplied by $\sin \pi\lambda\bar{F}\bar{Z}/L_i^2$ , while each Fourier component in the phase pattern is multiplied by $\cos \pi\lambda\bar{F}\bar{Z}/L_i^2$ , where $L_i$ is the scale size at the screen which produces the particular component. When the screen has a phase modulation which is a function of two dimensions, the term $\pi\lambda\bar{F}\bar{Z}/L_i^2$ is multiplied by a factor which lies between 1 and 2, depending on the relative scale size in the two dimensions. When these scale sizes are equivalent, the factor is 2 and the same frequencies are contained in the diffraction patterns regardless of the satellite motion over the screen. When one dimension is twice as large as the other, the factor is 1.25 and some of the frequencies can be lower due to the difference terms (2.32). Thus it is seen that the frequencies which appear

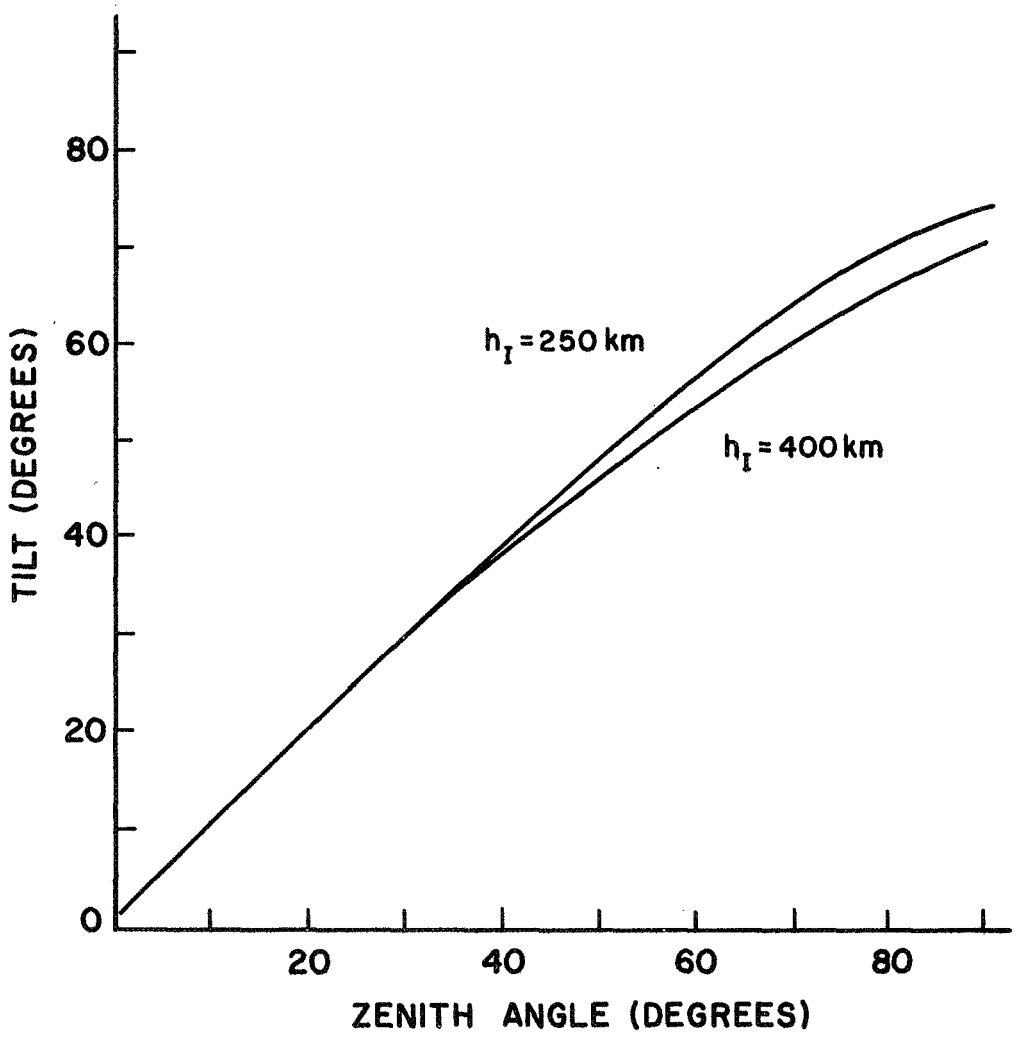


Figure 19. Ionospheric Tilt Versus Zenith Angle for Two Screen Heights

prominently in the diffraction patterns depend on the two-dimensional scale sizes, the distance to the screen, and direction in which the screen is crossed.

The variation in $\overline{FZ}$ as a function of zenith angle, for three values of ionospheric height and a satellite height of 1,000 km, has been calculated. This has been used in the expression $2\pi\lambda\overline{FZ}/L_i^2$ for $\lambda = 0.015$ km to determine the variation of $L_i$ versus zenith angle when $2\pi\lambda\overline{FZ}/L_i^2$ is a parameter. These are presented as the curves in Figures 20 through 25 where $\Theta = 2\pi\lambda\overline{FZ}/L_i^2$ is the parameter.

Values of $\Theta$ of $\pi/2$ and $3\pi/2$ would maximize the amplitude pattern, while values of $\Theta$ that are near 0 or $\pi$ would maximize the phase pattern. When a one-dimensional screen or the 40 MHz ($\lambda = 0.0475$ km) signal is considered, $\Theta$ is $\Theta/2$ . These curves are used to determine how each scale size can contribute to the amplitude or phase patterns observed on the Earth's surface.

When these patterns are recorded and analyzed by Fourier methods, certain frequency components have more energy than do others. The relationships between scale size and zenith angle with frequency as a parameter for the same satellite have been calculated and are presented in the b curves of Figures 20 through 25. These curves are used with the Fourier spectrums to determine the scale sizes of the phase modulating screens.

Figures 20 through 25 have two applications; one is to determine how a change in zenith angle will cause $\Theta$ to vary for a given scale size. The other is to determine what scale sizes are required to produce

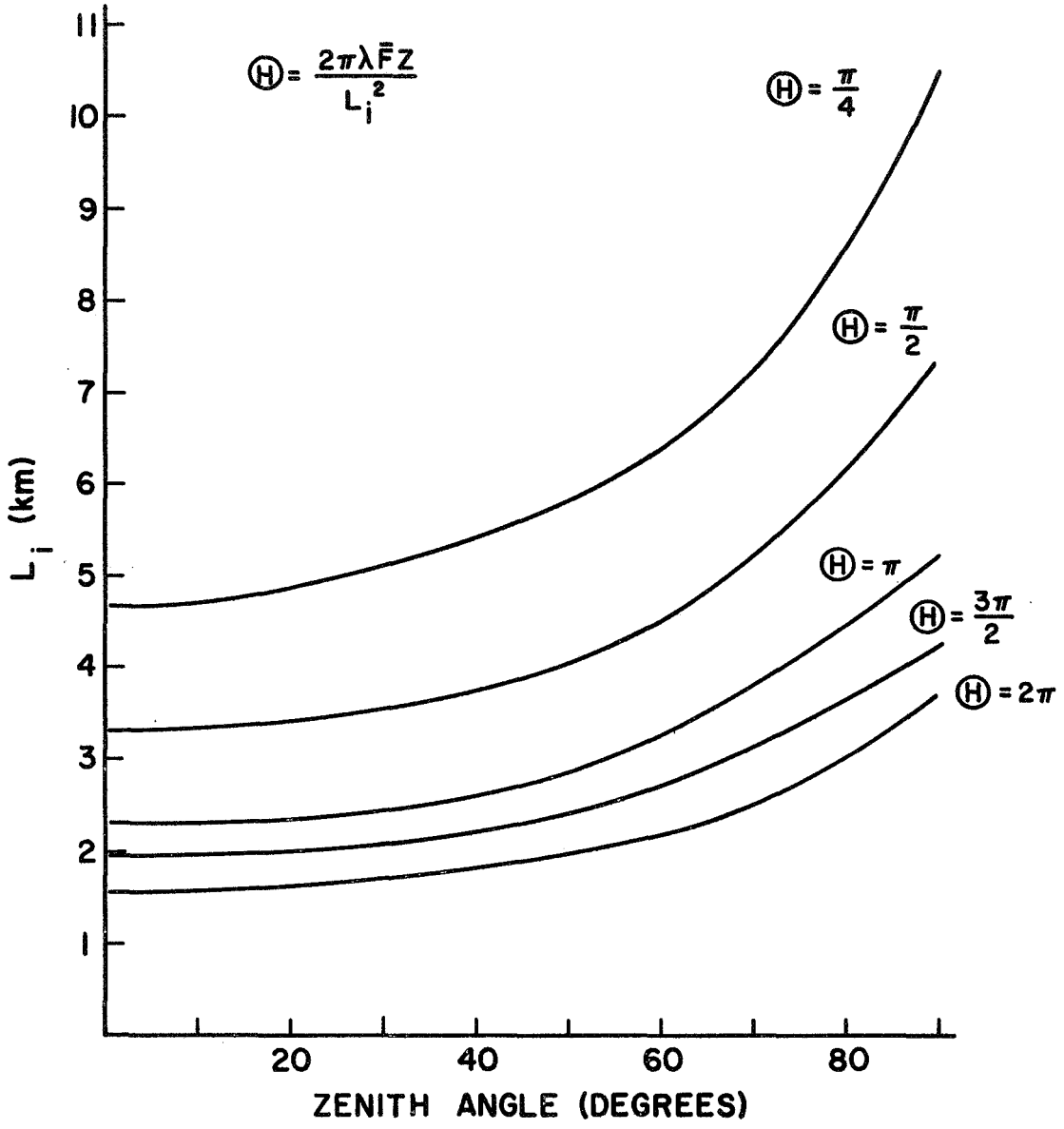


Figure 20. Scale Size Versus Zenith Angle with Θ a Parameter, $h_I$ = 250 km

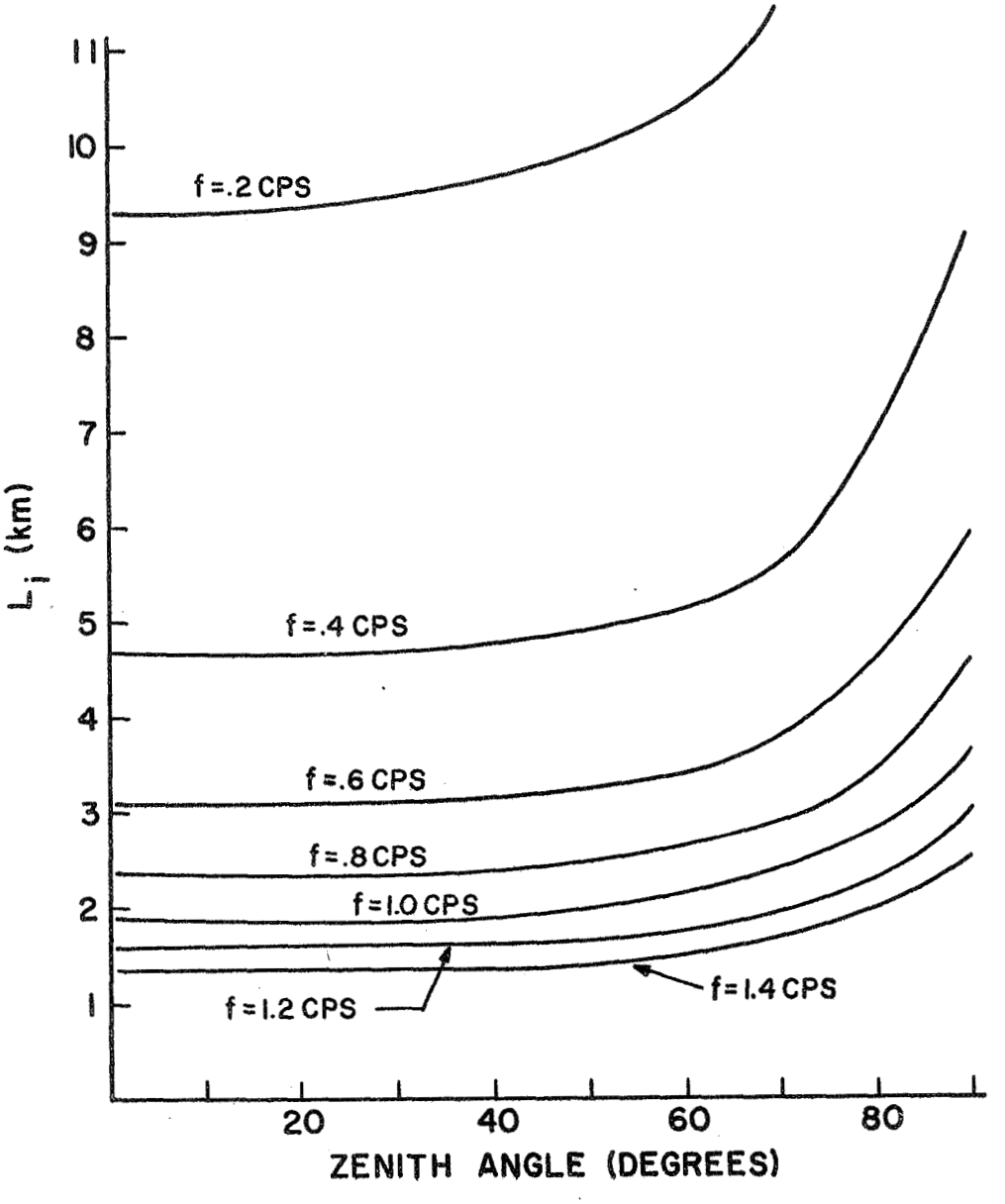


Figure 21. Scale Size Versus Zenith Angle with Frequency at Receiver a Parameter, $h_I$ = 250 km

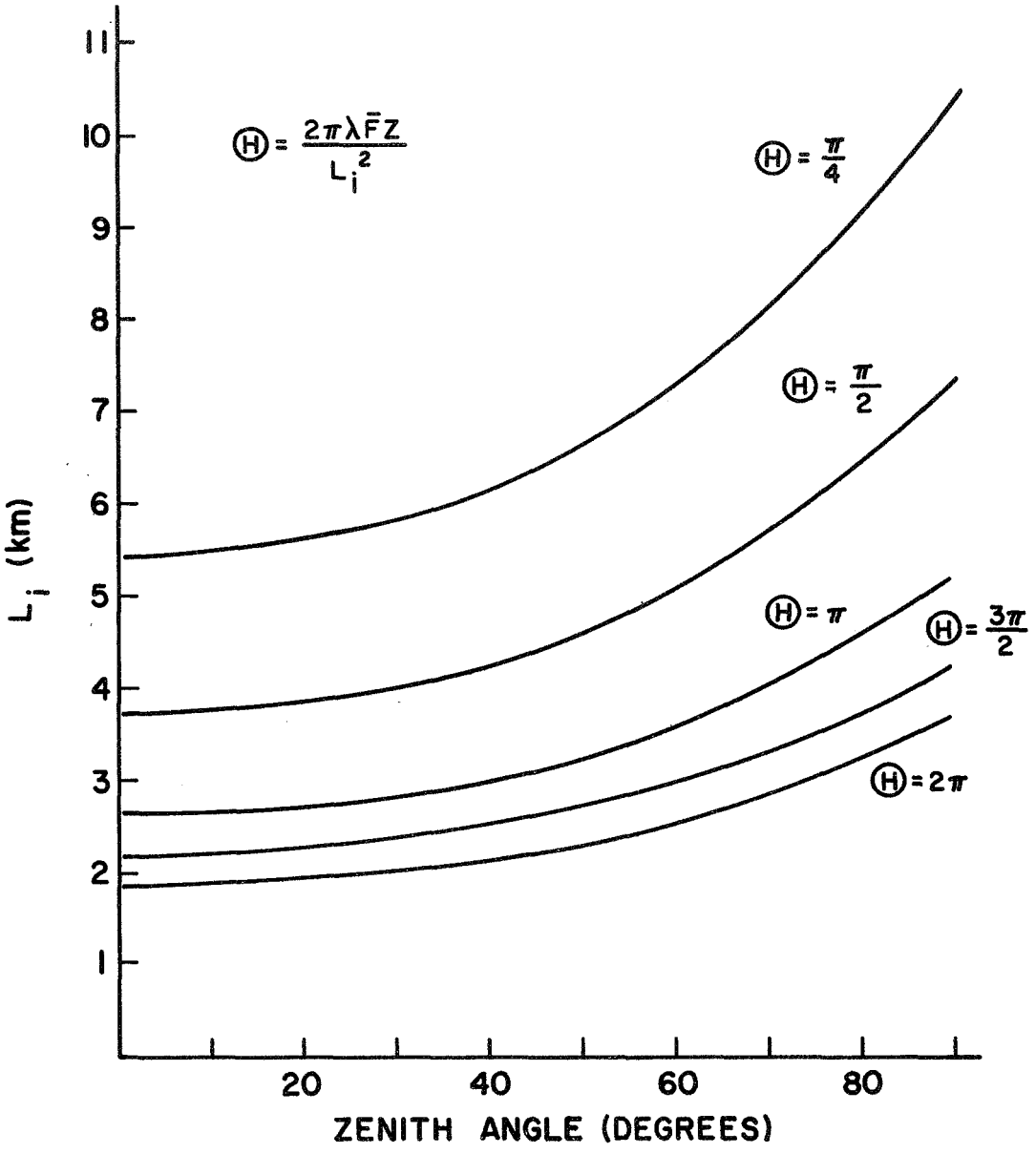


Figure 22. Scale Size Versus Zenith Angle with Θ a Parameter, $h_I$ = 400 km

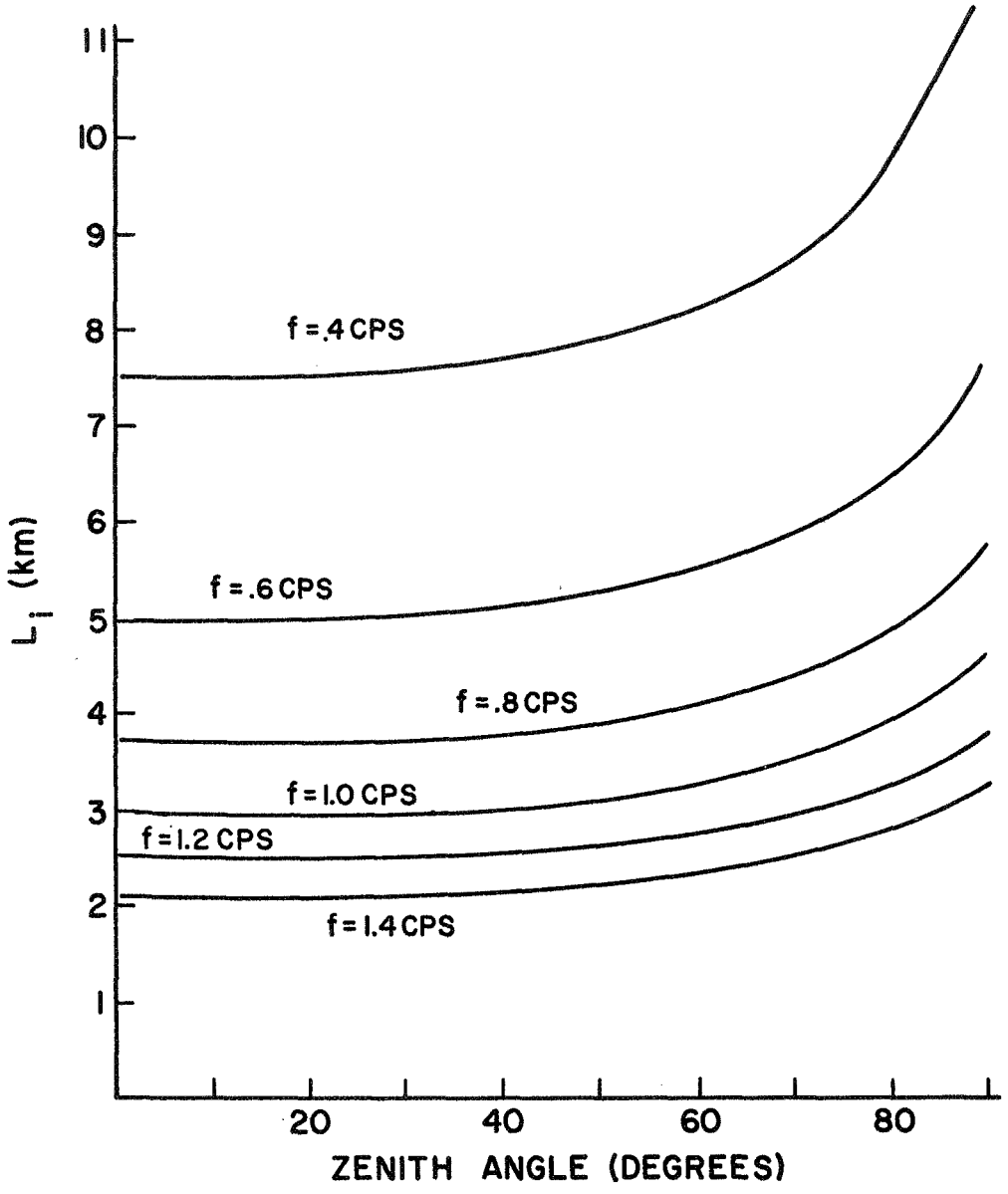


Figure 23. Scale Size Versus Zenith Angle with Frequency at Receiver a Parameter, $h_I$ = 400 km

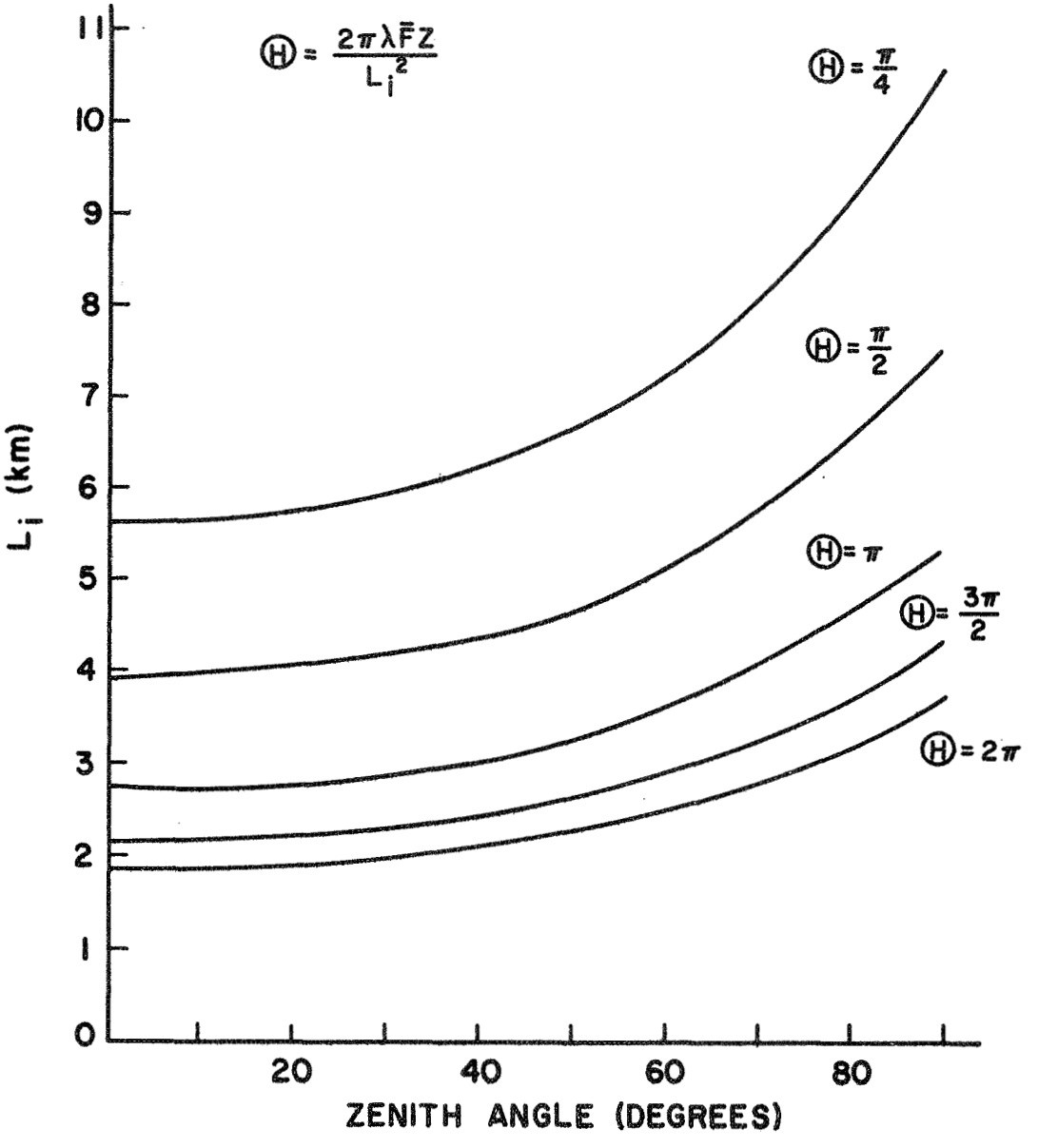


Figure 24. Scale Size Versus Zenith Angle with Θ a Parameter, $h = h_I$ for $\bar{F}Z$ (Max)

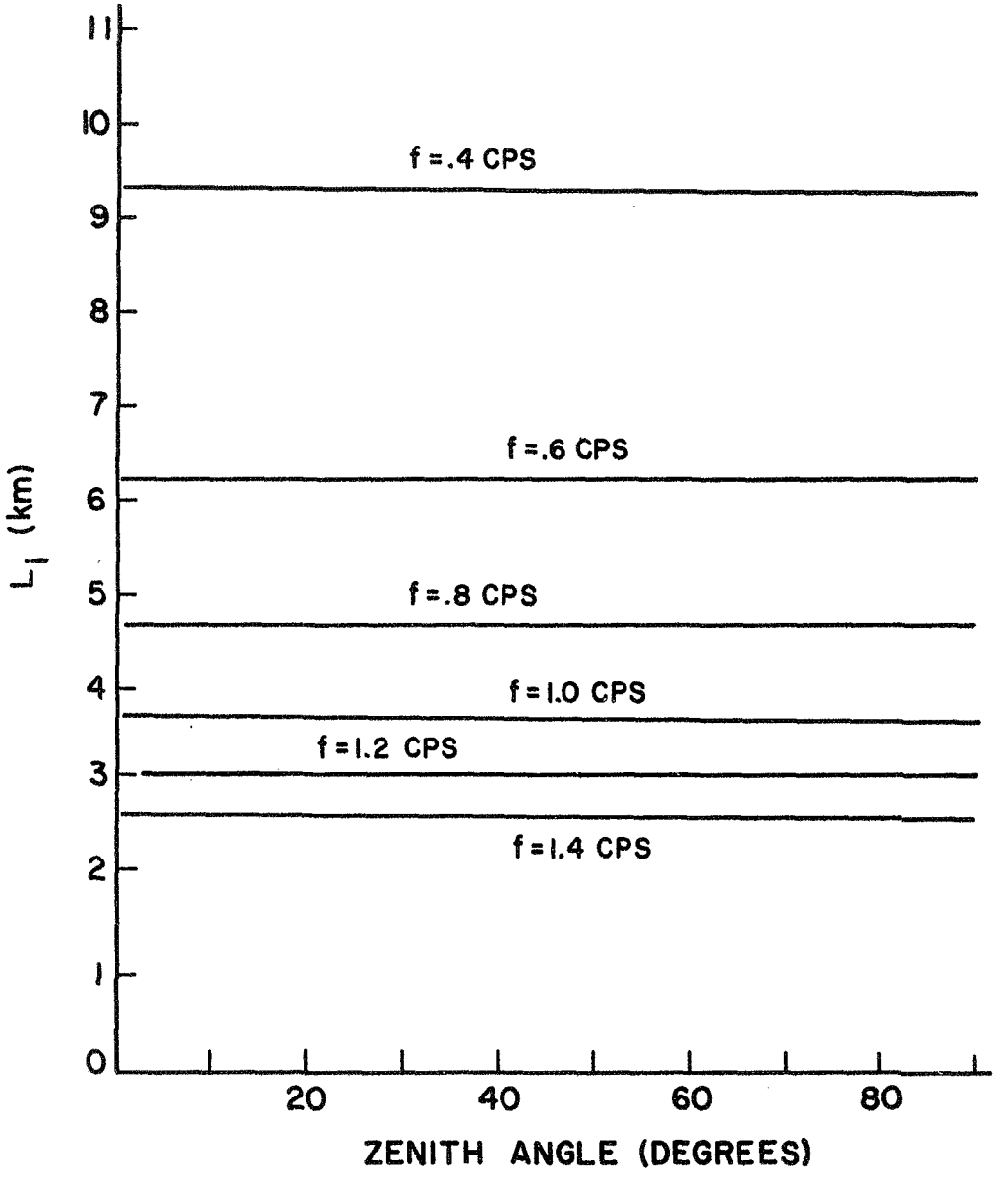


Figure 25. Scale Size Versus Zenith Angle with Frequency at Receiver a Parameter, $h = h_I$ for $\overline{FZ}$ (Max)

certain frequency components in the pattern. Then the dependence of the Fourier coefficients on the particular value of $\Theta$ is determined.

A large portion of the data analysis involves the comparison of the phase and amplitude patterns and their frequency spectrums. To help accomplish this comparision, the relative importance of the coefficients of each term have been calculated and plotted as a function of $\Theta$ . If the 20 MHz amplitude pattern has Fourier coefficients of the form:

$$A_{i(20)} = \varphi_i \sin \frac{2\pi\lambda_1 \overline{FZ}}{L_i^2} \tag{2-58}$$

when $\varphi_i$ = phase modulation imposed on the 20 MHz wave;

$\lambda_1$ = wavelength of the 20 MHz signal, 0.015 km;

$L_i$ = scale size of the ith term;

the 20 MHz phase patterns will have Fourier coefficients of the form:

$$\psi_{i(20)} = \varphi_i \cos \frac{2\pi\lambda_1 \overline{FZ}}{L_i^2} \tag{2-59}$$

and the Fourier components of the amplitude and phase patterns of the 40 MHz signal have the coefficients:

$$A_{i(40)} = \varphi_{i/2} \sin \frac{2\pi\lambda_2 \overline{FZ}}{L_i^2} \tag{2-60}$$

$$\psi_{i(40)} = \varphi_{i/2} \cos \frac{2\pi\lambda_2 \overline{FZ}}{L_i^2} \tag{2-61}$$

where $\lambda_2$ = the wavelength of the 40 MHz signal.

The phase measured at each end of the baseline system is that of the phase difference between the two frequencies. The components of the phase difference have the coefficients:

$$\psi_{i(20-40)} = \varphi_i \left( \cos \frac{2\pi\lambda_1 \overline{FZ}}{L_i^2} - \frac{1}{2} \cos \frac{2\pi\lambda_2 \overline{FZ}}{L_i^2} \right) \tag{2-62}$$

The three patterns used in most of the comparisons are the two amplitude patterns and the phase difference patterns. These patterns are plotted as a function of $\Theta$ for the $\lambda$ of 20 MHz and with $\varphi_i$ normalized to 1 in Figure 26.

Examination of these curves reveals intervals that yield larger coefficients for the 40 MHz pattern than for the 20 MHz pattern. Also, when $\Theta$ lies between $\pi$ and $2\pi$, the coefficients of the two amplitude patterns are of opposite sign, which shifts the nulls of one pattern with respect to the other. The phase difference pattern is seen to have coefficients which are from zero to 1.5 times larger than $\varphi_i$. The nulls in the Fourier spectrum of the 20 MHz amplitude pattern will occur in conjunction with a maximum in the phase difference pattern.

The other diffraction pattern considered is obtained from the phase difference across the baseline. In the simplest case, the satellite motion is parallel to the baseline and the screen has a one-dimensional

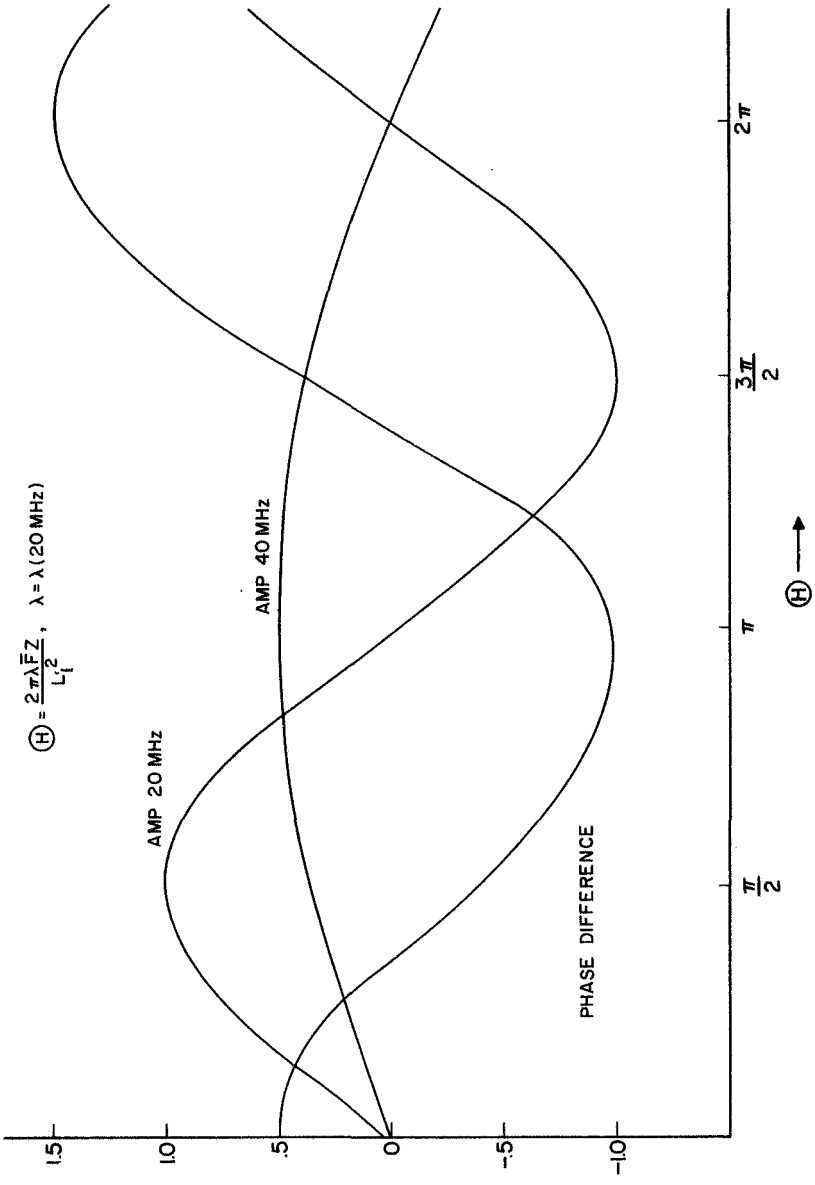


Figure 26. Relative Values of Diffraction Patterns Fourier Coefficients as a Function of Θ

variation in the same direction. Then the interferometer phase pattern for the 20 MHz signal will have Fourier components of the form:

$$\psi_{i(20-20b)} = \varphi_i \cos \frac{2\pi\lambda_1 \bar{F} Z}{L_i^2} \left[\cos \frac{2\pi \bar{F} X}{L_i} - \cos \frac{2\pi \bar{F}}{L_i} (X-q)\right]$$

$$= 2\varphi_i \cos \frac{2\pi\lambda_1 \bar{F} Z}{L_i^2} \sin \frac{\pi \bar{F}^2 b}{L_i} \cos\left(\frac{2\pi \bar{F} X}{L_i} - \eta\right) \qquad (2\text{-}63)$$

where $\tan \eta = \left(\dfrac{-\sin \frac{2\pi \bar{F}^2 b}{L_i}}{1 - \cos \frac{2\pi \bar{F}^2 b}{L_i}}\right)$

$q$ = the separation at the screen, $q \approx \bar{F}b$.

Thus it is seen that the baseline interferometer acts as a spatial filter on the Fourier components. The scale size whose diffraction component lies at the center of the pass band, $L_{i(M)}$, is a function of $b$ and $\bar{F}^2$:

$$L_{i(M)} = 2 \bar{F}^2 b$$

The scale size is within the filter half-power points when:

$$1.33 \bar{F}^2 b \leq L_i \leq 4. \bar{F}^2 b$$

When the baseline is parallel to the scale dimension of the one-dimensional screen but not to the satellite motions, then the rays to the two ends of the baseline follow parallel tracks through the ionospheric screen which are separated by distance, $\Delta P$:

$$\Delta P = \bar{F} b \sin \alpha \qquad (2\text{-}64)$$

where $\alpha$ is the angle between the baseline and the satellite motion.

The separation of the rays measured in the direction of motion is $\Delta D$ :

$$\Delta D = \bar{F} b \cos \alpha \tag{2-65}$$

which has the effect of increasing the apparent scale size. The baseline length, $b$ , must be longer by sec $\alpha$ to maximize a particular Fourier component when the satellite motion is not parallel to the baseline. The two requirements for maximizing a particular Fourier component are then:

$$\begin{aligned} L_i &= 2\bar{F}^2 b \cos \alpha \\ L_i &= 2\sqrt{\lambda \bar{F} Z} \end{aligned} \tag{2-66}$$

The frequencies most often observed in the diffraction patterns measured indicate that $L_i$ is from 2 to 5 km. As the value of $\bar{F}$ lies between 0.5 and 0.75, a baseline having a length of 5.0 km would place the pass band in the center of the expected frequencies. The 1 km baseline used in this study put the diffraction components of all scale sizes greater than 2.2 km outside of the half-power point. The scale size which is so attenuated is reduced to 1.0 km when the screen lies half-way between the satellite and receiver.

The effects of a particular baseline length can be extended to include the more general case where the screen is two-dimensional and the directions of the satellite ground track, the baseline, and the $X_0$ axis in the screen are arbitrary. If $\beta$ is the angle between the direction

of the $X_0$ axis and the baseline, and $\alpha$ is the angle between the baseline direction and the satellite ground track, the motion across the screen is such that:

$$\begin{aligned} Y_0 &= aX_0 \\ a &= \text{Tan}\ (\alpha + \beta) \end{aligned} \tag{2-67}$$

If a ray through $(X_0, Y_0)$ goes to one end of the baseline, the ray to the second end has a parallel direction of travel:

$$\begin{aligned} Y_0' &= aX_0' + P \\ X_0' &= X_0 - \overline{F}b \cos \beta \\ P &= \overline{F}b\ (a \cos \beta - \sin \beta) \end{aligned} \tag{2-68}$$

The individual sum and difference frequencies for the phase pattern of a two-dimensional screen are given by 2-31. If the relationships of 2-67 and 2-68 are used in 2-31, and a phase difference across a baseline similar to 2-63 is desired, expression is:

$$\psi_i(20\text{-}20b) = \frac{\varphi_i}{2} \cos \frac{\pi \lambda_1 \overline{F} Z}{L_1^2} \left(1 + \frac{L_1^2}{L_2^2}\right) \left\{ \cos \frac{2\pi \overline{F}}{L_1} \left[1 \pm \frac{L_1}{L_2} a\right] X \right. \tag{2-69}$$

$$\left. - \cos \frac{2\pi \overline{F}}{L_1} \left[ \left(1 \pm \frac{L_1}{L_2} a\right) X - \overline{F}b \left(\cos \beta \pm \frac{L_1}{L_2} \sin \beta\right) \right] \right\}$$

This can be expressed by:

$$\psi_i(20\text{-}20b) = \varphi_i \cos \frac{\pi\lambda\bar{F}Z}{L_1^2} \left(1 + \frac{L_1^2}{L_2^2}\right) \sin \frac{\pi\bar{F}^2 b}{L_1} \left(\cos \beta \pm \frac{L_1}{L_2} \sin \beta\right) \cos\left[\frac{2\pi\bar{F}}{L_1}\left(1 \pm \frac{L_1}{L_2}\, a\right) X - \gamma\right] \tag{2-70}$$

where $\gamma = \mathrm{Tan}^{-1}\left\{\dfrac{-\sin \frac{2\pi\bar{F}^2 b}{L_1}\left(\cos \beta \pm \frac{L_1}{L_2} \sin \beta\right)}{1 - \cos \frac{2\pi\bar{F}^2 b}{L_1}\left(\cos \beta \pm \frac{L_1}{L_2} \sin \beta\right)}\right\}$

when $a = 0$ , $\beta = 0$ , $L_1 = L_2 = L_1$ , 2-70 and 2-63 are identical.

The filter effect of the baseline is then represented by a product of a function of $Z$ and a function of $b$ , each of which has its nulls. When $b/L_i$ is small, the diffraction component which has the scale size will be attenuated for all $Z$ .

The phase difference patterns between the two frequencies as expressed by 2-62 use signals which also have a separation of their paths from the satellite to the antennas located at one end of the baseline. When these 20 and 40 MHz signals pass through the ionosphere having a zenith angle which is not zero, their ray paths are bent by different amounts. The 20 MHz signal is bent the most; it enters the top of the ionosphere with a smaller zenith angle than that of the 40 MHz signal. The two rays will cross at a point slightly above the height of peak ionospheric density and have a maximum separation at heights of 200 and

500 km. Calculations made using a parabolic profile indicate this maximum separation for nighttime conditions to be about 1.0 km for a zenith angle of 30 degrees and 2.5 km for a zenith angle of 45 degrees. A separation between the ordinary and extraordinary components of each frequency also exists and has been discussed by Roger,(1965)[13]. The spatial frequencies obtained from the records of diffraction patterns and the time correlation of the amplitude patterns of the two frequencies indicate that any separation at screen heights is small.

The separation of these rays in the ionosphere is a function of the frequencies, the zenith angle, and the ionospheric profile. There is no dependence on $\overline{F}$ as is true for the baseline system. Let the ray path projection on the screen make an angle, $\alpha$ ,with the direction of the satellite track across the screen and let this track make an angle, $\beta$ , with the $X_0$ axis. Then if the separation of the two rays measured along the screen is $r$ , this separation has components in the screen coordinate system given by:

$$X_0' - X_0 = r \cos(\alpha + \beta)$$
$$Y_0' - Y_0 = r \sin(\alpha + \beta) \qquad (2\text{-}71)$$

When the satellite motion across the screen is given by:

$$Y_0 = aX_0$$
$$a = \text{Tan } \beta \qquad (2\text{-}72)$$

Then the relationship between the two points in the screen can be expressed as:

$$X_0' = X_0 + r \cos(\alpha + \beta)$$
$$Y_0' = aX_0 + r \sin(\alpha + \beta) \tag{2-73}$$

The Fourier coefficients for this difference pattern, when the screen was one-dimensional and there was no differential refraction, were given by 2-62. When the screen is two-dimensional and the diffraction separation and satellite motion is given by 2-72 and 2-73, these coefficients are:

$$\psi_i(20\text{-}40) = \frac{\varphi_i}{2} \cos \frac{\pi\lambda_1 \bar{F} Z}{L_1^2} \left(1 + \frac{L_1^2}{L_2^2}\right) \cos \frac{2\pi\bar{F}}{L_1} \left(1 \pm \frac{L_1}{L_2} a\right) X$$
$$- \frac{\varphi_i}{4} \cos \frac{\pi\lambda_2 \bar{F} Z}{L_1^2} \left(1 + \frac{L_1^2}{L_2^2}\right) \cos \frac{2\pi\bar{F}}{L_1} \left[\left(1 \pm \frac{L_1}{L_2} a\right) X + rV\right] \tag{2-74}$$

where $V = \left[\cos(\alpha + \beta) + \frac{L_1}{L_2} \sin(\alpha + \beta)\right]$

This can be expressed by:

$$\psi_i(20\text{-}40) = K \cos \left[\frac{2\pi\bar{F}}{L_1} \left(1 \pm a \frac{L_1}{L_2}\right) X - \gamma\right] \tag{2-75}$$

$$\text{where} \quad K = \frac{\varphi_i}{2} \left\{ \cos^2 \frac{\pi\lambda_1 \bar{F}Z}{L_1^2} \left(1 + \frac{L_1^2}{L_2^2}\right) + \frac{1}{4} \cos^2 \frac{\pi\lambda_2 \bar{F}Z}{L_1^2} \left(1 + \frac{L_1^2}{L_2^2}\right) \right.$$

$$\left. - \cos \frac{\pi\lambda_1 \bar{F}Z}{L_1^2} \left(1 + \frac{L_1^2}{L_2^2}\right) \cos \frac{\pi\lambda_2 \bar{F}Z}{L_1^2} \left(1 + \frac{L_1^2}{L_2^2}\right) \cos \frac{2\pi \bar{F}rV}{L_1} \right\}$$

$$\gamma = \tan^{-1} \left\{ \frac{\sin \frac{2\pi \bar{F}rV}{L_1}}{2 - \cos \frac{2\pi \bar{F}rV}{L_1}} \right\}$$

When r is 0 , the magnitude of $\psi_i(20\text{-}40)$ has a dependence on Z and the scale sizes as shown in Figure 26. When r is not zero, the same limits exist for $\psi_i(20\text{-}40)$ , but they will occur for different values of Z . Thus if: $\frac{2\pi \bar{F}rV}{L_1} = \pi/2$ , the phase difference curve is shifted to the left by $\Theta = \pi$ and inverted so the value is + 1 when $Z = 0$ . When $\frac{2\pi \bar{F}rV}{L_1} = \pi$ , the curve is shifted to the left by $\pi$ . Thus, when ray separation occurs, the particular value of $\bar{F}Z$ which suppresses a Fourier component originating from a scale size, $L_i$ , is shifted to another value. The presence of ray separation does not eliminate more spatial frequencies; in fact for; $\frac{2\pi \bar{F}rV}{L_1} = \pi/3$ , regions exist where all three of the patterns represented by Figure 26 can have significant Fourier coefficients for the same $\Theta$ .

In the development above, the form of the individual Fourier components has been determined for the different patterns that were measured. These were functions of the modulation at the screen, the scale size, the

distance and the wavelength. Next, the relationship between the power of the phase and amplitude patterns will be determined. Let the amplitude pattern of the 20 MHz signal consist of a number of weak Fourier components so it can be written as:

$$A = 1 + \varphi_0 \sum_{n=1}^{N} C_n \sin \frac{n^2 2\pi\lambda_1 \overline{FZ}}{L^2} \cos \frac{2\pi n \overline{FX}}{L} \tag{2-76}$$

then:

$$\frac{\Delta\bar{A}^2}{\bar{A}^2} = \frac{\varphi_0^2}{2} \sum_{n=1}^{N} C_n^2 \sin^2 \frac{n^2 2\pi\lambda_1 \overline{FZ}}{L_2} \tag{2-77}$$

And the phase pattern for the same screen has the variance:

$$\psi^2 = \frac{\varphi_0^2}{2} \sum_{n=1}^{N} C_n^2 \cos^2 \frac{n^2 2\pi\lambda_1 \overline{FZ}}{L^2} \tag{2-78}$$

However, the phase patterns measured are phase difference patterns, either between the two frequencies at one point or between the two ends of the baseline. The variance of the pattern across the basline is:

$$\psi_I^2 = 2\phi_0^2 \sum_{n=1}^{N} C_n^2 \cos^2 \left( \frac{n^2 2\pi\lambda_1 \overline{FZ}}{L^2} \right) \sin^2 \frac{n\pi \overline{Fb}}{L} \tag{2-79}$$

When the phase difference between the two frequencies is taken, and $\varphi_0$ represents the phase modulation of the 20 MHz signal, the variance of this diffraction pattern is:

$$\psi^2_{(20-40)} = \varphi^2_{0/2}\left\{\sum_{n=1}^{N} C_n^2 \cos^2\left(\frac{n^2 2\pi\lambda_1 \bar{F}Z}{L^2}\right) + \sum_{n=1}^{N} C_n^2/4 \cos^2\left(\frac{n^2 2\pi\lambda_2 \bar{F}Z}{L^2}\right) - \sum_{n=1}^{N} C_n^2 \left(\frac{n^2 2\pi\lambda_1 \bar{F}Z}{L^2}\right) \cos\left(\frac{n^2 2\pi\lambda_2 \bar{F}Z}{L^2}\right)\right\} \quad (2\text{-}80)$$

The quantities on the left of expressions 2-78, 2-79, and 2-80 have been calculated from the measured data and are part of the output of the Fourier analysis computer programs. The relationships existing between the amplitude scintillation and the phase scintillations of the two difference patterns are given by the following functions:

$$\frac{\Delta A^2}{\bar{A}^2} = \bar{\psi}^2_{I/4} \frac{\sum_{n=1}^{N} C_n^2 \sin^2\left(\frac{n^2 2\pi\lambda_1 \bar{F}Z}{L^2}\right)}{\sum_{n=1}^{N} C_n^2 \cos^2\left(\frac{n^2 2\pi\lambda_1 FZ}{L^2}\right) \sin^2 \frac{n\pi\bar{F}b}{L}} \quad (2\text{-}81)$$

and

$$\frac{\Delta A^2}{A^2} = \psi^2 \frac{\sum_{n=1}^{N} C_n^2 \sin^2\left(\frac{n^2 2\pi\lambda_1 \overline{FZ}}{L^2}\right)}{\left\{\sum_{n=1}^{N} C_n^2 \cos^2\left(\frac{n^2 2\rho\lambda_1 \overline{FZ}}{L^2}\right) + \sum_{n=1}^{N} C_n^2 \cos^2\left(\frac{n^2 2\pi\lambda_2 \overline{FZ}}{L^2}\right)\right.}$$

$$\left. - \sum_{n=1}^{N} C_n^2 \cos\left(\frac{n^2 2\rho\lambda_1 \overline{FZ}}{L^2}\right) \cos\left(\frac{n^2 2\pi\lambda_2 \overline{FZ}}{L^2}\right)\right\} \qquad (20\text{-}40) \quad (2\text{-}82)$$

Expressions 2-81 and 2-82 emphasize the fact that, when a phase-modulating screen contains more than one spatial frequency, relationships between any of its diffraction patterns are complicated functions of $\overline{FZ}$ . Functions involving Z and the first Fresnel zone are not adequate for describing the dependence of one pattern on another.

### 2.7.3 The Ionospheric Variation Required to Produce a Given Peak Phase Modulation at the Screen

Previous sections have discussed the relationship between the peak phase modulation at the screen, $\phi_0$ , and the diffraction patterns which develop behind the screen. This section develops the variation in electron density required to produce a certain value of $\phi_0$ . Since the screens are relatively thin, and the scattering is weak, the effects of multiple rays within the screen are neglected.

The phase path length of a ray from the satellite source to the receiver is found by integrating along the ray path:

$$\varphi = \frac{2\pi}{\lambda} \int \mu dz \quad \text{radians} \tag{2-83}$$

In this investigation, changes in the phase path length due to variations in the electron density are of interest. When collisions and magnetic field effects are neglected, the refractive index has the following dependence on the electron density:

$$\mu \approx \left(1 - \frac{80.62\ N(Z)}{f^2}\right)^{1/2} \tag{2-84}$$

where $N(Z)$ = the electron density per meter$^3$ as a function of $Z$

$f$ = the transmitted frequency in Hz

When the linear term of the binomial expansion of 2-84 is used for the variation in $\mu$ and is inserted in 2-83, an expression for the variation in the phase path length is obtained:

$$\Delta\varphi = -\frac{80.62\pi\lambda}{c^2} \int N(Z)\ dZ \tag{2-85}$$

The dependence of $N$ on $Z$ gives it a variation over the total path through the ionosphere. Here the variations of interest are those which occur over a small portion of the ray path. Let this small scale variation obey the function:

$$N(Z) = \begin{cases} N_M \cos^2 \dfrac{\pi Z}{2L_Z} & , \quad -L_Z \leq Z \leq L_Z \\ 0 & , \quad \text{elsewhere} \end{cases} \tag{2-86}$$

where $\pm L_Z$ is taken about the center of the small scale variation. This is a smooth function with zero first derivatives at the origin and $\pm L_Z$. When 2-86 is integrated over the limits, the total electron variation along the ray path is found:

$$\int_{-L_Z}^{L_Z} N(Z)\, dz = 2L_Z\, N_M \tag{2-87}$$

If 2-87 is inserted in 2-85 using the values: $L_Z$ = 1000 meters and $\lambda$ = 15 meters, then:

$$\Delta\varphi = 8.4425 \times 10^{-11}\ N_M \tag{2-88}$$

The values of $N_M$, which will produce certain changes in phase when the density variation follows 2-86, are given in Table 2 together with the maximum first derivative for the density function.

Table 2 Maximum Variation and Derivative in Electron Densities For Cosine-Squared Shape Blob, $L_Z$ = 1 km, $\lambda$ = 0.015 km

| radians | $N_M$ electrons/meter$^3$ | $dN_M/dz$ electrons/meter$^4$ |
|---|---|---|
| .1 | $.118 \times 10^{10}$ | $.186 \times 10^{7}$ |
| .2 | $.237 \times 10^{10}$ | $.372 \times 10^{7}$ |
| .4 | $.474 \times 10^{10}$ | $.744 \times 10^{7}$ |
| .6 | $.711 \times 10^{10}$ | $1.116 \times 10^{7}$ |
| .8 | $.948 \times 10^{10}$ | $1.488 \times 10^{7}$ |
| 1.0 | $1.184 \times 10^{10}$ | $1.860 \times 10^{7}$ |

With the blob dimension used, a peak phase modulation of 1 radian is obtained when $N_M$ is about 5 or 10 percent of the density at the peak of the ionospheric profile. If the blob was elongated in one direction such that $L_Z$ was 5 km with the dimension normal to the Z axis being one kilometer, then a value of $N_M$ which represented a 1 to 2 percent variation in the nighttime peak of the F region would give a phase modulation of 0.2 to 1.0 radian depending on the angle at which the ray passes through the blob.

When the phase diffraction patterns which represent phase differences at a point are displayed on the oscilloscope, they contain large-scale phase variations in addition to the variations due to the diffracted components.

As the integral 2-85 changes, the time of occurrence of the zero crossings at the receiver will vary. The wave at the receiver has a dependence on time and distance:

$$E_R = Ee^{j\left(\omega t - \frac{2\pi}{\lambda}\int \mu dz\right)} \tag{2-89}$$

A positive going zero crossing will occur in the real part of 2-89 when:

$$t_0 = \frac{1}{\omega}\left(\frac{3\pi}{2} + \frac{2\pi}{\lambda}\int \mu dz\right) \tag{2-90}$$

Examination of 2-85 and 2-89 shows that dt/dN is negative. An increase in N causes the zero crossing to occur earlier. Thus, for the phase difference display described in Chapter 3, the net effect for

an increase in $\int N\,(dz)$ is that the record traces for the two frequencies move apart. This occurs in the records when the ray paths move through large-scale anomalies.

In the diffraction patterns an increase in the integral of N(Z) produces a negative change in the phase modulation of each of the two frequencies. This increase causes the pattern to move out or in on the display depending on the scale size and distance from the screen to the receiver. The individual components of the diffraction patterns have coefficients which change sign as a function of distance from the screen.

# CHAPTER 3 A SYSTEM FOR OBTAINING SIMULTANEOUS PHASE AND AMPLITUDE RECORDS

The theoretical development of the previous section relates how the phase and amplitude diffraction patterns, which occur behind a phase-modulating screen, depend on the transmitted frequency, the distance from the screen, and the scale size of the screen irregularities. To permit comparisons of the patterns to be made, using the scintillations on the received signals transmitted from satellites, a system was designed for receiving two frequencies. Each of these frequencies is received at the two ends of a one km baseline antenna system. The system that evolved was specifically designed to track NASA satellite S-66.

## 3.1 The Satellite

A scientific satellite built by NASA, Space Object No. 1964-64A, known as S-66, was launched on October 9, 1964 from Vandenberg Air Force Base. Its orbit had the following characteristics:

| | |
|---|---|
| Semi-Major Axis | 7358.8 n.mi. |
| Eccentricity | 0.013 |
| Inclination | 79.69 degrees |
| Period | 104.7 minutes |

The satellite transmits CW on the frequencies of 360, 41, 40, and 20 MHz among others. The measurements made utilized the harmonically related frequencies of 20 and 40 MHz.

The relative position of the satellite to the tracking stations as a function of local time is given in Table 3 for two of the passes used to obtain scintillating records. Short segments of these records (10 seconds or less) were selected for analysis.

## 3.2 The Baseline Antenna System

The inclination of the satellite of interest was 79.69 degrees, which was taken into account in selecting the direction in which the baseline antenna system was extended. The baseline is one km in length and has a bearing east of north that will allow the sub-satellite track of some south to north passes of S-66 to be parallel to the baseline. Two antennas, one for 20 MHz and one for 40 MHz, are positioned at each end of the baseline. They are crossed, folded dipoles and are attached to poles to provide spacing from the ground plane of a little less than $\lambda/3$ .

The folded dipoles have an impedance of about 300 ohms. To assure that the maximum signal is delivered to the connecting cables, the dipoles are phased and matched as shown in Figure 27. The crossed half-wave dipoles with a length which is 0.95 of the free space half wavelength are phased together with 300-ohm lead. The connecting balun is made of RG-59, and the matching section used to couple into the RG-11 lines is a section of RG-8.

The antennas at the ends of the baseline are located at different distances from the station housing the receivers, with one location 600 feet southeast of this station. A loss of less than 10 db occurs

Table 3 Relative Position of Satellite to Tracking Station

(a) Film Run S-66-41 March 6, 1965

| Local Time | Slant Range (km) | Azimuth (Degrees) | Zenith Angle (Degrees) | Latitude (Degrees) | Longitude (Degrees) |
|---|---|---|---|---|---|
| 23 10 40 | 1605.9 | -15.337 | 61.075 | 51.3 | 82.5 |
| 23 10 50 | 1550.5 | -15.592 | 59.333 | 50.7 | 82.3 |
| 23 11 00 | 1496.2 | -15.880 | 57.445 | 50.2 | 82.1 |
| 23 11 10 | 1443.1 | -16.207 | 55.521 | 49.6 | 81.9 |
| 23 11 20 | 1391.3 | -16.580 | 53.433 | 49.0 | 81.7 |
| 23 11 30 | 1341.0 | -17.009 | 51.210 | 48.5 | 81.5 |
| 23 11 40 | 1292.4 | -17.507 | 48.841 | 47.9 | 81.3 |
| 23 11 50 | 1245.7 | -18.089 | 46.316 | 47.3 | 81.1 |
| 23 12 00 | 1201.1 | -18.774 | 43.624 | 76.8 | 80.9 |
| 23 12 10 | 1158.8 | -19.641 | 40.760 | 76.2 | 80.8 |
| 23 12 20 | 1119.1 | -20.612 | 37.712 | 45.6 | 80.6 |
| (b) Film Run S-66-43 March 10, 1965 | | | | | |
| 21 32 00 | 1268.1 | 63.146 | 47.323 | 43.6 | 68.8 |
| 21 32 10 | 1262.6 | 67.648 | 46.991 | 43.0 | 68.6 |
| 21 32 20 | 1260.7 | 72.211 | 46.855 | 42.5 | 68.5 |
| 21 32 30 | 1262.5 | 76.779 | 46.920 | 41.9 | 68.3 |
| 21 32 40 | 1268.0 | 81.297 | 47.183 | 41.3 | 68.2 |
| 21 32 50 | 1277.0 | 85.713 | 47.634 | 40.8 | 68.1 |

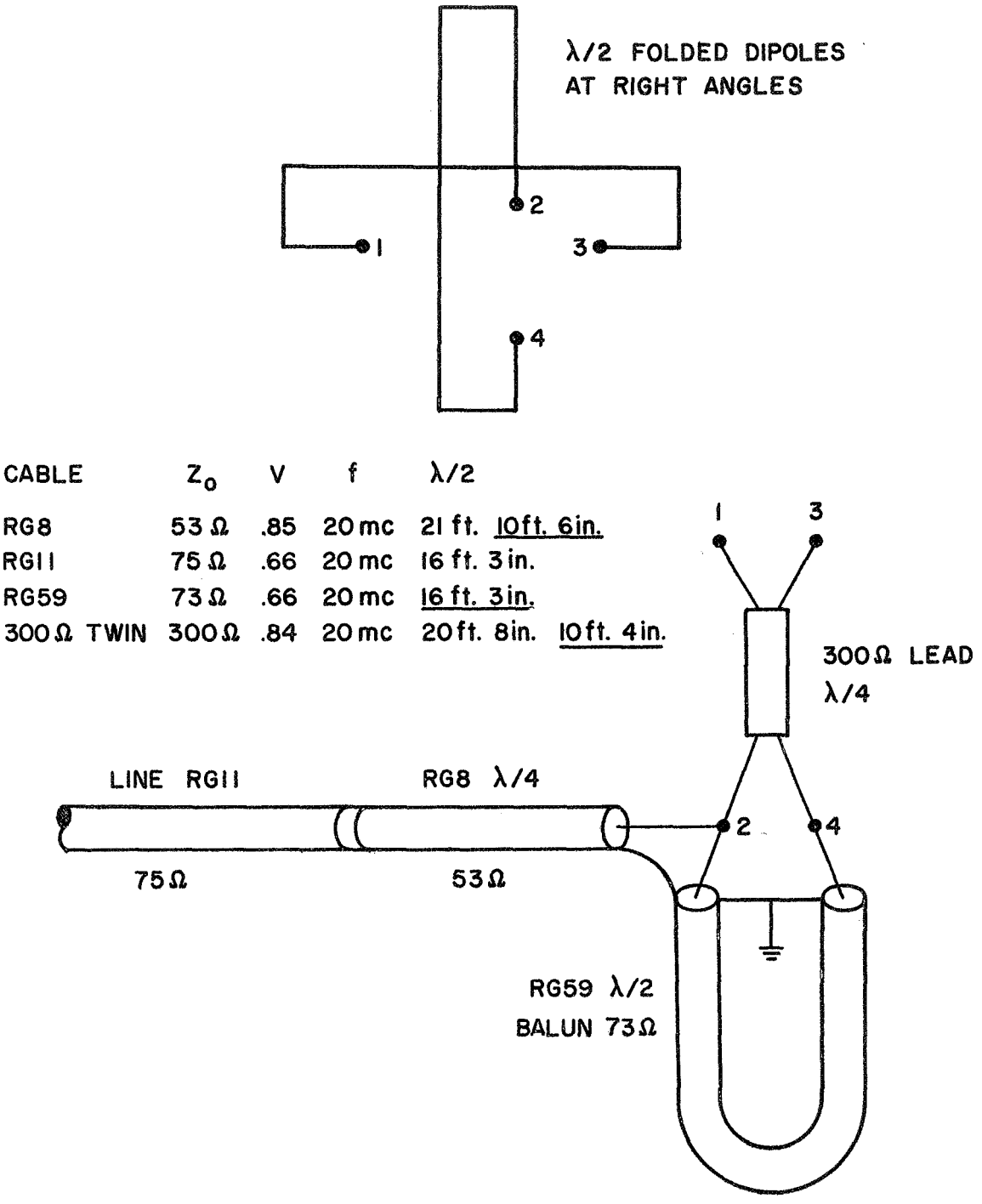


Figure 27. Antenna Phasing, Decoupling, and Matching

for the path from these antennas to the station, and is offset by use of signal stage pre-amps. The other antennas are located 3,200 feet north of the form station. To compensate for the line loss of about 40 db, multiple stage pre-amps are installed near the antennas. These pre-amps are line-powered from the receiving station.

### 3.3 Equipment for Obtaining a Simultaneous Display of Phase and Amplitude Scintillation

The equipment described here provides for the simultaneous display of the phase and amplitude scintillations as received at one location or at each of the two locations at either end of the 1 km baseline. Two amplitude scintillations and one relative phase scintillation, as well as time hacks at one-second intervals can be recorded on film and/or displayed on the oscilloscope.

The receivers, converters, and tracking filters used to transfer the H.F. signals to audio frequencies are described elsewhere[14], and thus only a broad outline of the block form of the receiving system (shown in Figure 28) is given here. The receiving system is a tracking heterodyne system in which the incoming H.F. signals beat with a locally generated signal to produce a difference frequency in the audio region. The local oscillator tracks the incoming signal as it varies with doppler shift, and maintains the difference frequency at either 250 or 500 Hz depending on whether the 20 or 40 MHz transmissions are received. The converter in the receiving system is a Tapetone Model TC-60 which has been realigned to handle 20 or 40 MHz. It has two cascade stages and a conversion stage and provides a gain of about 35 db. The receiver is a

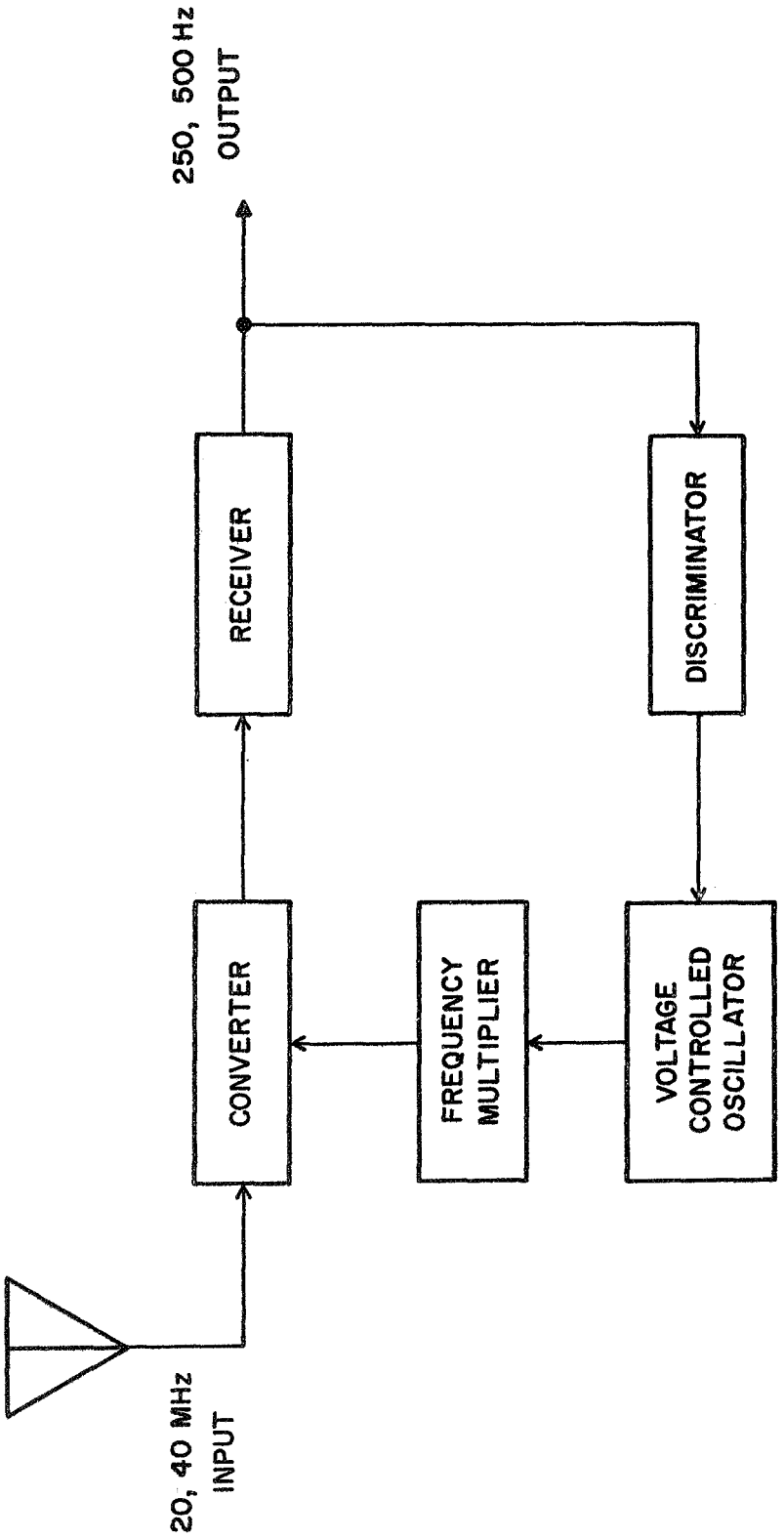


Figure 28. Receiving System Block Diagram

modified Specific Products Model SR-7, which is doubly converting and has sensitivity of better than 2 microvolts. The discriminator circuit takes the audio output which is limited and split into two components with a relative phase of 90 degrees at the desired audio output frequency. These phase-shifted components drive a balanced modulator. At frequencies above or below 500 Hz, the output has a zero frequency component with magnitude proportionate to the deviation and polarity, depending on the direction of the deviation. This output is applied to a voltage-controlled oscillator with a nominal frequency of 1 MHz. Its output is used by a frequency multiplier which furnishes the correct beat frequency to the converter stage. In this fashion the frequency tracking loop is closed to provide the desired outputs of 250 or 500 Hz. Through the outputs of the frequency multiplier, one tracking loop is able to supply four receivers (two frequencies are tracked at each end of the baseline) with the correct heterodyne frequencies.

A block diagram of the equipment used to process either the live or recorded signals is shown in Figure 29, and is intended to illustrate only the functions of the units and not all connections. Only those chassis peculiar to the system, not previously descrived[14], [15], are discussed in detail.

The equipment of interest is assembled in one rack, which takes the output of the receivers with frequencies of about 250 and 500 Hz and converts them to a film record for use in analysis of signal scintillations.

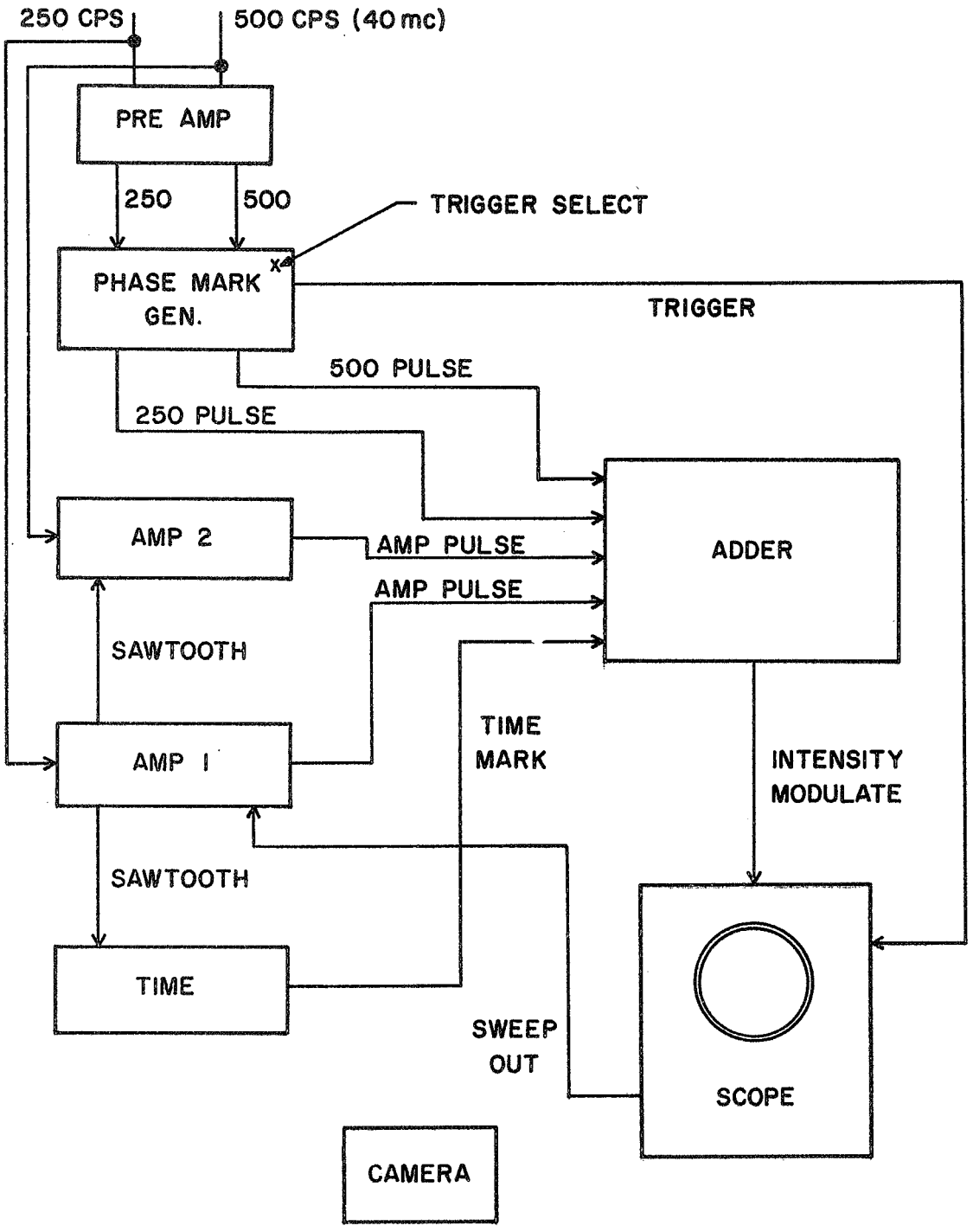


Figure 29. Block Diagram of Signal Processing System

The positive-going zero crossings of the audio frequencies are used to generate pulses, one of which is used to trigger the oscilloscope. The signals are also fed to amplitude detectors whose envelope is used to generate a pulse, the position of which, with respect to the trigger pulse, is proportionate to the amplitude. A time mark pulse is also generated. All of these pulses are added and used to intensity-modulate the beam of the scope. As scintillation in amplitude and in relative phase occurs, the dots on the scope move back and forth with respect to the trigger mark. A continuously moving film records this motion which can be used for analysis.

### 3.3.1 The Non-Linear Pre-Amplifier

To assure steep zero crossings over a wide range of inputs, a non-linear amplifier (see Figure 30) is needed to amplify the weak signals and limit the high portion of the signals. This amplifier has two channels which can be fed from common or separate inputs. The grid circuits of the first stages have parallel resonant filters that are tuned to 250 and 500 Hz. The output of the first stage is fed into a network that isolates the d.c. and feeds the a.c. signal across two diodes of reversed polarity, which yields a maximum output for the stage of about ± 1 volt. Then small input signals are amplified while larger signals are amplified and then limited. The following two stages give an adjustable gain and an impedance match.

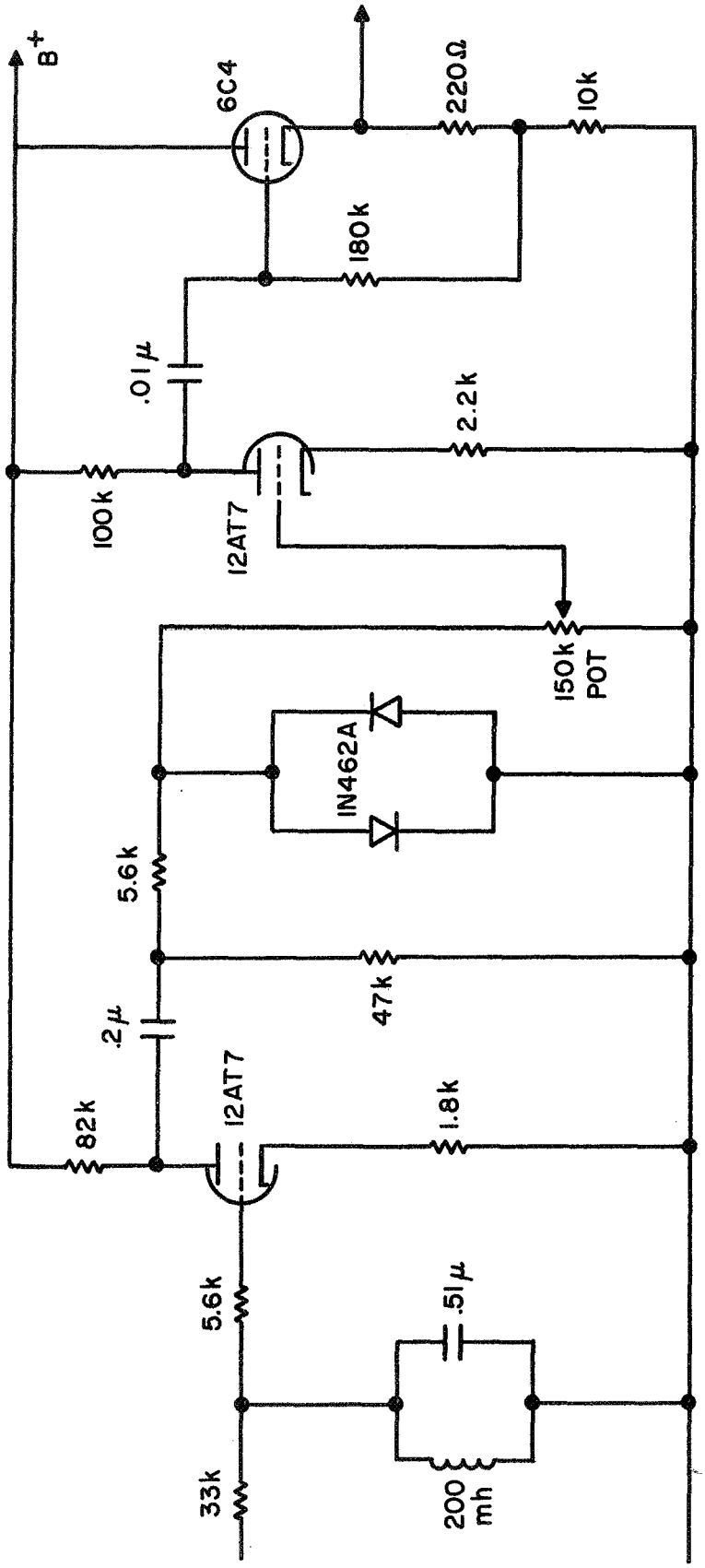


500 Hz CHANNEL, SIMILAR CHANNEL FOR
250 Hz WITH CHANGES IN FILTER

Figure 30. Non-Linear Pre-Amplifier

### 3.3.2 The Phase Mark Generator and Trigger Amplifier

This one unit contains three pulse generation channels and a trigger selector and amplifier. The channels are tuned for frequencies of 250 and 500 Hz. The inputs can all be separate or the 250 and 500 Hz can be common.

The input stages are tuned to reject unwanted frequencies, and the filters for the 250 and 500 Hz channels are of the series parallel resonant type. The output of the first stage is isolated by use of transformers, and is clipped by IN462A diodes. The resulting rectangular wave is then differentiated to produce pulses, and the positive-going pulse is removed by use of another diode. The outputs from each of the three channels then go to the adder.

The 250 cps and 500 cps pulses are also connected to a switch where either can be selected for amplification in the trigger circuit. The trigger circuit has two stages and adjustable gain, and the output trigger pulse is used to trigger the oscilloscope. This unit is shown in Figure 31.

### 3.3.3 The Amplitude Units

Except for minor differences these two units are alike; they both have as an input one of the receiver outputs of the signal recorded on a channel of the tape recorder. The waveform generated is a negative pulse whose time displacement from the pulse which triggers the scope sweep is proportionate to the amplitude of the input signal. These pulses are generated by comparing two voltages.

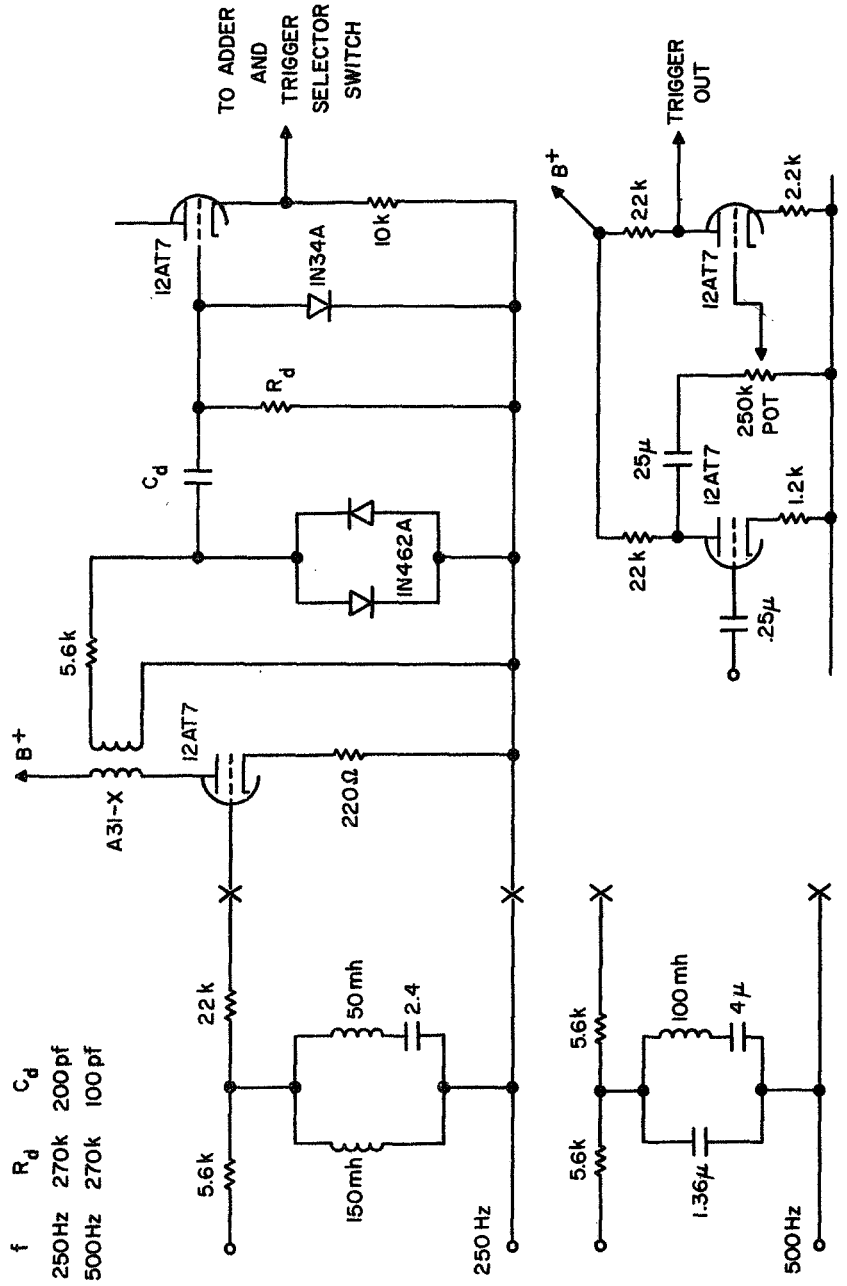


Figure 31. Phase Mark Generator and Trigger Selector

First the input signal is amplified and detected in a manner that gives, for the output of the first stage, a negative voltage proportionate to the amplitude of the input wave. This negative voltage is fed to a common summing point by a 39K resistor; the other voltage at the summing point is a positive-going ramp generated by the oscilloscope sweeper circuits. The scope sweep voltage is fed to Amp Unit 1, where is is divided, biased, and passed through a cathode follower. The voltage waveform out of the follower is used by Unit 1 and is also connected to Unit 2 and the Time Mark Generator. In each case, the positive-going wave is fed to a summing point through a resistor.

The summing point is connected to ground by two diodes, in parallel but with reversed polarity. At the start of the sweep, the voltage at the point is negative and small due to switching action of the diodes. When the sweep voltage is larger than the magnitude of the detected voltage, the voltage across the diodes is positive and small. However, during the transition time when the sweep voltage is within ± 1V of the magnitude of the detected voltage, a positive-going ramp is generated.

The positive-going ramp is then amplified by the following two stages, the last of which has a transformer-coupled output. The waveform is biases so that the steepest negative slope passes through zero; then the wave is clipped and differentiated to produce pulses. The positive pulses are removed and the output is obtained from a cathode follower. The amplification stages are used to produce a steeper slope than that produced by the scope sweep.

The differences between the two amplitude units are in the sweep circuits and the provisions for time marks. Unit 1 contains the circuit for modifying the sweep wave form, and Unit 2 is connected to the timer switch. The timer switches in, for a fraction of a second, a 10K resistor in parallel with the 47K resistor that feeds the sweep wave to the summing point. This causes an abrupt displacement of the amp pulse and serves as a time mark, as well as for identifying the output of Unit 2. See Figure 32.

3.3.4 The Time Mark Generator

The same principle is used for pulse-generating in this unit as is used for the amplitude units, the difference being that the negative voltage is supplied by the dry battery pack. A voltage divider circuit is used to position the time mark at the right edge of the scope trace.

Since the time mark appears only during that fraction of a second when the synchron cam is not suppressing the switch, and at the end of the trace, adequate pulse sharpening is obtained through use of one amplification stage. The bases of the negative-going pulses are removed by the series 1N629 diodes. A small capacitor is placed across the output to filter out the high frequency components which arise from the switching action.

The 30 RPM synchron cam provides time marks spaced by 2 seconds; on alternate seconds it also gives interrupts of the output of the Amp 2 Unit. Thus, time marks are provided at one-second intervals. (See Figure 33.)

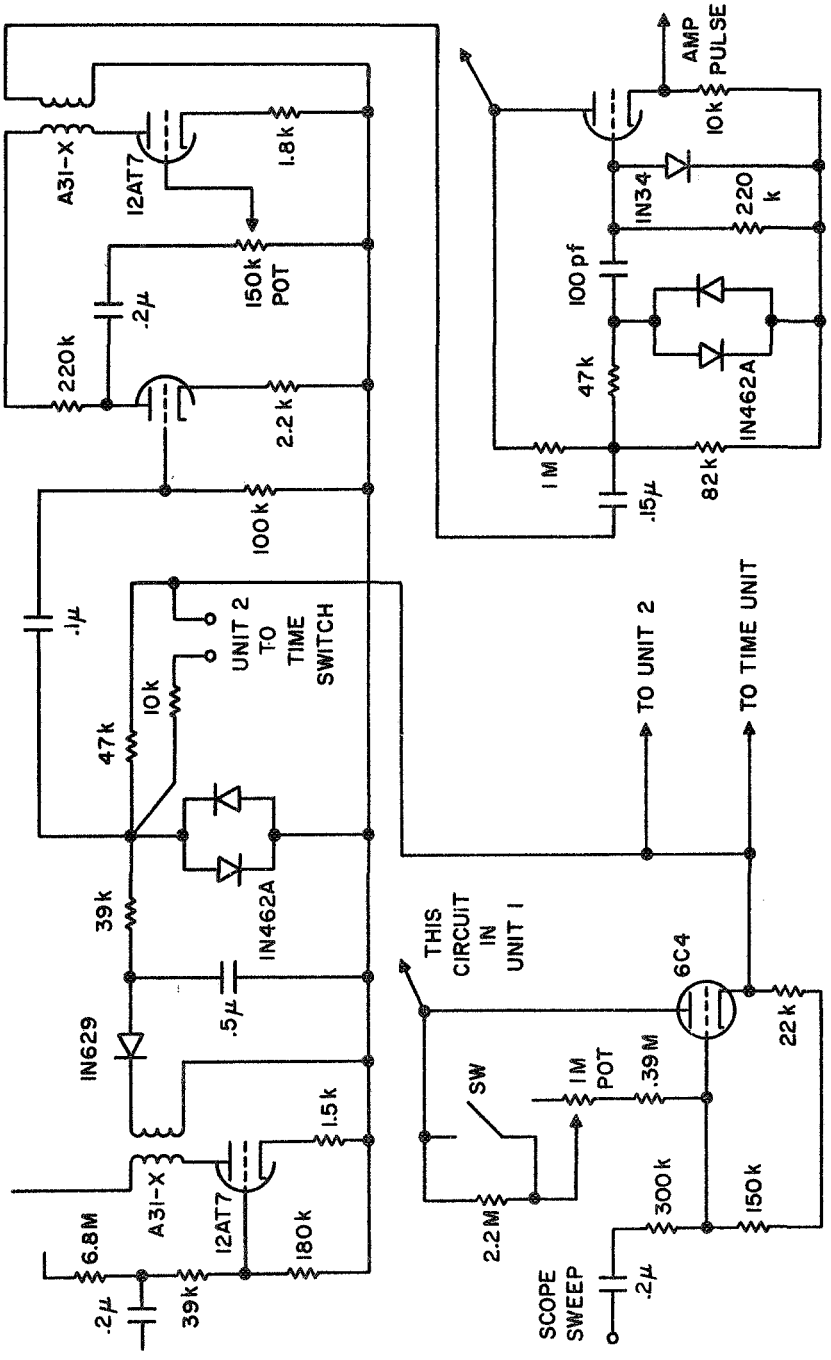


Figure 32. Amplitude Pulse Unit

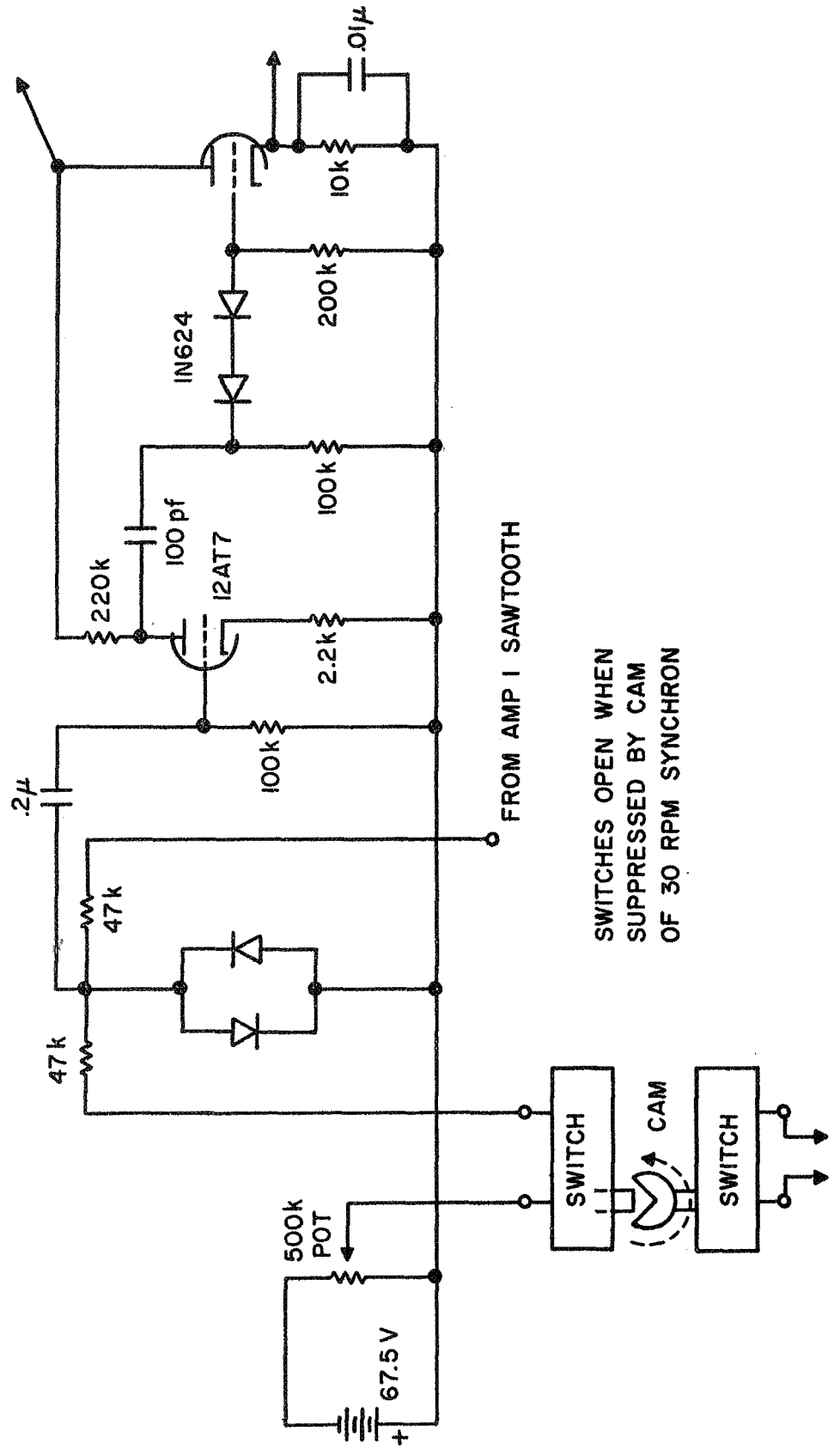


Figure 33. Time Mark Generator

### 3.3.5 The Adder

The Adder is located in a chasis with a limiter and pulse amplifier, and is basically an operational type amplifier with multiple inputs and resistive feedback. The input and output impedances are selected to give near unity gain. The time mark impedance is adjusted to give a darker trace for easy identification. The first two stages are cathode-coupled with the second stage having a grid bias which can be used to null the output when no input is present.

Once the input impedances are balanced, the same input jacks are used for the same signals since the relative magnitude of the pulses from the phase and amplitude units differs only slightly. The output voltage is then a function of the input voltages:

$$e_o = Z_0 \sum_{i=1}^{5} \frac{e_i}{Z_i}$$

The other circuits in the Adder unit are: a limiter, two stages of gain, and a cathode follower whose output is a series of negative pulses. As the phase and amplitude of the received signals vary, the pulses will show displacement in time with respect to the trigger pulse. In some instances, two and even three pulses could be superimposed. The limiter is adjusted to simply dip off the top of a single pulse; then superimposed pulses do not give an output of greater intensity. Since several volts are required to properly modulate the intensity of the oscilloscope beam, two stages of gain follow the limiter. A pot provides adjustment to the right level. The summed, limited, and amplified

negative pulses are then fed out through a cathode follower to the CRT cathode of the oscilloscope. (See Figures 34 and 35.)

3.3.6 The Oscilloscope

A Tektronix Model 532 is used, and is set to sweep 250 times per second, using an external trigger from the Phase Mark Generator. The ground disconnected from the CRT cathode at the back of the scope and the output of the Adder is then fed into this point. The sweep is fed out to Amp Unit 1 where it is reduced and used in the generation of pulses from Amp 1 and 2 as well as the time units. The sweep is also fed to external sweep where it is alternated to produce a narrower sweep on the screen (one that can be fully photographed).

It is possible for a full sweep of the scope to show five dots on the screen. At the left edge is a dot coincident with the 250 Hz trigger pulse. (Other modes of operation can be used.) Two other dots are present, spaced apart by one-half sweep, and showing the relative position of the 500 Hz zero crossings. Also present is a dot representing the amplitude of the 250 Hz and the 500 Hz signals. On alternate seconds, spaced two seconds apart, a time mark will appear at the right edge of the sweep. All dots except the trigger and time marks dots show lateral displacement with time when the satellite signal scintillates in phase and amplitude.

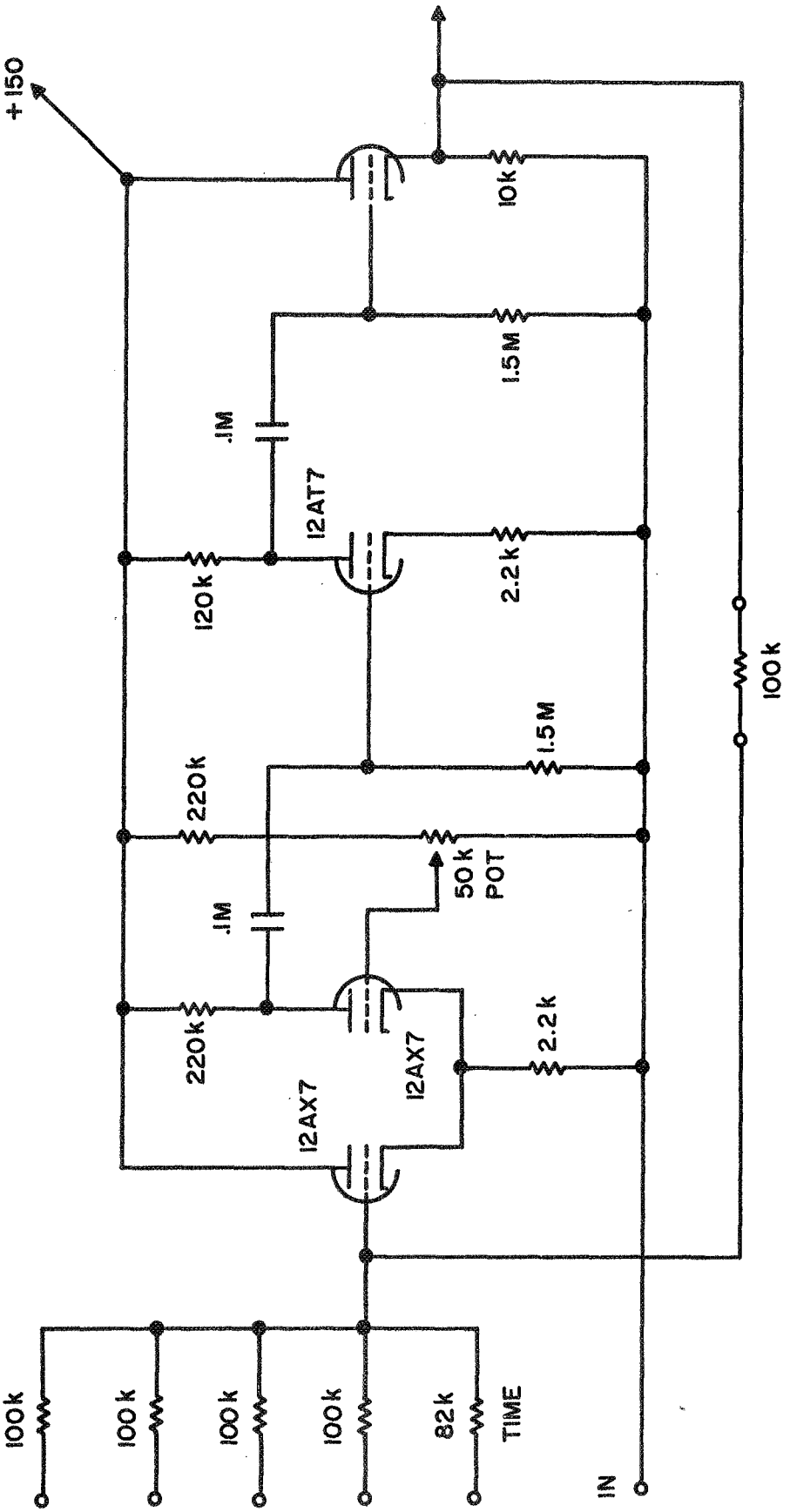


Figure 34. Adder

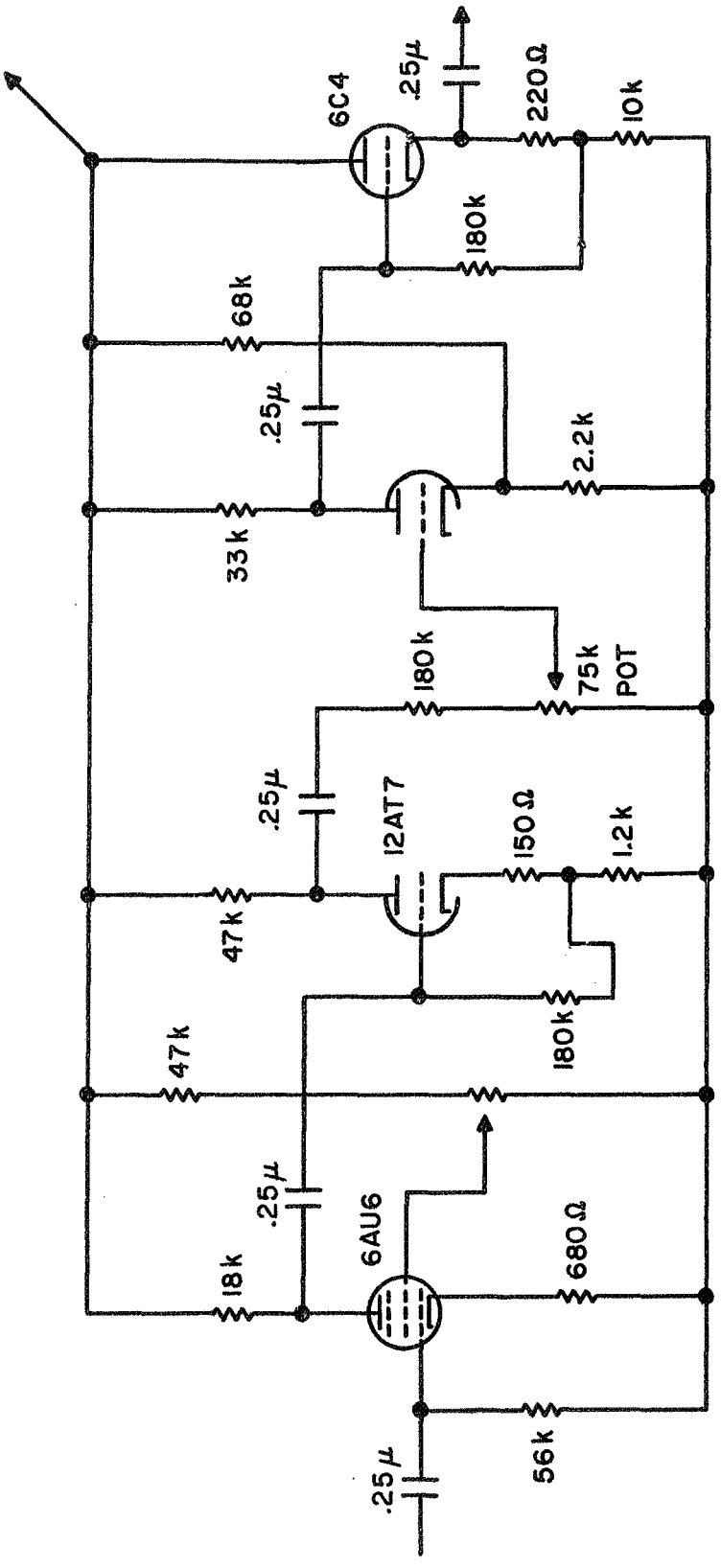


Figure 35. Clipper Amplifier

### 3.3.7 The Camera

A Cossor 35 mm camera is used to photographically record the time-varying display on the oscilloscope screen. The integration effect of the film results in as many as five lines if the trigger on the left edge of the scope face is included. The camera motor is set to drive the film at a rate of one inch per second, which provides film records with scales convenient to project for processing.

The projection of one second of film run is shown in Figure 36 For this case, the amplitude is for the 20 MHz signal. The phase is the relative phase between the 20 and 40 MHz signals received at the same point, and the full scale mark is $2\pi$ radians in phase. Only one relative phase track is shown here. Full scale yields two traces for the 40 MHz (250 cps) signal.

## 3.4 The Simultaneous Records Obtained

The baseline antenna system described in the previous section is used to receive satellite signals which are recorded and then processed to produce simultaneous phase and amplitude patterns. The 20 MHz and 40 MHz signals from both ends of the baseline are converted to audio of 250 Hz and 500 Hz, respectively, before being recorded on four channels of an Ampex recorder. The two records from signals received at one end of the baseline can be used to generate three patterns. When the two audio signals are fed to the amplitude units described in Section 3.3.3, simultaneous amplitude diffraction patterns are produced in film records. If the same signals are fed into the phase mark generator unit described in

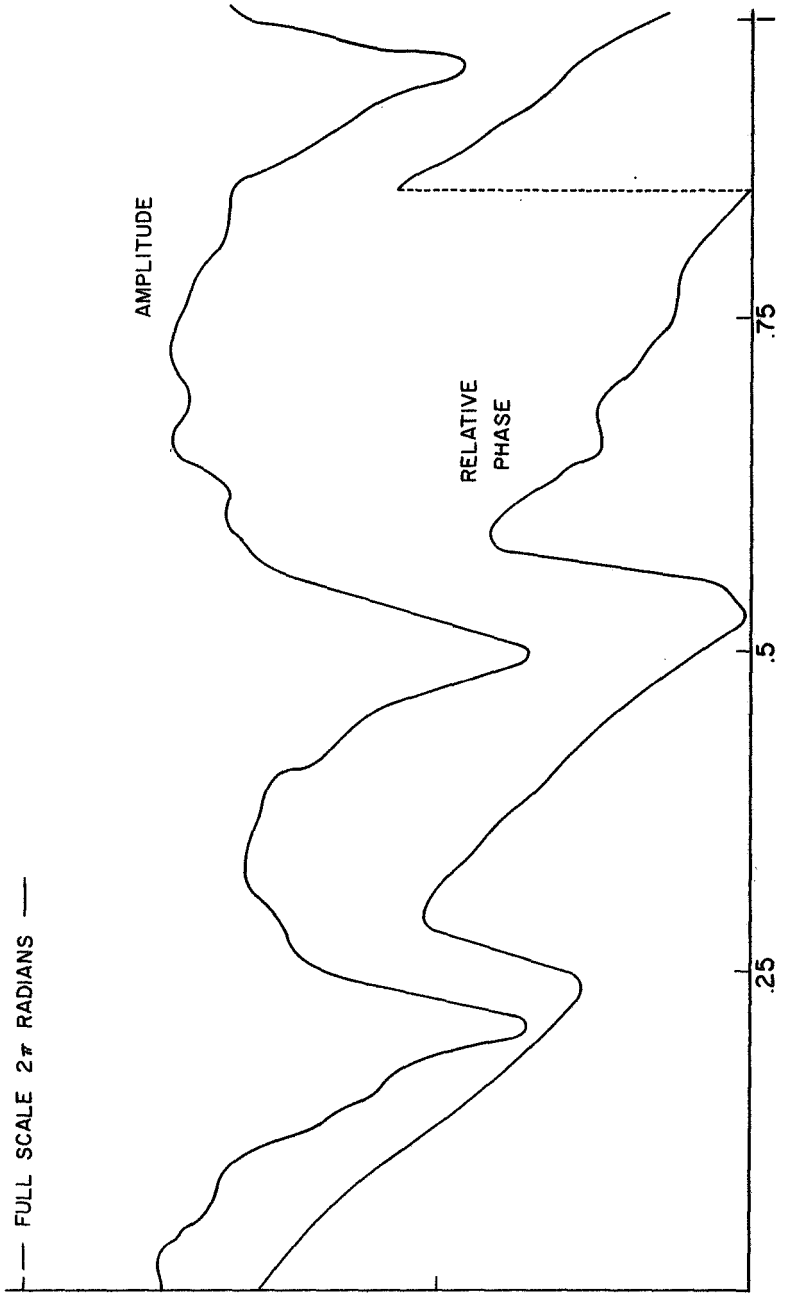


Figure 36. Projection of One Second of Film Run and Amplitude and One Phase Trace

Section 3.3.2, a phase diffraction pattern is produced from their relative phase. These three simultaneous diffraction patterns can be recorded on the same film for comparision and analysis.

When the total of four signals received at both ends of the baseline are taken together, several diffraction patterns can be produced: two amplitude patterns and one relative phase difference pattern across the baseline. The 20 MHz signal was used for this interferometer pattern. One of the 250 Hz signals from the recorder was first doubled so that the same equipment could be used for generating phase marks. One satellite pass then produces seven patterns for comparison and analysis.

# CHAPTER 4 METHODS OF DATA ANALYSIS

The analysis of the phase and amplitude records detailed herein permits comparison of the recorded phase and amplitude diffraction patterns with those calculated using the theoretical phase-modulating screens. The modifications produced by geometry and method of measurement, discussed in Section 2.7, have been considered. The various diffraction patterns obtained using the equipment described in Chapter 3 were sampled at uniform intervals, and the resulting data points were used as input arrays to two different Fourier analysis computer programs. The closeness with which these programs represented the harmonic content of the input functions was determined by use of a number of sample input arrays for which the Fourier spectra were known.

When the spectra for the phase and amplitude patterns measured at the Earth's surface were determined, they were projected back to the height of the screen where they originated. This was based on the assumption that the phase and amplitude patterns had the same origin. The differences of the Fourier spectra of the pattens projected back to an incremented screen height were then minimized in a lease-squares manner.

## 4.1 Fourier Analysis of Records

All the theoretical phase-modulating screens developed in Chapter 2 could be represented, with small error, by a finite number of Fourier components. To compare the theoretical diffraction patterns these screens produce with the diffraction patterns recorded during satellite passes, two computer programs were written and used to process

the data. One program computes the autocovariance function of a data sample and takes its cosine transform to obtain the power spectral density. The other program calculates the Fourier coefficients for a segment of the data sample assuming that the sample represents one period of a repetitive function. In each case, the d.c. value is extracted first, but the a.c. and d.c. powers and their ratios are obtained as part of the program output.

The use of two different programs was dictated by the concept that the real diffraction patterns to be processed were neither deterministic or random, but contained a measure of each. It is known that any interval of any function can be represented by a Fourier series expanded in terms which are harmonic within its length. When the function is orderly, this series may indicate the presence of relatively strong quasi-periodic terms, although the precise distributions of coefficients is sensitive to the particular end points and how they relate to these periodicities. In the more general case of a random function, the Fourier series coefficients are not a good indication of the distribution of spectral power and an approach based on the autocovariance function may be used.

As indicated, the use of two programs enables consideration of both periodic and random time functions. The basic tool for analysis of functions, which are principally periodic, is the Fourier series program. The tool for analysis of the random functions is the autocovariance and spectral density program. The Fourier analysis theory used to develop the simulation program is widely known and is discussed only briefly.

4.1.1. Harmonic Analysis Using Fourier Series

If $f(t)$ is an arbitrary real function in the interval $t_1 \leq t \leq t_2$, it may invariably be represented by a Fourier series:

$$f(t) = \frac{a_0}{2} + \sum_{n=1}^{\infty} (a_n \cos n\omega_0 t + b_n \sin n\omega_0 t) \qquad (4\text{-}1)$$

where $t_2 - t_1 = T$ and $\omega_0 T = 2\pi$

The Fourier coefficients, $a_n$ and $b_n$, of 4-1 are defined by:

$$a_n = \frac{2}{T} \int_0^T f(t) \cos n\omega_0 t \, dt \quad , \quad n = 0, 1, 2 \qquad (4\text{-}2)$$

and

$$b_n = \frac{2}{T} \int_0^T f(t) \sin n\omega_0 t \, dt \quad , \quad n = 0, 1, 2 \qquad (4\text{-}3)$$

The Fourier series program gave as an output a normalized value for $c_n$ where:

$$c_n = \left( \frac{a_n^2 + b_n^2}{2} \right)^{1/2}$$

The array for the values $c_n$ was divided through by its largest member to obtain the normalized array of Fourier coefficients.

Using this program, the input which is a sampling of a diffraction pattern, is treated as one period of a periodic function. The program then maps the significant terms from the time domain into the frequency

domain. Care must be taken in selection of a sampling procedure so that the program output will represent the spectrum of the function being sampled.

Among the errors that must be considered are round-off, truncation, and aliasing errors. The round-off errors were minimized by sampling using three significant figures; the truncation errors were minimized by sampling long enough to represent full periods of the lowest frequencies present. The aliasing errors occur when the high frequency components of a time function impersonate low frequencies, which results when the sampling rate is too low. This error was removed by making certain that the sampling rate was high enough for the highest significant frequency to be sampled at least twice during each cycle. Because of these considerations, most of the computer runs were made using input arrays which covered sections of five to ten seconds of diffraction patterns which were sampled at the rate of 20 per second.

The Fourier coefficient program written to obtain $a_n$, $b_n$, and $c_n$ gave as additional outputs the mean, variance, and ratio of a.c. to d.c. power for the input arrays. The program was checked using a number of input arrays obtained by sampling analytic functions. The output Fourier spectrum calculated by the computer program was then compared with the spectrum known to represent the analytic function. The output of this Fourier amplitude coefficient program was found to give a very good representation of the expected spectrum; this was true even for harmonic components which had very little amplitude.

4.1.2. Harmonic Analysis Using Power Spectral Density

Assume that $f(t)$ is the periodic function represented by 4-1. Then the power spectrum may be obtained from the Fourier cosine transform of the autocovariance function. The autocovariance function operates on $f(t) - \mu$ where $\mu$ is the mean value of $f(t)$ over the interval $T$. If the time average of the periodic function $f(t)$ over a period is zero, then the autocovariance, $\psi_f$ is defined as:

$$\psi_f(\tau) = \frac{1}{T} \int_{t_1}^{t_2} f(t)\ f(t - \tau)dt \qquad (4\text{-}6)$$

where $0 \leq \tau \leq T$, and $t_1$, $t_2$ are the limits of the sample being analyzed.

If a function, $y(t)$, has a time average $\overline{y(t)}$, then the substitution $f(t) - y(t) - \overline{y(t)}$ is made in 4-6 and the autocovariance of the function $y(t)$ becomes:

$$\psi_y(\tau) = \frac{1}{T} \int_{t_1}^{t_2} y(t)\ y(t + \tau)dt - \left( \frac{1}{T} \int_{t_1}^{t_2} y(t)dt \right)^2 \qquad (4\text{-}7)$$

For either case, the power spectral density, $\Phi$, is given by the Fourier cosine transform of $\psi(\tau)$ :

$$\Phi(n\omega_0) = \frac{1}{T} \int_{0}^{T} \psi(\tau)\ \cos\ n\ \omega_0\ \tau\ d\tau \qquad (4\text{-}8)$$

where a finite portion of the record is analyzed by applying a unity amplitude data window of length, $t$.

Here the term power spectral density is used in contrast to the power spectrum of Section 4.1.1. The power spectrum is associated with the Fourier series method, and has a discrete or line spectrum corresponding to the values of $n$. The power spectral density given by 4-13 is also a line spectrum. However these spectra are equivalent only when the function being analyzed is periodic in the sample interval with zero mean.

If samples are taken over the time interval, $T$, and the correlation shift is for $\tau = T$, the required total data sample is 2T. This means that the lowest frequency which can be represented in the output is $1/2\ T$. The highest frequency which can be represented is still the reciprocal of twice the sampling interval. Thus, twice as much data is handled and twice as many frequencies are available than for the Fourier series methods of 4.1.1.

A correlation and power spectral density program was written to process the diffraction pattern records. This program also can be used to obtain cross-correlation functions and cross-power-density spectra. The correlation functions calculated by this program are the normalized autocovariance and cross-covariance functions. When the power spectral densities are developed, they are normalized since the relative power distribution is considered to be most important for diffraction pattern analysis. The mean value, variance, and ratio of ac to dc power are also calculated for each input array.

As mentioned previously, the fact that the input sample is taken over a finite time causes the input to be multiplied by a unity data window of length $T$. The corresponding convolution in the frequency

domain results in the spectrum being blurred by Sin X/X-shaped pulses. The "leakage" of the power of a given frequency through the side lobes of the shaping function can be reduced by applying a data window to the time series which has lower sidelobes in the frequency domain than the rectangular data window. The spectral density program uses a hamming lag window to suppress spurious frequency components.[17]

4.1.3. Comparison of Records

The amplitude patterns generated by the simultaneous film display are sampled for obtaining a computer program input array by projecting them on a reader. The phase records, $\psi(20\text{-}40)$ , show a very slow periodic behavior as the integrated electron content from satellite to the receiver varies. This ramp must be removed before the computer inputs are acceptable, which is accomplished by fitting a constant slope through the total sample to be used. The first and last values are made to correspond by subtracting their difference. A scaled amount is then subtracted from each intermediate value. Amplitude and phase records similar to those sampled for the computer programs are shown in Figures 37 and 38.

Since an attempt is made to treat the records as periodic functions, the last sample taken from the diffraction record usually is one with a magnitude approximately equal to that of the first sample. The sampling interval selected then is one which eliminates a step function between the first and last samples. If the time function selected were discontinuous between these two points, a truncation

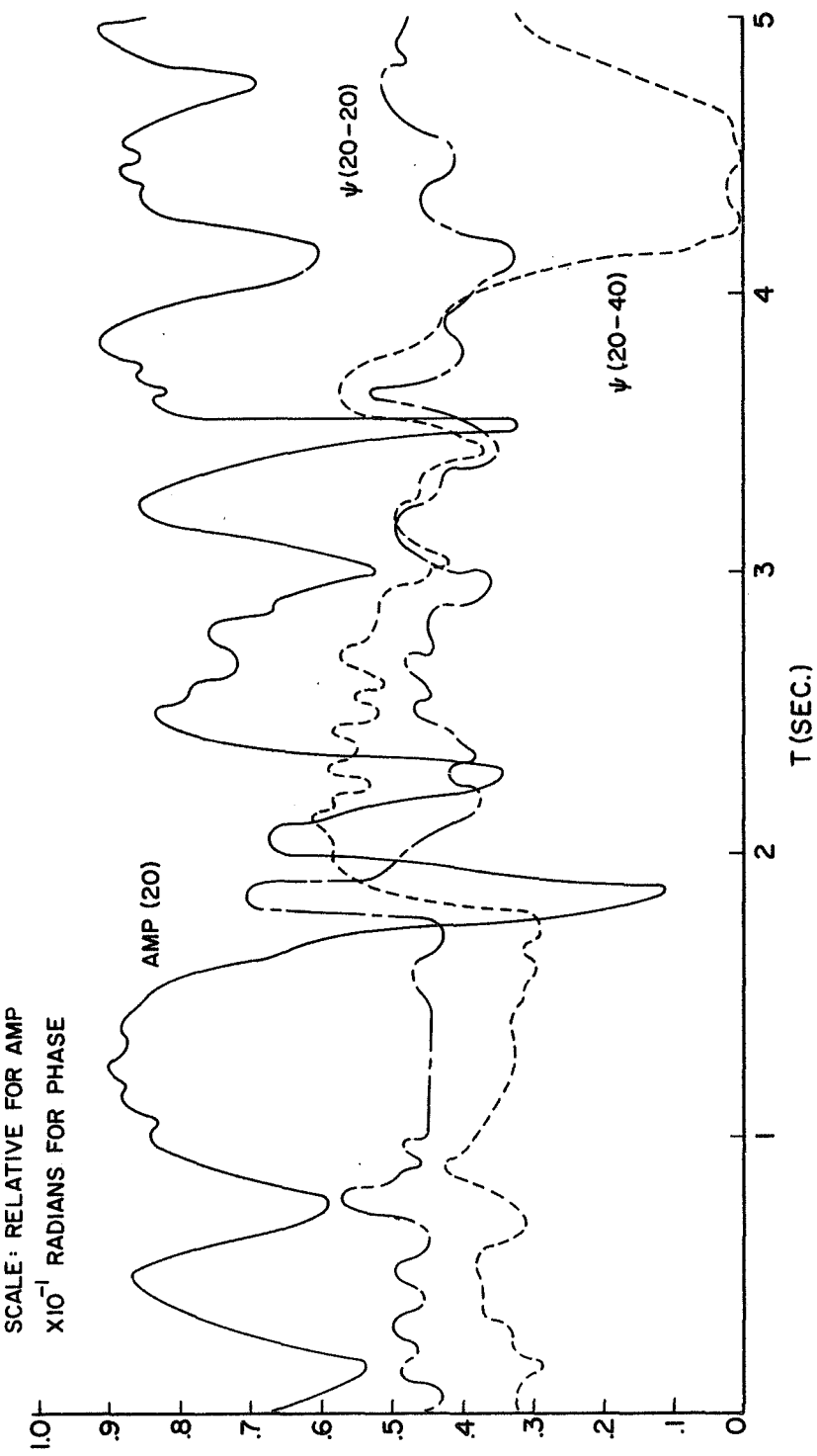


Figure 37. Phase and Amplitude Diffraction Patterns Scaled for Fourier Analysis, M IV 64-69

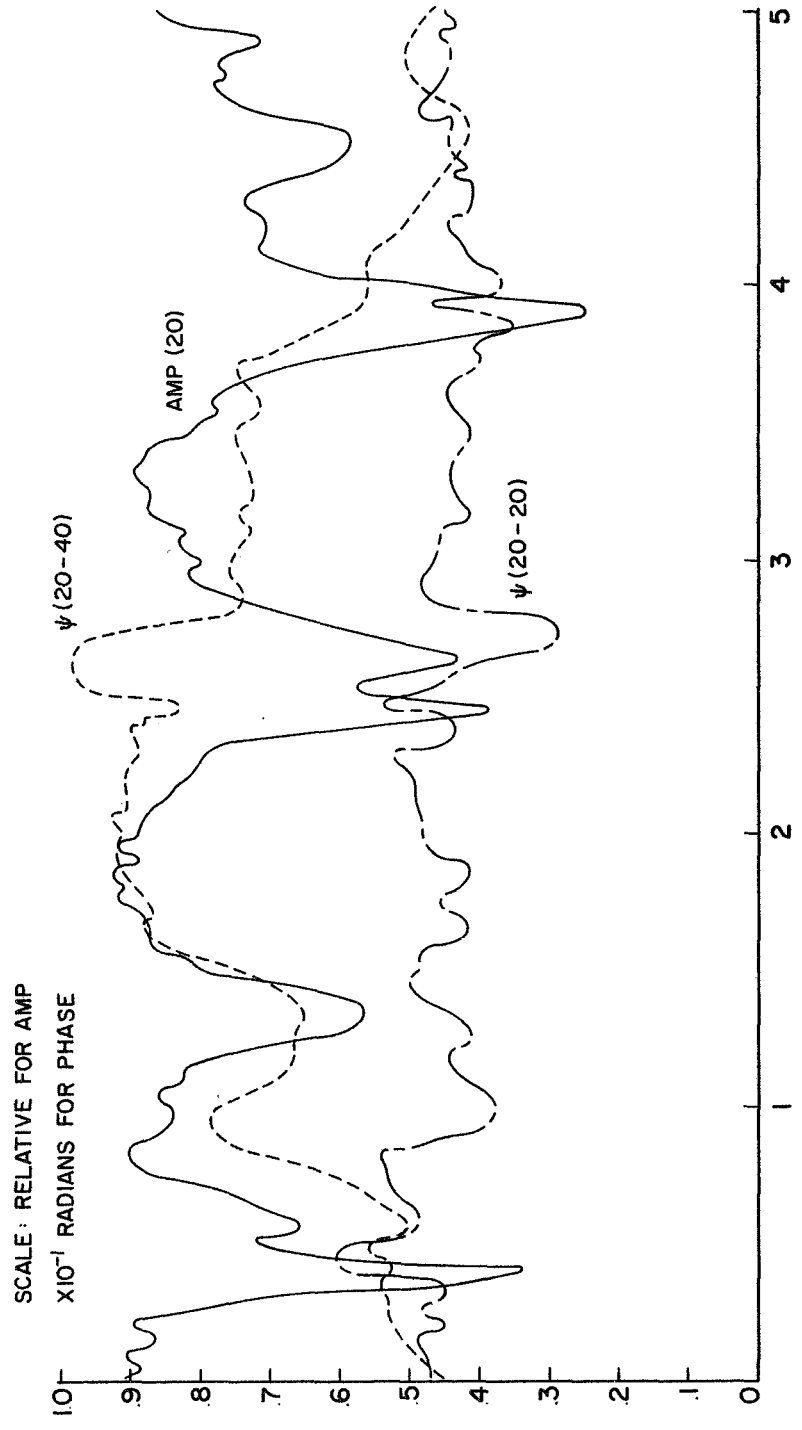


Figure 38. Phase and Amplitude Diffraction Patterns Scaled for Fourier Analysis, M IV 69-74

error would result that could not be eliminated by increasing the number of samples taken. In fact, this Gibb's phenomenon error will become more pronounced as the sampling rate is increase. In addition to this magnitude match, a rough attempt is made to match the slopes at the first and last sample points.

The relationships shown to exist between the theoretical phase and amplitude diffraction patterns of Chapter 2 are observed in the measured patterns. First, the large phase excursions always occur in conjunction with amplitude nulls; in some cases the phase excursions are in the $\psi(20\text{-}40)$ pattern; in other cases they are in the $\psi(20\text{-}20)$ patterns. Second, the nulls in the amplitude patterns are sharper than the peaks; for phase, which is not an absolute value function, notches in either direction have equal sharpness. It is worth noting here that, when a transmitted wave is disturbed by phase modulation in a purely random fashion, rapid excursions for an increase or decrease of amplitude are equally likely. The third significant characteristic for comparison is that the $\psi(20\text{-}40)$ diffraction pattern contains spatial frequencies lower than those of the amplitude patterns, while the $\psi(20\text{-}20)$ pattern contains relatively more high frequency terms than the amplitude pattern. The differences can be accounted for. The low frequency terms of the $\psi(20\text{-}40)$ pattern do not have enough distance, $Z$, for developing in the amplitude pattern. The $\psi_I(20\text{-}20)$ baseline interferometer filters out the low frequency terms because of its length.

The normalized autocovariance functions calculated for the simultaneous patterns shown in Figure 37 are presented in Figures 39 and 40, and were calculated using the Power Spectral Density program. The low frequency terms in $\psi(20\text{-}40)$ are shown by the slow fall-off of the autocovariance function. The amplitude correlation function is shown as calculated for two runs having a slightly different time interval. These plots demonstrate the repeatability of the process of generating film records, projecting, and sampling for the computer program. The normalized autocovariance function for the interferometer phase, $\psi(20\text{-}20)$ shows the high frequency terms and the rapid drop-off near d.c. This correlation function is indicative of a random process. The other autocovariance function on Figures 39 and 40 is typical of a more deterministic function. Figures 41 and 42 show the normalized power density spectrums which result from the cosine transforms of the functions of Figures 39 and 40. Again, the repeatability in the amplitude spectrum is observed. Most of the energy is in the low frequency terms for $\psi(20\text{-}40)$ , $\psi_I(20\text{-}20)$ has a more random spectrum with an average power of only one tenth of that for $\psi(20\text{-}40)$ .

Figures 43 and 44 show the normalized amplitude spectrums which result when the same diffraction records are processed using the Fourier coefficiant program. A comparison of Figures 41 and 42 with 43 and 44 reveals that the Fourier coefficient program is more sensitive for locating regions of the spectrum where no energy exists, and the rapid drop-off for narrow spectra. It is apparent that a more random spectrum exists when the baseline filter for $\psi_I(20\text{-}20)$ eliminates the low

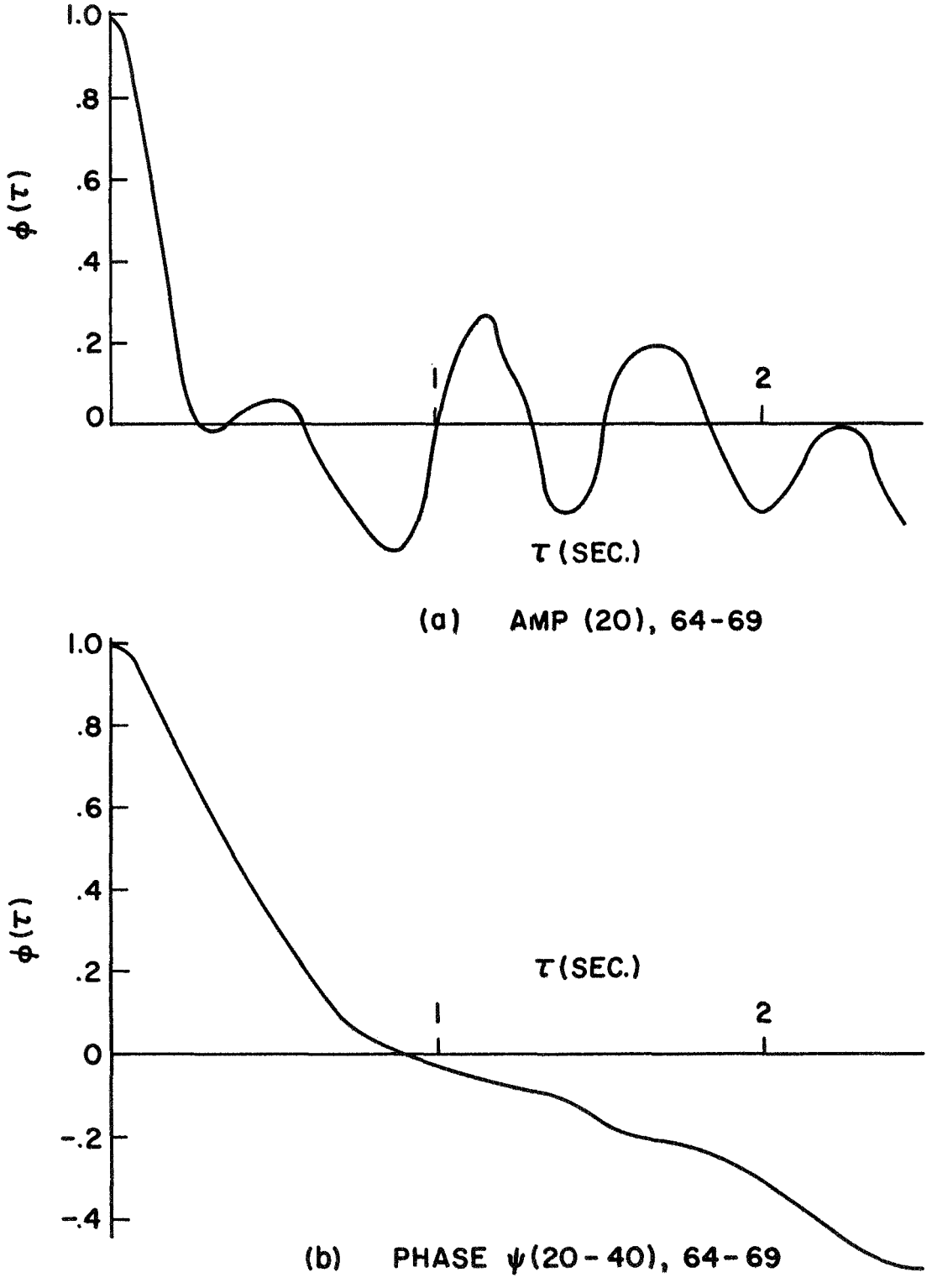


Figure 39. Normalized Autocovariance Functions for Run M IV 64-69

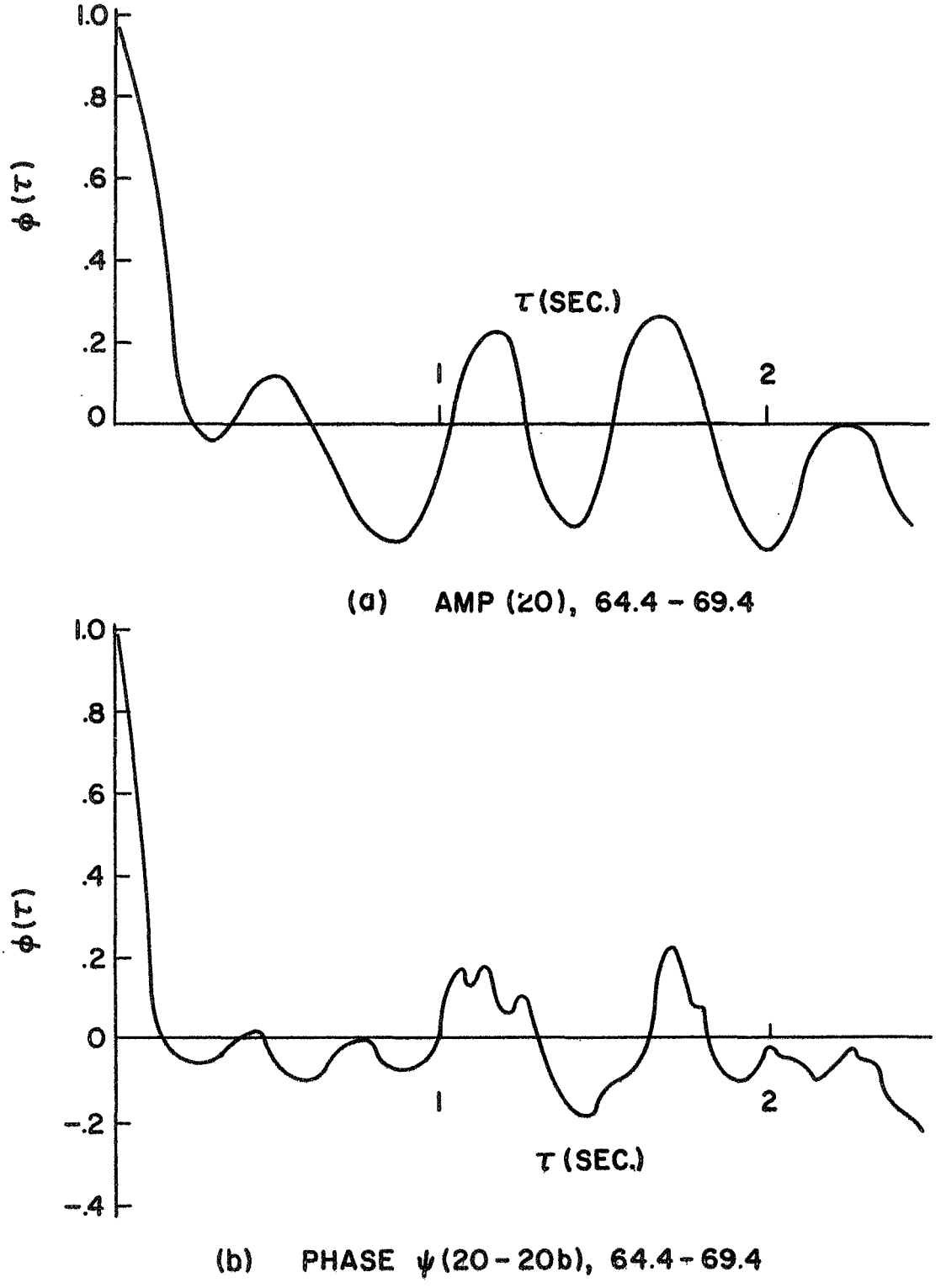


Figure 40. Normalised Autocovariance Functions for Run M IV 64.4 - 69.4

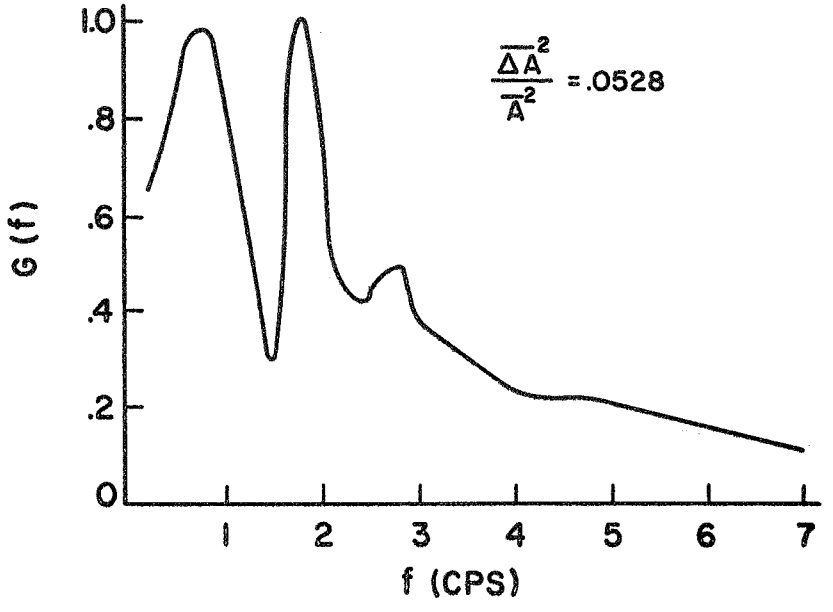


(a) AMP (20), 64-69

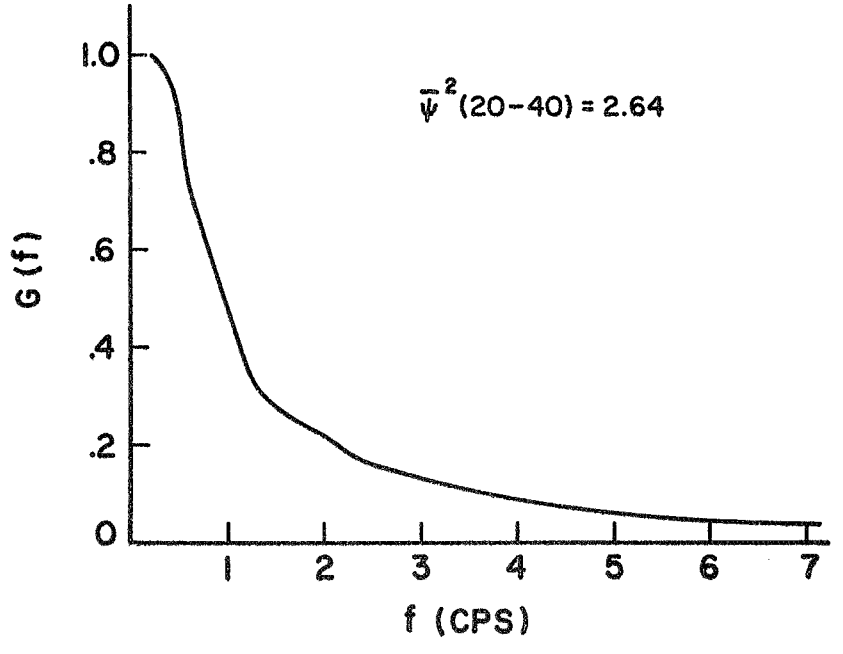


(b) PHASE $\psi$(20-40), 64-69

Figure 41. Normalized Power Density Spectra for Run M IV 64-69

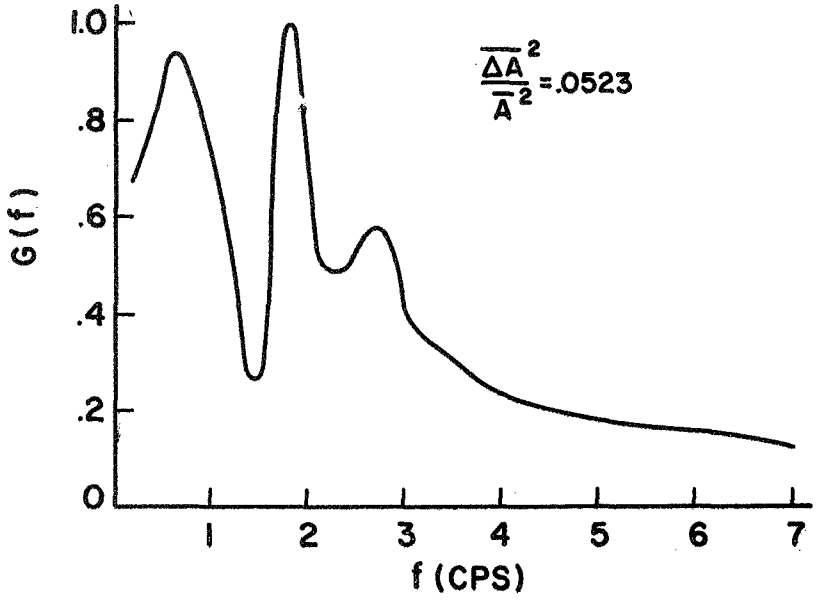


(a) AMP (20), 64.4 - 69.4

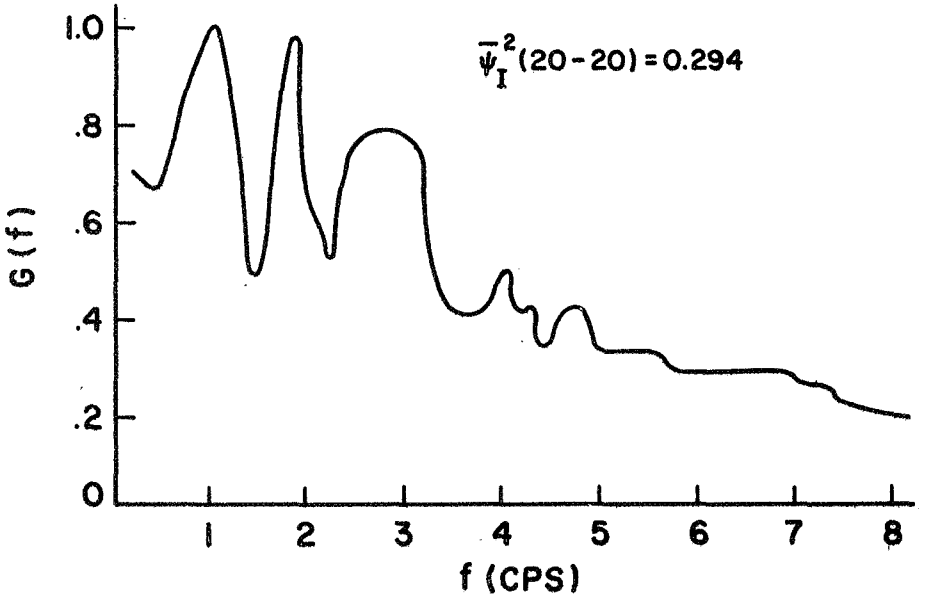


(b) PHASE $\psi$(20-20b), 64.4-69.4

Figure 42. Normalized Power Density Spectra for Run M IV 64.4 - 69.4

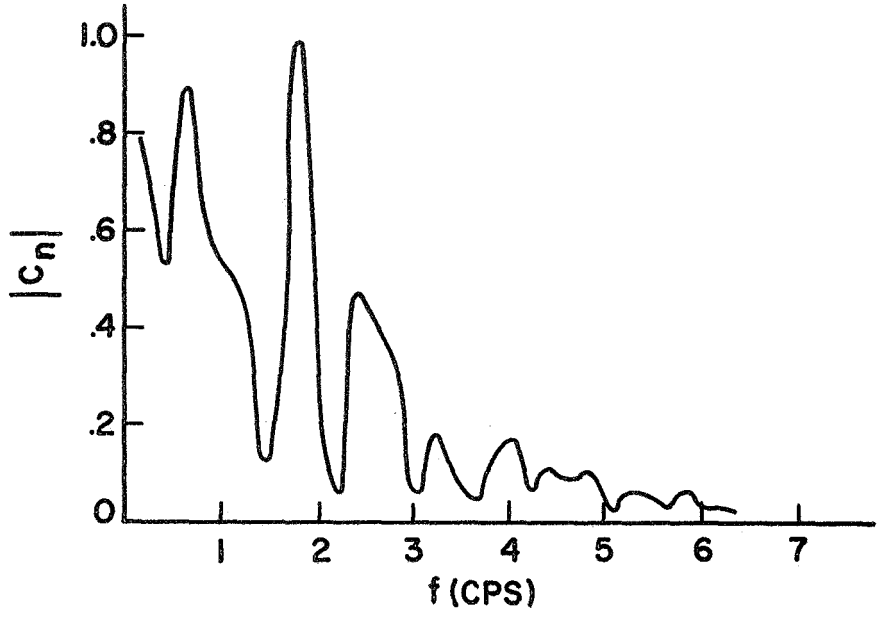


(a) AMP (20), 64-69

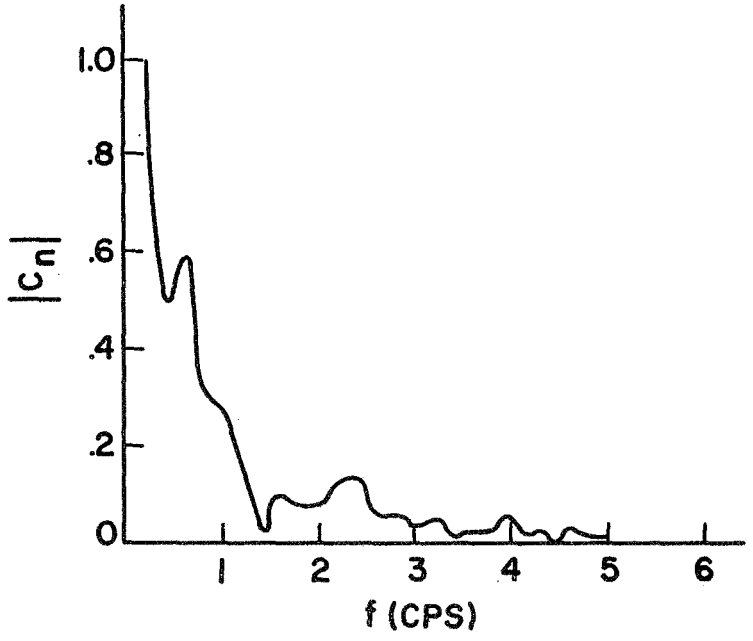


(b) PHASE $\psi$(20-40), 64-69

Figure 43. Normalized Amplitude Spectra for Run M IV 64-69

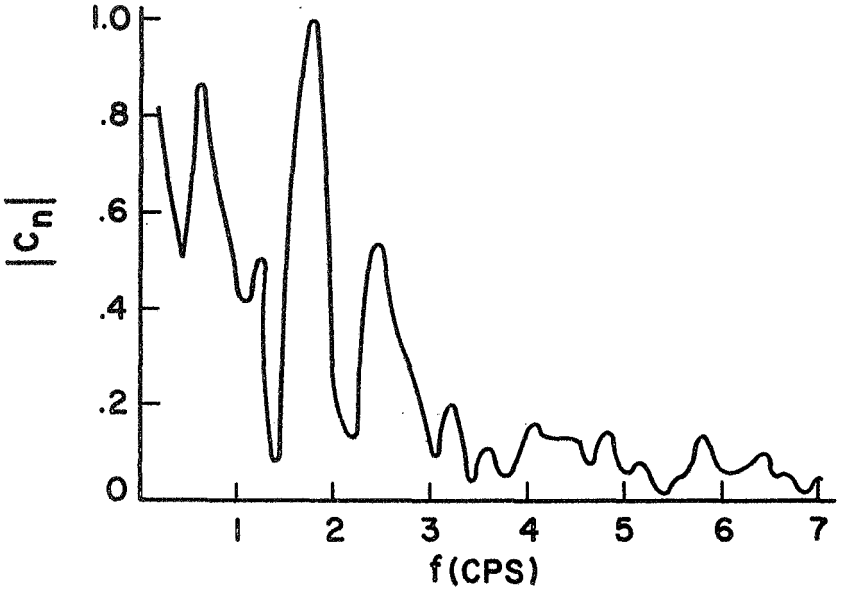


(a) AMP (20), 64.4 - 69.4

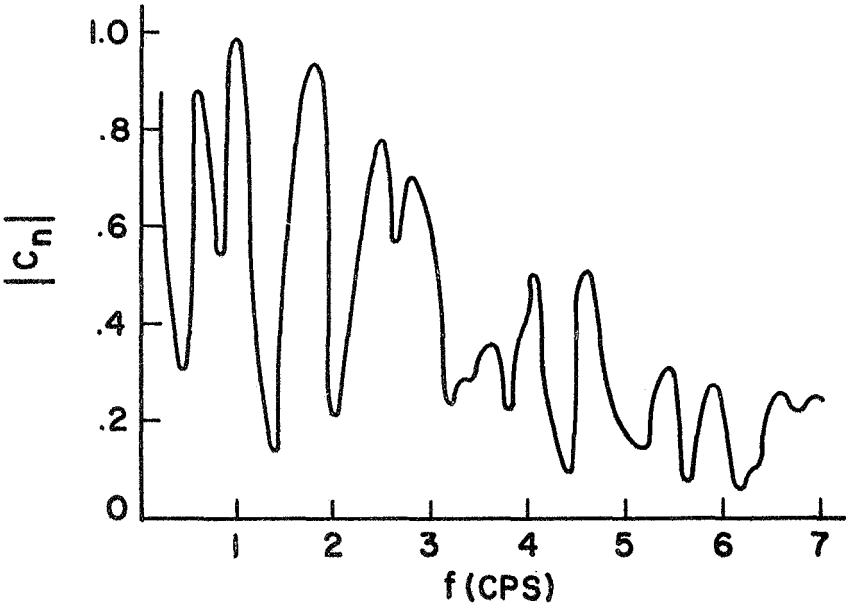


(b) PHASE $\psi$ (20-20b), 64.4-69.4

Figure 44. Normalized Amplitude Spectra for Run M IV 64.4 - 69.4

spatial frequency components. However, the amplitude spectrum and the $\psi(20\text{-}40)$ spectrum show that significant energy exists at only a few frequencies, which indicates that the total spectrum contains a few low frequency terms having significant energy, plus a randomized wide-band spectrum which has a lower amplitude. The program behavior is such that, if energy exists between the frequencies $Kf_0$ and $(K+1)f_0$, the energy will be divided between those two frequencies. No loss occurs when $Kf_0$ does not lie directly on the particular line of the spectrum. If the sampling duration is such that if periods are not complete at some frequencies, there will be an extra measure of energy at the lowest frequencies in the spectrum. If high frequency components exist which are not covered by the sampling rate, they will be reflected around the highest frequency represented. This is the aliasing error, which is not considered important except, perhaps, in the $\psi(20\text{-}20)$ spectrums.

In Figures 45 and 46 the normalized Fourier amplitude spectrums are shown for four simultaneous patterns; three are phase patterns and the other is an amplitude pattern. Here AP and CP are spectrums of the $\psi(20\text{-}40)$ patterns taken at the two ends of the baseline, while BP is that of the interferometer pattern. AA is the spectrum from the 20 mc pattern measured at the same end of the baseline where AP was measured. It is observed that all the phase patterns show some L.F. terms when comparison is made with the amplitude patterns. L.F. patterns do not develop as fast in amplitude as they do in phase. The interferometer pattern spectrum again shows relatively more energy at the higher frequencies when comparison is made with the $\psi(20\text{-}40)$ patterns.

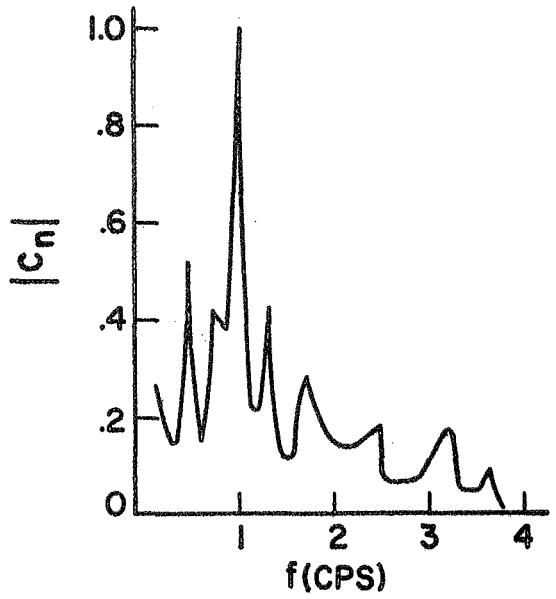


(a) AMP (20)

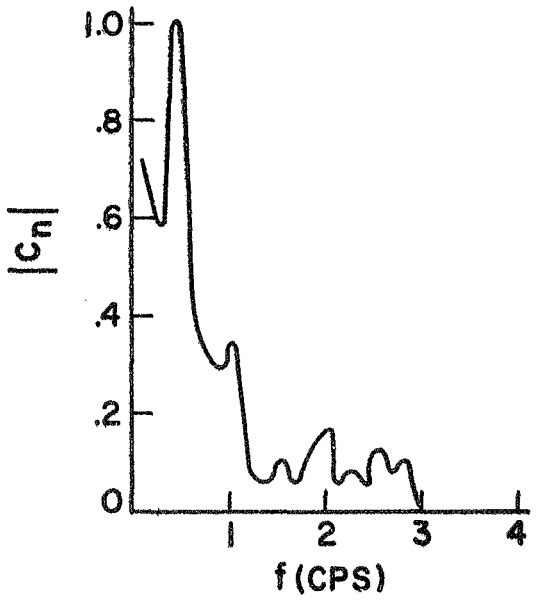


(b) PHASE $\psi$(20-40)
SOUTH END OF
BASE LINE

Figure 45. Normalized Phase and Amplitude Spectra Obtained from Simultaneous Records

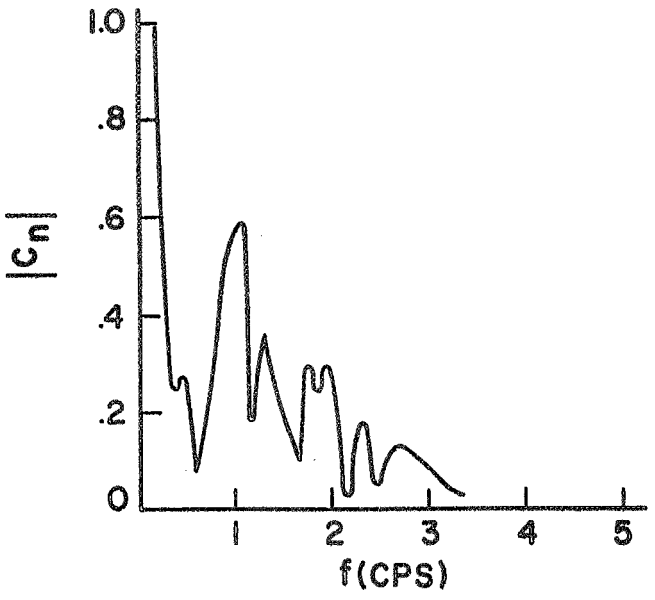


(a) PHASE $\psi_I$(20-20b)
INTERFEROMETER ACROSS
BASE LINE

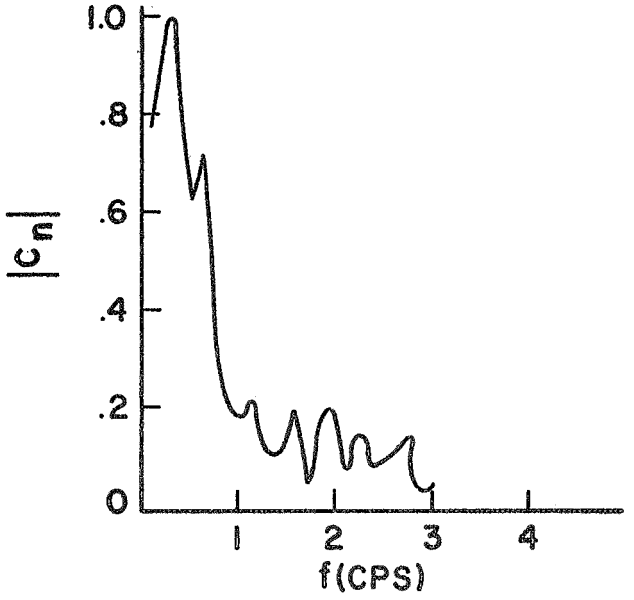


(b) PHASE $\psi$(20-40)
NORTH END OF
BASE LINE

Figure 46. Normalized Phase Spectra Obtained from Simultaneous Records

In Figures 47 and 48, all the spectra came from amplitude patterns; a 20 MHz and a 40 MHz pattern were measured at each end of the baseline. For this data sample, differences in patterns across the baseline are not as significant as differences in patterns between the frequencies measured at the same point. Also, the 40 MHz patterns show relatively more energy at the higher spectral frequencies. The theory of Chapter 2 shows how the patterns of the smaller scales develop faster. Thus, it is possible for the higher frequency terms to be more important at 40 MHz than at 20 MHz. It is noted that all of these spectrums are about 4.5 Hz wide if the bandwidth is defined as the frequency extent at which the amplitude falls off to 10 percent of maximum. The main differences in the spectra are in the distribution over this bandwidth.

## 4.2 Obtaining the Fourier Spectra at the Screen

The Fourier spectra which were discussed in Section 4.1 are those which represent the phase and amplitude diffraction patterns observed at the receiving stations. It has been assumed that the patterns have the same origin and each term in the angular spectrum is produced by a corresponding spatial frequency in the phase-modulating screen. This is equivalent to assuming that the screen is sufficiently weakly modulating that harmonic components in the angular spectrum (which can correspond to apparently amplitude modulating spatial periodicites) are not significantly large. Thus, if the patterns are transferred back to the screen using the appropriate propagation functions, each pattern should yield essentially the same function for representing the screen.

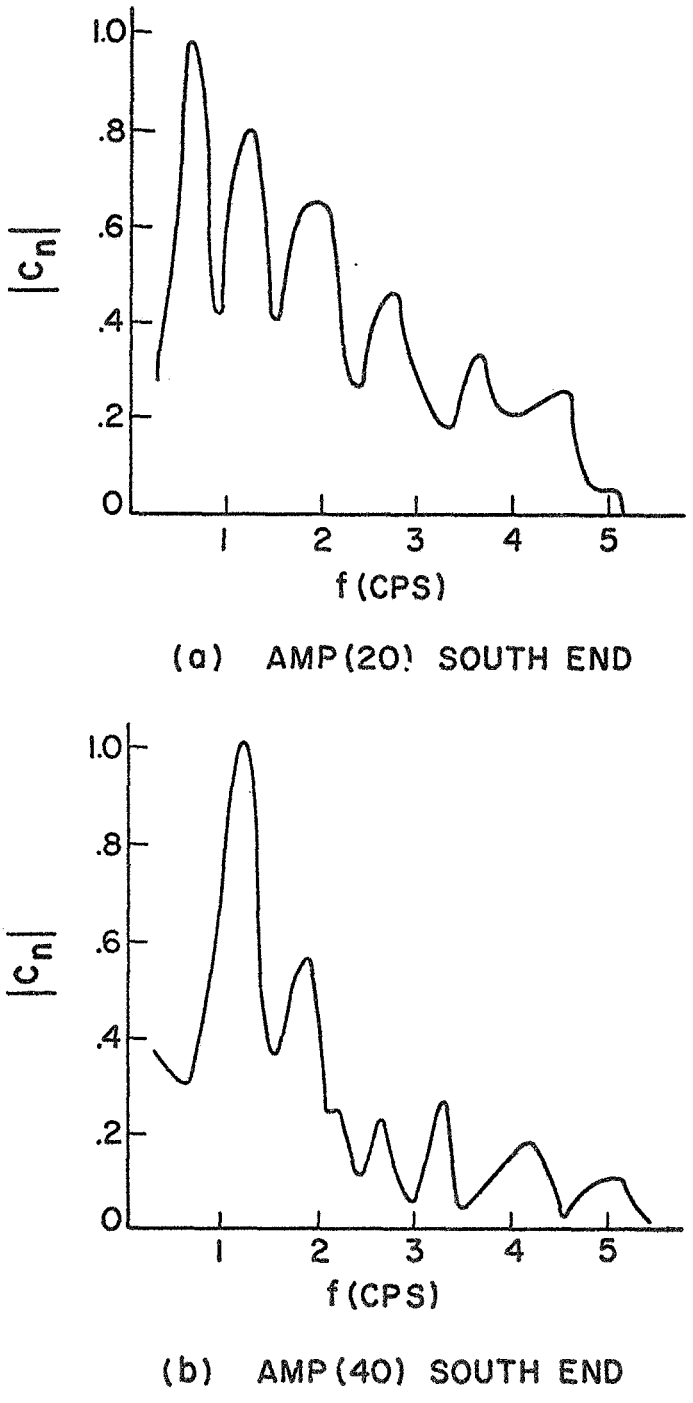


Figure 47. Normalized Amplitude Spectra Obtained from Simultaneous Records

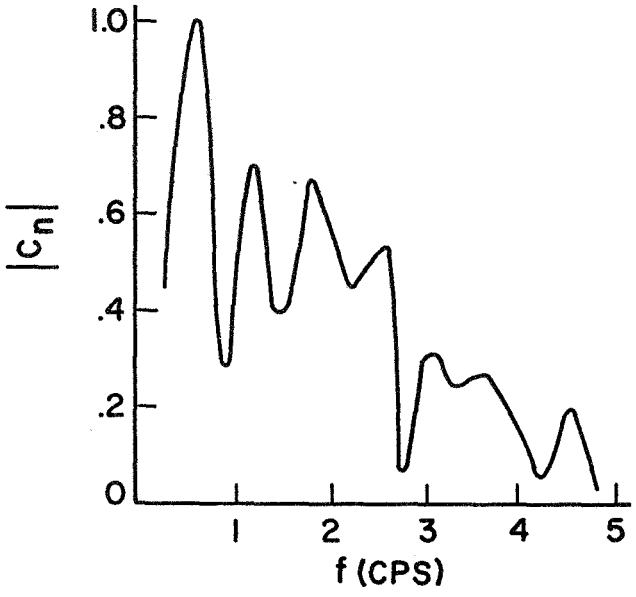


(a) AMP(20) NORTH END

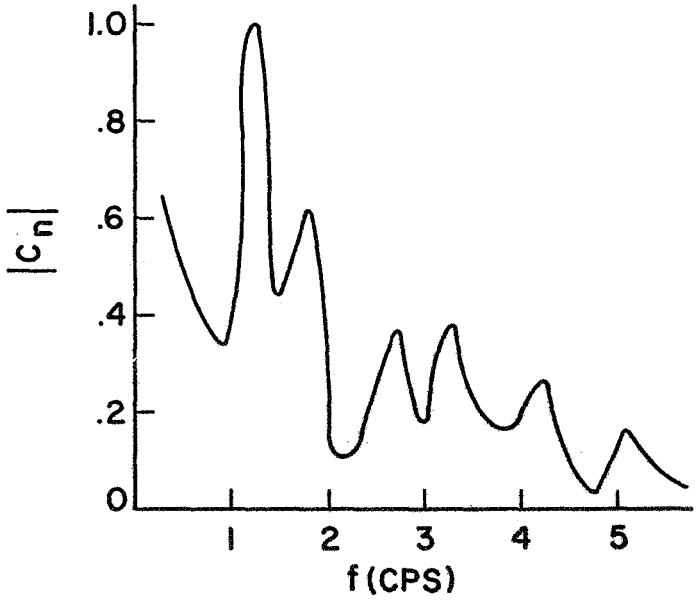


(b) AMP(40) NORTH END

Figure 48. Normalized Amplitude Spectra Obtained from Simultaneous Records

These similar screens would then have the same Fourier spectra. The closeness with which the transferred spectra correspond was investigated using a computer program which searches for a minimum variation in a least-squares sense.

The computer program accepted, as input arrays, the normalized Fourier spectra of two diffraction patterns which were measured simultaneously at one location. These could be a 20 MHz amplitude pattern and a 40 MHz amplitude pattern or one of the two amplitude patterns and the differential phase pattern between the 20 MHz and 40 MHz signals. Each term in the normalized array was then divided through by its propagation function. Thus, the coefficients $C(I)$ at the screen became:

For the 20 MHz amplitude array--

$$C(I) = A2(I)/\sin(I^2\Theta) \tag{4-9}$$

where $A2(I)$ is the normalized value of the Ith harmonic of the observed diffraction pattern for the 20 MHz signals, and $\Theta$ is the independent parameter which expresses the distance from the screen to the point where the pattern was measured.

For the 40 MHz amplitude array--

$$C(I) = A4(I)/\sin\left(\frac{I^2\Theta}{2}\right) \tag{4-10}$$

where $A4(I)$ is the normalized value of the Ith harmonic of the observed diffraction pattern for the 40 MHz signals.

For the 20-40 MHz differential phase array--

$$C(I) = B24(I) / \left[\cos\ I^2\theta - \frac{1}{2}\cos\ \frac{I^2\theta}{2}\right] \qquad (4\text{-}11)$$

where B24(I) is the normalized value of the Ith harmonic of the observed diffraction pattern on the phase between the 20 and 40 MHz signals.

In the simulations, any two of the above expressions for which data was available could be used. Implicit in expressions 4-9 to 4-11 is the assumption that each harmonic propagates as a function of a single scale size. This assumption is justified in Section 5.2.4. To prevent large values of C(I) from occurring when the denominators of the above expressions became small, denominators having values less than 0.1 were replaced by 0.1. For the first runs, using two arrays, the value of $\theta$ was stepped in increments of 0.5 degrees and continuing to 25.0 degrees; this range in $\theta$ was found to position the screen at all heights of interest within the ionosphere. The index I was varied from 1 to 15 or 1 to 20 depending on the input spectrum. For every value of $\theta$, the C(I) were obtained for each of the two input arrays and then were normalized to the largest member in their array. The sum of the squares of the differences of the members of the normalized transferred arrays having the same value of I was then found using the function:

$$S(\theta) = \sum_{I=1}^{N} \left[\left|C_{1\theta}(I)\right| - \left|C_{2\theta}(I)\right|\right]^2 \qquad (4\text{-}12)$$

The sums, $S(\theta)$, were stored for all $\theta$ and then sorted for their minima. The value of $\theta$ which produced this minimum was than used in the appropriate pair from 4-9, 4-10, and 4-11 to obtain the normalized spectra which represented the screen. To assure that an absolute minima was obtained, those regions in $S(\theta)$ were nulls had been observed were recrossed as $\theta$ was varied in steps of 0.05 degrees.

For the first harmonic (I=1), it was illustrated in Chapter 2 that $L_1$ is related to $\overline{FZ}$ through $\theta$:

$$L_1 = \left(\frac{2\pi\lambda\overline{FZ}}{\theta}\right)^{1/2} \tag{4-13}$$

Thus when the value of $\theta$, in radians, which minimizes 4-9, is inserted in 4-13, $L_1$ becomes a function of $\overline{FZ}$. The zenith angle and satellite height of the data sample may be used with the figures of Section 2.7 to obtain a plot of $L_1$ versus $h_I$, the screen height.

The frequency of the first harmonic in the spectrum, $f_0$, obtained by processing the records with the methods described in Section 4.1, was used to obtain another relationship between $L_1$ and $h_I$. First $L_1$ was expressed as a function of $\overline{F}$.

$$L_1 = V_S(1 - \overline{F})/f_0 \tag{4-14}$$

The satellite velocity, $V_S$ and the quantity $\overline{F}$ are known for each track. Since each value of $\overline{F}$ corresponds to a particular screen height, $h_I$, for the particular satellite height and elevation angle of the data sample, a plot of $L_1$ versus $h_I$ was obtained. An example

of these two curves and their single crossing is shown in Figure 49; this is one of the eight cases represented in Table 4. The crossing point yields two values of interest--the scale size of the first harmonic and the height of the screen.

Once the scale size of the first harmonic is determined, a scale size for each term in the spectrum may be obtained. A plot of normalized amplitude of the spectrum at the screen versus scale size is given in Figure 50. The 60 points used to obtain this composite figure came from the results of eight simulations for obtaining Fourier spectra at the screen.

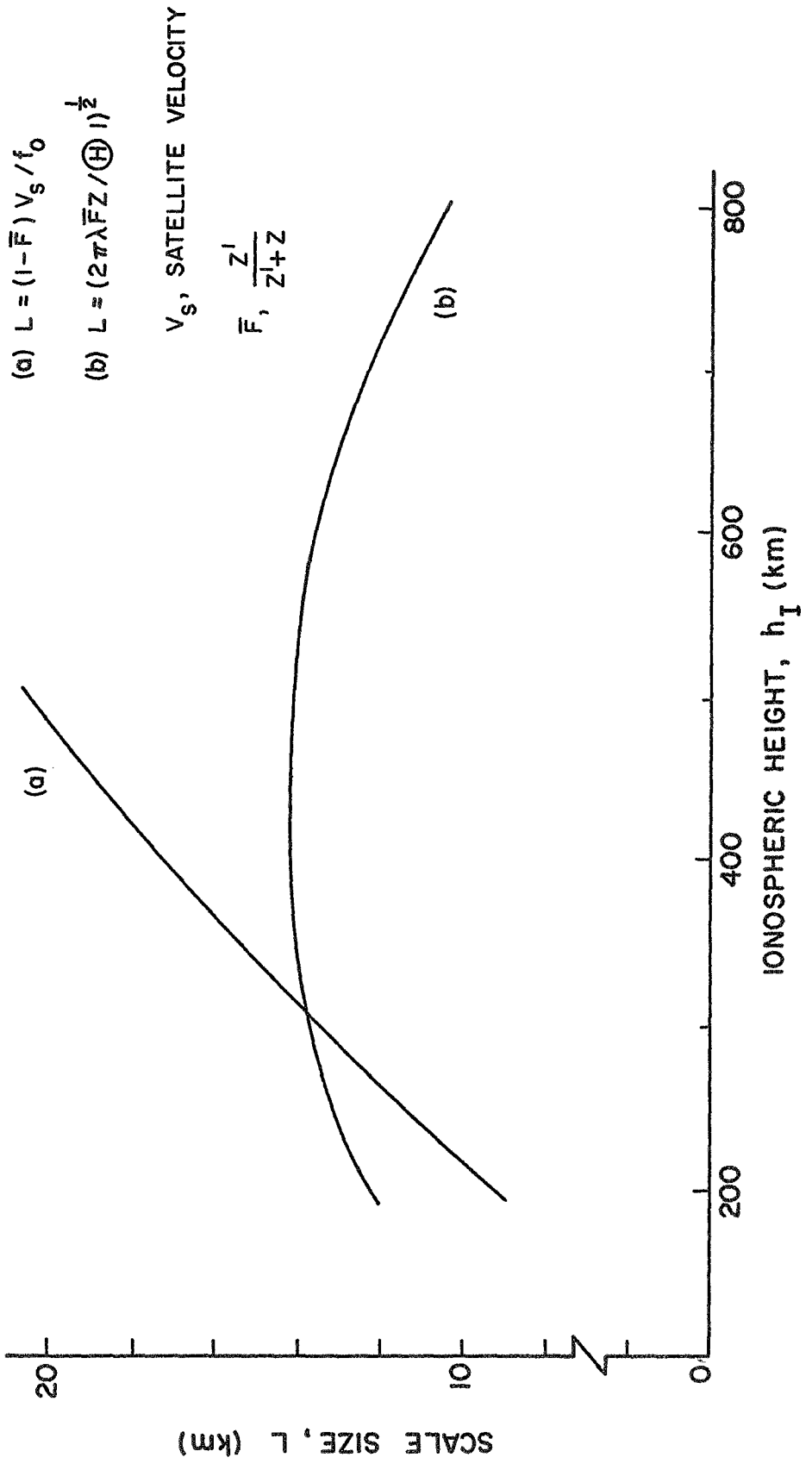


Figure 49. Two Curves that Represent L as a Function of $h_I$

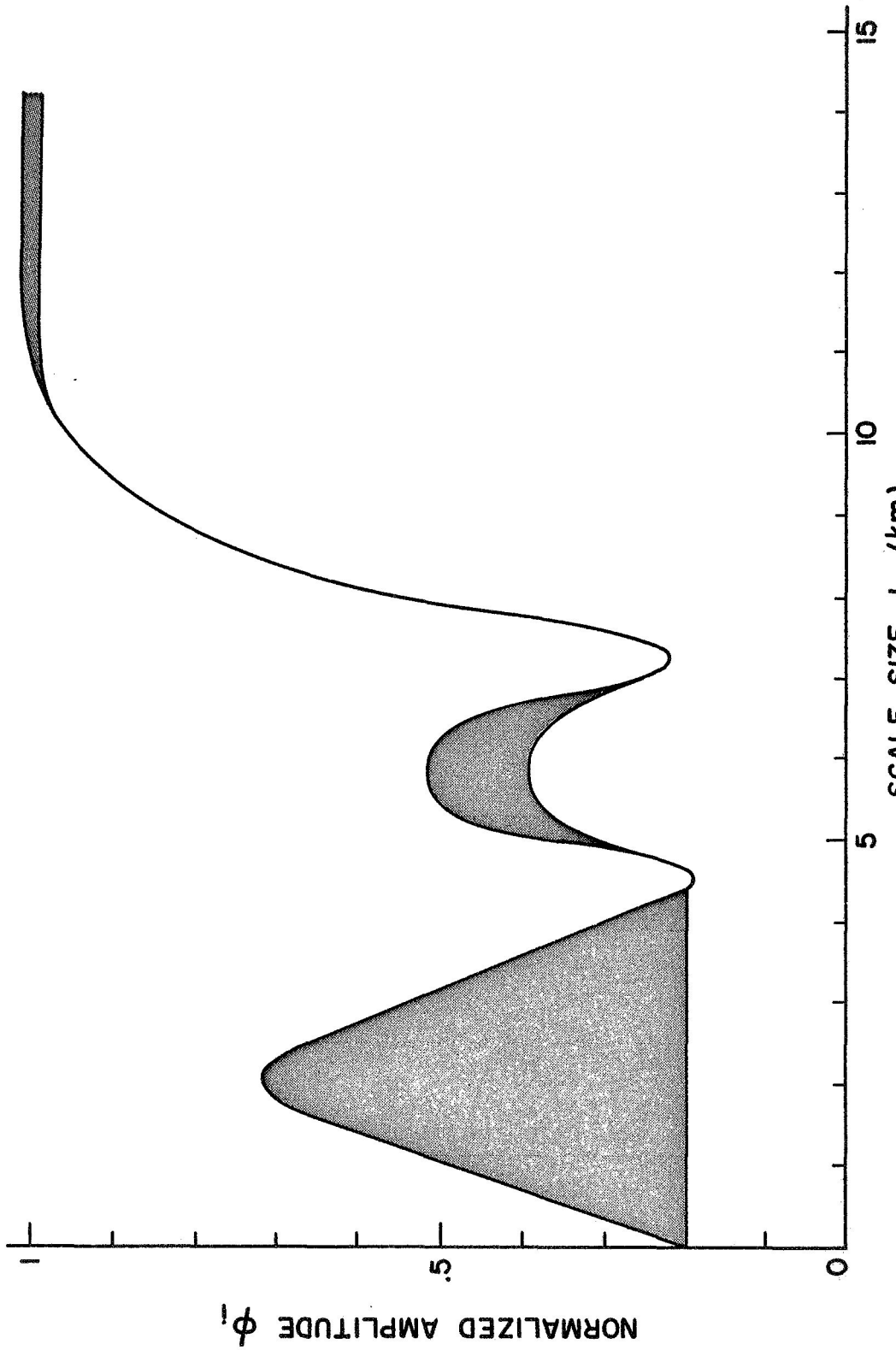


Figure 50. A Plot of Normalized Fourier Coefficients at Screen Versus Their Corresponding Scale Size

# CHAPTER 5 RESULTS AND CONCLUSIONS

The initial discussion in this chapter consists of a comparison of the phase and amplitude patterns which develop behind the various screen models presented in Chapter 2; both the similarities and differences in the patterns are noted. Because it has been assumed that each harmonic in the spectra has an associated weak modulation, the principle of superposition is evoked to assemble a composite ionospheric phase-modulating screen that will produce the particular patterns which were measured at the receiving stations. The Fourier spectra, for representing the screens obtained by transferring the spectra of the measured patterns back to the altitude which minimizes their differences, are shown to possess the characteristics of the composite screens.

The results obtained in this study are compared with those of other investigators. A final section contains suggestions for future work.

## 5.1 A Comparison of Phase and Amplitude Patterns and Their Spectra

When the diffraction patterns which develop behind the theoretical screens of Chapter 2 are examined, both similarities and differences are observed. For those screens consisting of more than a single modulating frequency, both the phase and amplitude patterns change with distance behind the screen. Each component of the Fourier series which represents the screen propagates as a different function of distance from the screen. Therefore, the correlation functions of these patterns also depend on, and change with, the distance from the screen.

The variation of the magnitude of a single component of three of the diffraction patterns measured for this investigation are shown in Figure 18 as a function of distance behind a thin screen. These curves illustrate that, although it is possible for the same harmonic in the two amplitude patterns to vanish at the same distance from the screen, there is no distance that will cause the simultaneous disappearance of the same harmonic in either of the two amplitude patterns and the phase difference patttern. Thus the absence of a particular harmonic in the two patterns indicates that it was not present in the phase-modulating screen. If phase and amplitude patterns are both measured on the same transmitted frequency, it is possible for one to be quite evident while the other is absent; this was noted by DeBarber (1962)[15], who used a short 0.152 km baseline for measuring the phase fluctuations on 54 MHz signals.

Comparison of the measured phase and amplitude patterns reveals that the phase patterns usually contained more relative energy in their low frequency components. This in part is due to the pattern propagation functions which reduce the amplitude components considerably more when $2\pi\bar{F}Z/L$ is small. Also, when the screen is neither single frequency nor weak, the cross products inherent in the rectification operations, which yield amplitudes, lead to more energy in the higher frequency components.

In this investigation amplitude patterns were measured on both 20 and 40 MHz signals. The thoretical work of Chapter 2 reveals that if $\pi\bar{F}\lambda/L^2$ is greater than $\pi$ for $\lambda$ being that of the 20 MHz signal,

then the 40 MHz amplitude pattern will be shifted so that the nulls in the patterns will not be coincident. This shift was not observed in the measured patterns.

When two-dimensional screens are considered, the observed patterns become a function of the direction in which the screen is traversed. When the anomalies are not elongated in a direction normal to the direction of travel, the amplitude patterns develop in one-half the distance for the same scale sizes. Each complexity added to the screen model increases the number of significant Fourier terms required to properly represent the screen and the diffraction patterns that result behind it. The fact that all of the observed diffraction patterns could be represented by a few significant Fourier terms shows that these patterns originated from a relatively simple screen.

Although most of the phase diffraction patterns examined in this study were the differential phase patterns that exist between two frequencies received at the same point, some phase differences across a baseline were used. It has been shown, in this case, if the antenna spacing is the baseline length, $b$, then this interferometer is in effect a spatial filter with a pass band whose function is $2 \sin \frac{\pi b \overline{F}^2}{L}$. A baseline having a length of one kilometer or less will attenuate those spatial frequencies which originate from the larger anomalies. This filter effect accounts for the differences observed in the phase patterns measured across the baseline.

It was shown in Chapter 2 that the single frequency, one-dimensional screen is the most effective for producing deep nulls in the amplitude pattern for a given peak phase modulation, $\phi_0$ . When the screen becomes two-dimensional and thick, with the same value of $\phi_0$ , not only is the average modulation intensity across the screen reduced but the phasing of the several diffracted components is such that fewer nulls are produced. Because the most efficient screen produces deep notches for $\phi_0$ of 0.8 radian or greater, the regular occurrence of deep notches behind a two-dimensional screen of finite thickness indicates that the screen has a peak modulation of more than one radian. This has been observed for most of the records processed.

## 5.2 Ionospheric Screen Requirements for Producing the Observed Diffraction Patterns

In this section the characteristics of the diffraction patterns which developed behind the theoretical screens of Chapter 2 are used to specify some of the parameters of a real ionospheric screen. The criterion used is that the specified screens produce, when the geometric relationships of Section 2.7 are considered, the phase and amplitude patterns which have been recorded and analyzed.

### 5.2.1 The Magnitude of the Peak Phase Modulation

Using the scintillation index, S , as a measure, the peak phase modulation at the screen is found to be slightly larger than one radian for the samples that were processed. The scintillation index has been

used in previous studies[18] to indicate the magnitude of the fluctuations on received radio frequency signals. The recorded amplitudes are scaled by using the relationship:

$$S = \frac{\text{Max signal - Min signal}}{\text{Max Signal + Min signal}} \qquad (5\text{-}1)$$

As the fluctuation level is to be determined over the sample duration, for consistency in reduction of records, the third peak down is used for the maximum signal and the third null up for the minimum signal; the sample period should contain at least ten changes from maximum to minimum. When all the simulation runs made for Chapter 2, where the peak phase modulation was one radian, were considered, the voltage scintillation index, $S_V$, of the resulting amplitude patterns varied from 0.31 to 0.84. The mean value of $S_V$ for the simulations was 0.46 with one-fourth of the values being above 0.72. This leads to the conclusion that the peak phase modulation at the screen was greater than one radian. This was not revealed in any of the previous studies where the efficient one-dimensional cosine screen of Hewish (1952)[4] was used as a model for determining the intensity of the phase modulation. It was shown in Chapter 2 that the two-dimensional screen having finite thickness is less efficient in generating peaks and nulls. This inefficiency combines with the strong dependence of the patterns on the distance from the screen to reduce the scintillation index of the observed patterns.

Another parameter of interest for indicating the intensity of the amplitude scintillations is the ratio of a.c. to d.c. powers. This

is expressed by 2-77. By plotting $S_V$ against the power ratio, RA , a linear relationship was found to exist for these two quantities.

$$S_V = 0.3 + 2.\ RA \tag{5-2}$$

The average value of RA taken over all the amplitude diffraction patterns processed was 0.11; the fluctuating signal power was slightly greater than 10 percent of the average signal power. When the theoretical diffraction patterns of Chapter 2 were analyzed, the scintillation index and RA were shown to be strong functions of the scale size and the distance from the screen. This indicates that these quantities, when obtained from a single diffraction pattern record, are not sufficient for determining the phase-modulating intensity of the screen.

5.2.2 The Scale Size of the Irregularities

This investigation has determined that the scale sizes obtained for irregularities during processing of the diffraction pattern records depend on the particular patterns measured and the definition of the term "scale size." Using the geometrical relationships of Section 2.7, with the major components in the Fourier coefficient spectra for the amplitude patterns measured, results in scale size variations of from 0.63 km to 10. km with a mean value of 2.16 km. If the same procedures are used with the major components in the Fourier spectra of the differential phase patterns, $\psi(20\text{-}40)$ , which were measured between two frequencies at the same location, the scale size is found to vary from 2 to 17 km with the mean value being 7 km. When the interferometer

records, $\psi(20\text{-}20b)$ , taken across the 1.0 km baseline are used in the same analysis, the scale sizes obtained vary from 0.7 km to 5.8 km, with a mean value of 1.8 km.

The methods of Section 4.2 transferred patterns back to the height of the screen where the scale sizes were determined. In some instances, only amplitude patterns were used; in others, differential phase and amplitude patterns were used together. Figure 50, which is a plot of normalized amplitude of components at the screen versus scale size, shows peaks in amplitude at 2, 6, and 12 km. This is in good agreement with the scale sizes obtained by use of the individual patterns. The presence of large scale sizes are not usually evident in the amplitude patterns; it is possible for them to appear when the anomalies are elongated or due to the beats of two or more smaller scale sizes.

Most of the work previously performed to investigate diffraction patterns has been based on analysis of amplitude patterns alone. Also, in most cases the determination of scale size has assumed that the scale size of the pattern was similar to that of the screen; then a measure of correlation distance was used to estimate the scale size. To permit comparison of the findings of this investigation with those of other studies, the method of Aarons and Guidice (1966)[19] is used to demonstrate the relationship between scale size and correlation distance. That investigation used an irregularity scale size, $L_F$ (F for Fourier), defined by Lawrence et al (1964)[20] as the reciprocal of the wave number of the dominant terms in the Fourier analysis of the

irregularity distributions. It is $2\pi$ times greater than the autocorrelation distance, $L_c$ (c for correlation) for a single frequency screen. If this relationship is used to find $L_c$ for the diffraction patterns measured and analyzed for this investigation, then a mean $L_c$ is obtained of 0.34 km for the amplitude patterns, 1.11 km for the differential phase patterns, and 0.29 km for the phase patterns measured across the baseline. For investigations using autocorrelation functions and the assumption of a Gaussian distribution for the phase modulation[15], if the falloff to 0.606 is asserted to correspond to the correlation distance, then $L_F$ is 6.8 times greater than $L_c$.

Another important consideration for scale size determination is whether the radiating source is a satellite or a radio star. When tracks are made at low elevations, the geometry of satellite measurements reduces the value of $\overline{FZ}$ to about one half of $Z$; the amplitude patterns produced by the larger scale sizes do not have distance in which to develop. For this reason, those investigations which used radio stars at elevation angles not near the zenith should obtain larger values for $L_F$. This held true for Hewish (1952)[4], who found $L_F$ to be 3 to 7 km, and Aarons and Guidice (1966)[19], who obtained 7 km for $L_F$. These values correspond closely to those obtained in this investigation where the phase difference patterns, $\psi(20\text{-}40)$, were analyzed.

Having examined and analyzed the several types of diffraction patterns measured, it was concluded that the phase-modulating screens contain scale sizes from less than 1 km to greater than 15 km. The low

frequency terms which result from the large scale sizes contain the most phase modulation but are not much in evidence when amplitude or baseline interferometer patterns are measured. Superimposed on this structure of scale sizes, which results in a small number of Fourier terms for the spectra, is a certain amount of randomness which derives from a larger number of small scale size irregularities.

It is worth noting here how dissimilar the spectra obtained for representing the screens are when compared with the spectra of time functions from more random phenomena. The spectra for the screens have, on the average, 7.6 harmonics in the first 15 spectra with normalized amplitudes larger than 0.2; the bandwidth was 51 percent achieved for this threshold. In each case, the first harmonic was the largest element. When a number of samples of the radar amplitude function from 20 randomly spinning metallic reflectors, plus a steady component, were analyzed, they were found to produce 13 harmonics in the first 15 of their Fourier spectra with normalized amplitudes greater than 0.2; the bandwidth was 87 percent achieved. Also, the position of the harmonic in the normalized spectra which had the maximum amplitude varied from the first to the fourteenth with the average being the seventh harmonic. The Fourier series spectra which result when random phenomena are sampled are wide-band with the larger element taking any position in the bandwidth with equal probability. The spectra obtained for representing this spatial modulation across the ionospheric screens were narrow band and ordered such that the first harmonic was the largest.

5.2.3 The Height Distribution of the Anomalies

All past investigations of F-region anomalies appear to agree that the screen height should lie between the altitudes of 250 and 600 km. The values for height obtained by use of various methods did not show dependence on the frequency transmitted, the patterns used, or the method used. There is reason for not obtaining a precise height determination through examination of the patterns. For example, in this study when the satellite was near zenith at a height of 1,000 km, the $\overline{F}Z$ term, which is the variable in pattern propagation when scale size is a constant, increases by only 28 percent as the ionospheric height is increased from 250 to 600 km. The effect is even less at larger zenith angles. If anomalies have scale sizes which produce maximum intensity amplitude patterns when they are positioned at an altitude of 600 km, they will produce 0.90 of this amplitude when they are positioned at 250 km. Lowering the satellite height will produce a larger variation of the patterns as the scale size is moved through the ionosphere; it also will reduce the contributions of all large scale sizes.

Two methods were used in this study to obtain the height of the ionospheric phase-modulating screens. First it was observed in Chapter 2 that, when $\Theta(\Theta = 2\pi\lambda\overline{F}Z/L^2)$ is larger than $\pi$ for the 20 MHz transmission, the nulls in the 20 MHz and the 40 MHz amplitude patterns would not occur at the same time. In the measured patterns the nulls occurred together; thus $\Theta$ must be assumed to be less than $\pi$. If the mean value for $L_i$, obtained for the cases when simultaneous

amplitude patterns were measured, 2.55 km is inserted in the expression for $\theta \leq \pi$, and Figures 15 through 17 of Section 2.7 are used, it is found that the ionospheric height, $h_I$, for the screen varies from 250 km to less than 400 km.

The second method for height determination, discussed in Section 4.2, involves transferring the measured spectra back to a height which minimizes their differences when the appropriate propagation factors are used. This method resulted in a height variation for the screens of from 250 to 390 km, with the mean value of 300 km (see Table 4). It was concluded that the screen heights vary from 250 to about 400 km with the mean value near 300 km. These values are in general less than those obtained by DeBarber (1962)[15] from 330 to 540 km but in good agreement with those given by Yerkhimore (1962)[21]--270 to 350 km.

The position of the observed anomalies with respect to the height of maximum ionization, and the excess ionization of the large anomalies, corresponds to the predictions of the theory of Martyn (1959)[29]. However, patches of excess ionization in the same position and time frame could be obtained using other theories for irregularity formation.

### 5.2.4 The Composite Screen

The conclusions of Sections 5.2.1 through 5.2.3 are combined to specify phase-modulating screens which agree with the theory of Chapter 2 and which are capable of producing phase and amplitude diffraction patterns similar to those measured. The mean height of the ionospheric screen will vary from 250 to 400 km, with the most likely value being

Table 4

Height of the Irregularities

| Run No. | Type of Spectra | Height (km) |
|---|---|---|
| 1 | Amp-Amp | 280 |
| 2 | Amp-Amp | 390 |
| 3 | Amp-Amp | 300 |
| 4 | Amp-Phase | 325 |
| 5 | Amp-Phase | 310 |
| 6 | Amp-Phase | 250 |
| 7 | Amp-Phase | 295 |
| 8 | Amp-Phase | 265 |

about 300 km. Because the dominant terms in the patterns change only sightly for small variations in screen height, the screen thickness is difficult to determine. The calculations described in Section 4.2 indicate that the screen thickness should be less than 100 km.

The total peak phase modulation in most cases is greater than one radian, which is divided among scale sizes ranging from 15 km down to 1 km. This upper limit on scale size is determined by the sample length. The structure of the screen is such that smaller blobs are superimposed on or imbedded in the larger blobs. The large blobs produce the greatest variation in phase; the variances of the $\psi(20\text{-}40)$ differential phase patterns were ten times as large as those for the $\psi(20\text{-}20b)$ interferometer phase patterns across the baseline. It is interesting to note that the scale sizes between 4 to 8 km have less phase modulation than did those which were larger or smaller. The weak modulation associated with the small scale sizes prevents large scattering angles, which validates the assumptions of Section 2.7.1, whereby the region of the screen which can contribute to the pattern at a point is no more than a scale size in extent. The larger scale sizes have not been observed in investigations where the amplitude patterns alone were used. This is particularly true where satellites were used as radiation sources. The theory of Chapter 2 shows that when the anomalies are elongated the small scale size controls the propagation factor for the pattern, while the direction of travel of the satellite across the screen controls the scale size observed. Because the larger scale sizes were for the most part not seen in the amplitude patterns,

the anomalies appeared not to be elongated; this was the conclusions of Titheridge (1966)[22]. However, the records were all taken when the satellite was to the north of the receiving stations where the magnetic field geometry is such that this direction of travel of the satellite is nearly across the small (transverse) axis of the anomalies. For this reason, the presence of elongated anomalies would not be detected. Because of this particular ray path magnetic field geometry, the procedure of Section 4.2, which assumes that each harmonic in the pattern propagated as a function of a single scale size, are justified.

The larger blobs comprising the bulk of the modulation could result from a number of smaller blobs which merged by diffusion but which retained some of the small scale characteristics in their electron density gradients. This postulated configuration acquires credence by virtue of the fact that patches of scintillation have been noted[8], and large scale anomalies have been observed to drift while retaining their identity. Stewart and Thitheridge (1966)[24] observed patches with horizontal dimensions from 75 to 520 km. Large scale irregularities also were studied by Chisholm (1961)[24] who gave 38 km to 117 km as their horizontal dimensions. Since the configurations of anomalies are not truly symmetrical, they produce diffraction patterns which contain a measure of random variation in addition to the finite number of Fourier terms representing the bulk of the modulation. This random variation is represented by a larger number of small amplitude Fourier terms. When the pattern produced by the screen is sampled for longer times, the resulting Fourier spectra contain a larger contribution due

to the randomness in the size and spacing of the anomalies. This situation is more likely to occur when radio stars are used as a radiating source. In this study, the sampling techniques were selected to avoid magnifying the apparent randomness of the screens. This was accomplished by sampling over a time consisting of one or more complete periods of record fluctuation.

## 5.3. Comparison With Previous Investigations

Previous investigations used Fourier analysis to determine the scale size of the ionospheric irregularities. Gruber (1961)[25] used the radio star Cygnus A and tracked on frequencies of 50 and 200 MHz. In that investigation, measurements were made across the baseline or 400 meters in length. The phase differences and the sum of the amplitude fluctuations were used for records, and during processing, the autocorrelation function and power density spectra were determined. The usual assumptions were used of the scattering being a random process and the one-to-one relationship between the spatial autocorrelation function of the phase-modulating screen and the fluctuations observed at the ground. The investigation determined the spectra for phase and amplitude to be somewhat similar although the spectra were not a continuum but consisted of discrete frequency components. The analysis of Chapter 2 shows that the short baseline used would filter out the larger scale sizes in the phase pattern. Although the data-handling procedure is one which tends to smooth the spectra, it does not suppress the discrete harmonic components.

An investigation by Lansinger (1966)[26] also used the radio star Cygnus A. Both phase and amplitude spectra were obtained using the autocorrelation functions and power density approach; they were found to be somewhat different even though the durations of the data samples were from 1.5 to 2.0 hours. At times, the statistics for the amplitude and angular scintillations showed dependence; this is possible since the statistics are not time functions. This condition suggested that the ionospheric screen model consisted of non-random ionizations which produced an ordered structure in the ground diffraction patterns. As the only screen motions are due to Earth's rotation and ionospheric drifts, the important frequency components in the spectra have frequencies which are an order of magnitude smaller than those resulting from satellite tracks. The continuous alterations in size and electron density of the individual anomalies give them a more random appearance; if the patterns are somewhat ordered for radio star tracks they should be even more ordered for satellite tracks.

Another investigation using power spectra, made by Jesperson and Kamas (1964)[27], used the scintillation on satellite signals of 54 and 150 MHz, and again found that the spectra are composed primarily of several discrete components and that on no occasion was there a continuous distribution of frequencies. The upper frequencies were all less than 3 Hz. This investigation, which uses the frequencies of 20 and 40 MHz and both phase and amplitude diffraction patterns confirms the observations of Jesperson and Kamas. For the theory of Chapter 2 and the data processing procedure of Chapter 4, both investigations

indicate that: (1) the spectra consist of a few important components, and (2) amplitude patterns on two different transmitted frequencies, measured simultaneously at the same location, will not have the same ordering of their important components. In addition, the phase patterns may contain other quite significant terms.

Another scintillation study which warrants note is that of Allen, Aarons and Whitney (1964)[28], which analyzed the amplitude diffraction patterns that developed on the transmissions from both radio stars Cygnua A and Cossiopeia A and satellites. When their measurements were compared with the random scattering anclysis of Briggs and Parkin (1963)[9], inconsistencies were revealed. First, the mean frequency dependence in the region between 30 and 63 MHz was less than inverse linear. (The geometrical developments of Section 2.7 show this could occur only in a particular range of the independent variable $\Theta$ .) Also, this study stated that it was not unusual for amplitude scintillation to decrease with decreasing frequency, even in the higher H. F. region, during intense storms. This would occur, as shown in Section 2.7, if the ratio $\overline{F}Z\lambda/L^2$ is approximately equal to 0.5 for the lowest frequency. Finally, the study concluded that multifrequency observations have shown that, when satellite beacon frequencies are used, it is usually not possible to find a direct correspondence between the shadow pattern on the ground and the irregularity pattern in the ionosphere. The theory of Chapter 2 shows that the only time a phase or amplitude diffraction pattern behind a screen is similar to the spatial distribution along the screen is when the screen can be represented by a single spatial frequency.

## 5.4 Suggestions for Further Work

The analysis involving the geometrical considerations in Chapter 2 showed that for an interferometer system the baseline length determined which of the screen scale sizes would be enhanced. A variable baseline system should be constructed such that a number of interferometer diffraction patterns could be generated for each satellite pass. These patterns then should be compared with the amplitude patterns measured at the same frequency. According to the theory of Chapter 2, the same spatial frequencies cannot be dominant in both the amplitude and phase patterns; however, for certain baseline lengths the spectra would be more similar.

Additional patterns to those treated in this study could be obtained from the same baseline. For example, $\psi(40\text{-}40)$ interferometer patterns as well as harmonic frequency, $\psi(20\text{-}40)$ interferometer patterns would be of interest. A short baseline could be used to collect data on the small random scatters during the same satellite pass when the other patterns are being used to evaluate the nature of the discrete anomalies. Similarly, a comparison of the 40 MHz and 20 MHz amplitude patterns could be made to determine if the latter is more random. Since a larger area of the screen contributes to this pattern, it should contain a greater measure of randomness.

It has been observed, as expected, that records obtained from radio star tracks show a larger scale size. If possible, it would be of interest to have radio star tracks for the same time and region of space over which satellite data is available. The amplitude patterns

of satellite signals increase with $\overline{FZ}$ while the radio star pattern gorws with $Z$ alone. Accordingly, the tracks of two different satellites would be useful. If one had a height of 400 km and the other had a height of 1,00 km, their diffraction patterns should be quite different. Also, a detailed examination could be made of the spectra from two amplitude patterns measured on frequencies separated by more than 20 and 40 MHz.

## 5.5 Conclusions

In conclusion, it is worth noting that the success of this investigation in answering a number of questions posed in previous studies is primarily due to limitation of restricting assumptions in formulation of the problem to be addressed. The intent of this investigation was to measure a number of diffraction patterns and then to match their spectra using the theoretical phase-modulating screens as models. A gaussian distribution was not used as a model for the irregular phase modulation; the anomalies were not put in the far field or within the first Fresnel zone. The assumptions were that: (1) the angular spectrum-electric field transforms could be used; (2) the scattering was sufficiently weak for the diffraction theory to hold and for the principle of superposition to be used; and (3) the region in the screen producing the modulation could be represented by a two-dimensional spatial Fourier series. The solution of the problem was thus kept as general as possible until the parameters which define the screens were to be determined. This non-restrictive

philosophy also was followed in selection of the methods for harmonic analysis; the computer programs and sampling techniques finally selected were those which gave the best spectral representation for the sample inputs used to test the programs.

BIBLIOGRAPHY


1. Booker, H.G. and Clemmow, A., Proc. Inst. Elec. Engrs., 97, III, 11, 1950.

2. Booker, H.G., Ratcliffe, J.A., and Shinn, D.H., Phil. Trans. Ray. Soc. A242, S29, 1950.

3. Hewish, A., Proc. Ray. Soc. 209, 81, 1951.

4. Hewish, A., Proc. Ray. Soc. 214, 494, 1952.

5. Bowhill, S.A., Jour. Atmosp. Terr. Phys. 20, 9, 1960.

6. Bowhill, S.A., Jour. Res. Natl. Bur. Stds. 65D, 275, 1961.

7. DeBarber, J.P. and Ross, W.J., AGARDO graph No. 95, "Spread F and its Effects on Radio Wave Propagation and Communications", 357, 1963.

8. Yea, K.D. and Swenson, Jr., G.W., Jour. Res. Natl. Bur. Standards, 68D, 867, 1964.

9. Briggs, B.H. and Parkin, I.A., Jour. Atmosph. Terr. Phys., 25, 339, 1963.

10. Booker, H.G., Proc. Inst. Radio Engrs., 46, 298, 1958.

11. Briggs, B.H., Radio Science, 1, 1163, 1966.

12. Sneddon, I.N., "Fourier Transforms", p. 112, New York McGraw-Hill Book Company, Inc., 1951.

13. Roger, R.S., Jour. Stmosph. Terr. Phys., 27, 335, 1965.

14. DeBarber, J.P., Sci. Report No. 151, Ionosphere Research Laboratory, The Pennsylvania State University, 1961.

15. DeBarber, J.P., Sci. Report No. 169, Ionosphere Research Laboratory, The Pennsylvania State University, 1962.

16. Evans, G.W. II, et al, Tech. Report No. 15, Stanford Research Institute, 1963.

17. Blackman, R.B. and Tukey, J.W., "The Measurement of Power Spectra", New York: Dover Publications, Inc., 1959.

18. Whitney, H.E. and Allen, R.S., "Notes on the Measurement and Comparison of Scintillation Index Values", Report of the Joint Satellite Studies Group, ed. by E. J. Vassey, Universite de Paris, 1966.

19. Aarons, J. and Guidice, D.A., J. Geophys. Res., 71, No. 8, 3277, 1966.

20. Lawrence, R.S., Little, C.G., and Chivers, H.J.A., Proc. IEE, 52, 4, 1964.

21. Yervkhimov, L.M., Geom. i Aeron., 2, 688 NASA Translation, 1962.

22. Titheridge, J.E., J. Geophys. Res., 68, 3399, 1963.

23. Stuart, C.F. and Titheridge, J.E., Jour. Atmosph. Terr. Phys., 28, 255, 1966.

24. Chisholm, G.E., Sci. Report No. 166, Ionosphere Research Laboratory, The Pennsylvania State University, 1962.

25. Gurber, S., Jour. Atmosph. Terr. Phys., 20, 59, 1961.

26. Lansinger, J.M., Radio Science, 1, 11/6, 1966.

27. Jespersen, J.L. and Kamas, G., Jour. Atmosph. Terr. Phys., 26, 457, 1964.

28. Allen, R.S., Aarons, J., and Whitney, H., IEEE Trans. on Mil. Electronics, 146, 1964.

29. Martyn, D.F., Proc. Inst. Radio Engrs., 47, 147, 1959.